UNIVERSITY OF CALIFORNIA, MERCED

Exploring the Dynamics of Confined Microtubule-Based Active Matter

A dissertation submitted in partial satisfaction
of the requirements
for the degree of Doctor of Philosophy
in Physics

by

Fereshteh L. Memarian

Committee in charge:
Professor Kevin Mitchell, Chair
Professor Linda S. Hirst, Advisor
Professor Bin Liu
Professor Rob Phillips

The dissertation of Fereshteh L. Memarian is approved and is acceptable in quality and form for publication on microfilm and electronically.

Rob Phillips

Bin Liu

Linda S. Hirst, Advisor

Kevin Mitchell, Chair

University of California, Merced
2023

Dedications

This thesis is dedicated to all the brave students around the world, especially in Iran, who have been imprisoned because they spoke up about the political situation or couldn't pursue their education due to financial problems. Your unwavering courage and determination to stand up for what you believe in, despite the risks and consequences, are a testament to the power of education and the human spirit. Your struggles remind us that access to education is not always a given and that we must continue to fight for the right to learn and grow. Your resilience in the face of adversity is an inspiration to us all. May your sacrifices serve as a reminder of the importance of education as a tool for progress and empowerment. May your spirits be lifted by the knowledge that you are not alone, and may your bravery inspire us all to work toward a more just and equitable world where education is accessible to all.

Table of Contents

Acknowledgments

I am deeply grateful to the many individuals who helped me shape and refine this work with their comments and support. My husband Michael provided unwavering support and encouragement in the most challenging moments that helped me persevere. I feel incredibly lucky to have had him on this journey. I can't wait to get old with you.

I am also deeply grateful for the mentorship and support of Professor Linda Hirst, who welcomed me into her lab and provided guidance and support throughout this project. I can only imagine having completed this work without her expertise and mentorship. I am forever grateful for the opportunity to work in the Hirst lab under her leadership. Thank you for your patience and encouragement.

I want to thank my committee chair and collaborator, Prof. Kevin Mitchell, for all he has taught me and his patience throughout the process. I would also like to thank my committee members, Dr. Bin Liu and Prof. Rob Philips. Dr. Liu generously offered me his lab equipment and provided valuable insights and guidance, while Prof. Rob Philips helped me become a better person in both my work and life. Thank you for all the unforgettable memories and lessons.

I am also deeply grateful for my family and friends' unconditional love and support. While I regret not spending more time with them, their support has meant everything to me. In particular, I want to acknowledge my mother, whom I deeply miss as I write this, and my sister.

Additionally, thank Dr. Heun Jin Lee at Caltech for all the training and for answering all my questions. Prof. Ajay Gopinathan, Dr. Daniel Beller, and Dr. Kinjal Dasbiswas for their great collaboration and contributions.

Finally, I would like to thank my lab mates, especially Dr. Amanda Tan, Dr. Joseph Lopes, Jocelyn Ochoa, and Derek Hammar, for their support and for making me feel at home. Your training and camaraderie have been invaluable to me throughout this project.

I would also like to acknowledge the various sources of funding for this work, including a confocal microscope acquired through the National Science Foundation MRI Award Number DMR-1625733 and generous funding from the National Science Foundation grants DMR-1808926, NSF-CREST: Center for Cellular and Biomolecular Machines at UC Merced (HRD-1547848), and the Brandeis Biomaterials Facility (DMR-2011846).

Curriculum Vitae

Fereshteh L. Memarian

fmemarian@ucmerced.edu | https://www.linkedin.com/in/fereshteh-memarian/

Education

University of California, Merced – *Merced, CA, USA*
Anticipated Spring 2023 | Ph.D. Candidate in Physics

University Akron – *Akron, OH, USA*
M.Sc. Physics Aug. 2016 – Aug. 2018

Azad University, Science and Research Tehran – *Tehran, Iran*
B.Sc. Physics Sept. 2011 – Feb. 2016

Professional Experience

Internship

• Bosch - Sunnyvale, CA

Spring 2023 Microfluidics engineer intern working on prototyping parts for the next-generation point-of-care diagnostics systems and quantitative data analysis.

Graduate Researcher

• University of California, Merced

2021 Built a cost-effective high-performance Total Internal Reflection Fluorescence (TIRF) microscope and optical trap at the California Institute of Technology (Caltech)
2020-2022 Carried out experiments to confine microtubule-based active matter in microfluidic wells and control the dynamics of the system
2019-2022 Fabricating microfluidic devices with photolithography and ultra-resolution 3D printing
2019 Performed image analysis using the Maximum Likelihood Estimation (MLE) method in Python, for publication in chapter 12 of ”Physical Models of Living Systems”
2018-2022 RF Plasma cleaning, surface treatment, and polymer coating of microfluidic devices
2018-2022 Tubulin purification from porcine brain tissue and subsequent polymerization to microtubules
2018-2022 Protein expression and purification of kinesin motor proteins from E.coli

• University of Akron

2016-2018 Theoretical studies on electron scattering effects for materials with Graphene-like band structures with MATLAB

Technical Skills

• Microscopy and spectroscopy (Confocal, Fluorescent, TIRF, AFM, SEM, TEM, EDX)
• Microfluidics (Lithography, Nanoscribe, Ion-Beam Evaporation, DIRE, 3D printing, Injection molding)
• Quantitative image analysis (FRAP, Particle image velocimetry, Particle tracking, Ilastik)
• Data analysis and interpretation (MATLAB, Python)
• Software (AutoDesk Fusion 360, Solidworks, Micromanager, ImageJ)
• Protein characterization (Gel electrophoresis, Bradford assay, Chromatography)

Publications

• **Memarian F. L.**, Hirst L. S., *Effect of internal energy depletion on active nematic texture and dynamics*, Submitted (2023).
• **Memarian F. L**., Khaladj, D., Hammar, D., Hirst L. S., Forming, confining and observing microtubule-based active matter, Vis. Exp., e64287, In-press (2022).
• **Memarian, F. L.**, Lopes, J. D., Schwarzendahl, F. J., Athani, M. G., Sarpangala, N., Gopinathan, A., Beller, D. A., Dasbiswas, K., Hirst, L. S., Active nematic order and dynamic lane formation of microtubules driven by membrane-bound diffusing motors, Proceedings of the National Academy of Sciences, 118, 52 (2021)
• Effect of Electron scattering on linear conductivity for Graphene-like band structure Master's thesis, University of Akron, Physics (2018)

Presentations

- Oral Presentation: *Microtubules' Dynamic Apolar Lane Formation and Long-Range Order on a Supported Lipid Bilayer*, American Physical Society, 2022
- Oral Presentation: *Microtubules' local and global order on membrane-bound motor proteins*, Biophysical annual meeting, 2022
- Oral Presentation: *Global order and lane formation in Microtubule-based active matter*, American Physical Society, 2021
- Oral Presentation: *Microtubule Motility on Fixed and Diffusive Motor Proteins*, American Physical Society, 2020

- Poster Presentation: *Crowd surfing at the molecular level*, CCBM Workshop on Emerging Themes in Cellular and Biomolecular Machines, 2019
- Oral Presentation: *Correlation of microtubule buckling and motor protein concentration*, UC Systemwide bioengineering symposium, 2019
- Poster Presentation: *Microtubule Buckling driven by motor activity*, UMass Summer School on Soft Solids and Complex Fluids, 2019
- Poster Presentation: *Effect of Electron Scattering on linear conductivity for Graphene,* American Physical Society, 2019
- Poster Presentation: *The importance of classical Elastica theory in buckling of microtubules*, Biomaterial Symposium, 2019
- The Standard Model at 50 Years, Case Western Reserve University, OH, 2018
- 2nd Institute of advanced studies school on Particle Physics and Cosmology and Implications Technology supported by CERN, Nanyang Technological University, Singapore, 2015
- International Workshop, GALAXIES INSIDE AND OUT, IPM Tehran, Iran, 2015
- IAU MENA Regional Summer School 2014: Astronomy with Small Telescopes, Notre Dame University-Louaize, Lebanon, 2014
- 3rd International Conference of Eclipsing and Occultation, IOTA/ME Tehran, Iran, 2012
- Organization Committee of Exoplanet Workshop, Plasma Physics Research Center Tehran, Iran, 2012

Fellowships/Awards

• CCBM Fellow: NSF-funded center for cellular and bio-molecular machines – Jun. 2022
• CCBM Training Award ($2,800): Ultra-precise Nanofabrication and Deep Reactive Ion Etching(DRIE) at California Institute of Technology (Caltech) – Dec. 2021
• GRAD-EXCEL Peer Mentorship fellowship – Sept. 2021
• Research Award ($10,000): Building a total internal reflection fluorescence (TIRF) microscope at California Institute of Technology (Caltech) – Feb. 2021
• National Science Foundation funded National Research Training: Innovations in Graduate Education program in Interdisciplinary Computational Graduate Education (NRT-ICGE) – Jan. 2020
• Research Award ($10000): Investigating effects of environmental viscosity on chaotic advection in a biological active nematic – Jun. 2019
• CCBM Scholar – CREST: Center for cellular and bio-molecular machines, UC Merced 2018-2023
• The First Radio Telescope Competitions of Iran-2nd place – Mar. 2015
• Excellence Grant, 2nd Institute of Advanced Studies School on Particle Physics and Cosmology, And Implications for Technology supported by CERN – Feb. 2015
• Excellence Grant, IAU MENA Regional Summer School – Aug. 2014

• The First Design and Manufacturing Physical Instruments Challenges Award of Iran 2nd place – Apr. 2012
• The Second Sundial Competition of Iran – 2nd place – Sept. 2010

Associations

- Secretary of Biophysics Graduate Club: Organization of a journal club to discuss new research papers with other graduate students and invite speakers for personal development webinars.
- President of the Iranian Association: Promoted diversity at UC Merced through the organization of an Iranian New Year event involving cultural presentations, live music, and dance performances, and catered food for over a hundred guests.

Lists of Symbols, Tables, Figures, and Illustrations

Abstract

Active matter is ubiquitous in nature, from the flocking of birds to the swarming of bacteria. Both living and non-living systems are out of equilibrium and exhibit rich dynamics that are of fundamental interest. This thesis focuses on the microtubule based active matter, a fascinating material class that has attracted significant attention in recent years. The first project, investigates the dynamics of microtubules propelled by diffusive motor proteins on lipid bilayers, providing insights into bidirectional lanes and nematic phase behavior. The second, third, and fourth projects explore dense microtubule-kinesin systems bundled together with motor protein clusters. In 2D, these systems exhibit self-organizing patterns and nematic-like behavior. In chapter four, I discussed different parameters can change the morphology of active nematics, such as oil viscosity and the fuel source or ATP. In chapter five, I discussed a robust experimental method to confine the active nematic laterally in different geometries. In chapter six, the material is confined in cardioid-shape geometry, and an efficient mixing pattern or golden braid pattern and more controlled dynamics have been shown. Overall, this dissertation advances our understanding of microtubule-based active matter systems, providing a framework for controlling and manipulating these materials for practical applications in the future for drug delivery systems and soft robotics.

Chapter 1

Introduction

Active Matter

Active matter is a term used to denote a collection of active bodies in which every active unit consumes energy to move or exert force as a part of a large group. This field of study is growing multidisciplinary research that gathers researchers from biophysics, soft matter, and fluid dynamics[1]–[4] Reminiscent of my research today, Leibniz wrote in 1704, ”Define the organism or natural machine, as a machine each of whose part is a machine.”[2], [5] Active matter can be found everywhere on different scales. Some diverse biological and synthetic examples of active matter include sheep herding, flocking birds on the largescale, and colonies of bacteria, and synthetic active colloids on smaller scales can be found in Figure 1.1[1], [2]Components of active matter are self-driven, i.e., they consume energy without external input of energy into the system, which then drives the system out of equilibrium.[1], [2], [4] It is fascinating that similar behaviors in different active matter systems can be seen, for instance, collective motion from larger scales like fishes to small scales like bacteria or synthetic colloids.
Active matter structures consume energy individually, move collectively, and react to the environment collectively. If there is a predator near a school of fish, they react and change their collective structure accordingly.[2], [6]

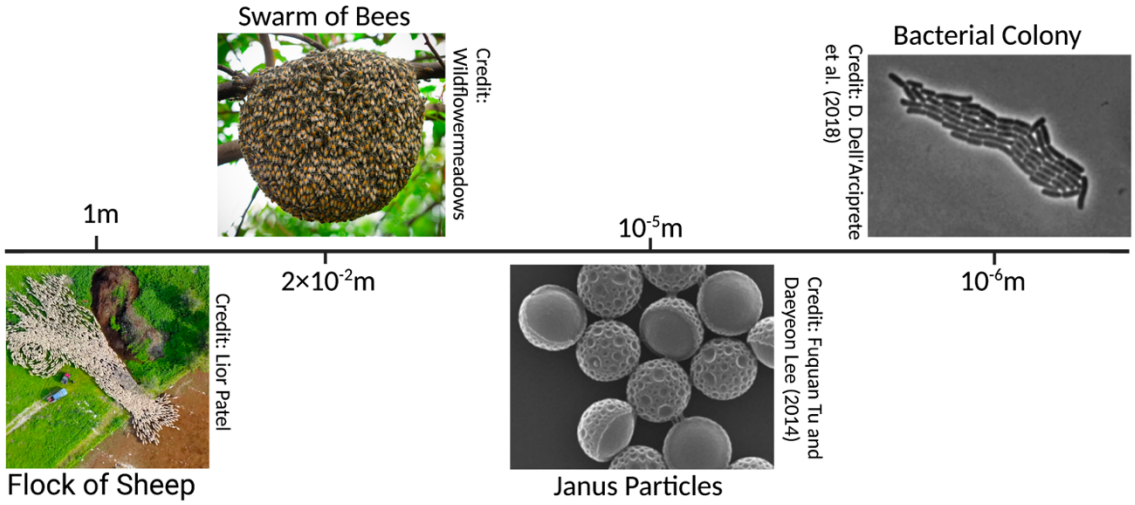

Figure 1.1: Active matter in different forms and scales. A Flock of sheep, a swarm of bees, and a bacterial colony are examples of living active matter. The synthetic active matter example is Janus particles.

Active matter individual units or active agents constantly consume and dissipate energy and, as a result, exhibit emergent behavior out of equilibrium.[7] For far from equilibrium systems, classical statistical mechanics cannot be used to study these systems. Nature inspires us with all the living active matter systems and helps us understand active matter's non-equilibrium state.[2], [6], [8] By controlling an active structure, we can manipulate its dynamics, use them in material transport, and convert its activity into mechanical work. Understanding a simplified system *in vitro* is a step towards understanding more complex systems, especially in living systems with complicated structures.

Over the last two decades, active matter systems with biopolymers have become an interesting topic. Three major processes are common in active matter systems made of biopolymers: self-assembly, self-organization, and collective motion.[1]–[3], [5], [8]–[12]

Collective Motion in Active Matter

Active matter exhibits a self-driven dynamics and rich variety of emergent phenomena out of equilibrium, one of which is collective motion. Collective motion in active matter refers to the coordinated movement of many self-propelled entities, such as cells, animals, or robots. In these systems, the motion of individual entities is influenced by their interactions with their neighbors, leading to emergent behaviors such as flocking, swarming, and pattern formation.[1], [3], [13], [14] From large-scale active matter systems like herds of reindeer to small-scale systems,

like a bacterial colony, collective motion can lead to long-range order and patterns on large scales compared to the size of the active units. For instance, ants with an average length of 5 millimeters can make ant trails 100 times or longer than their length.

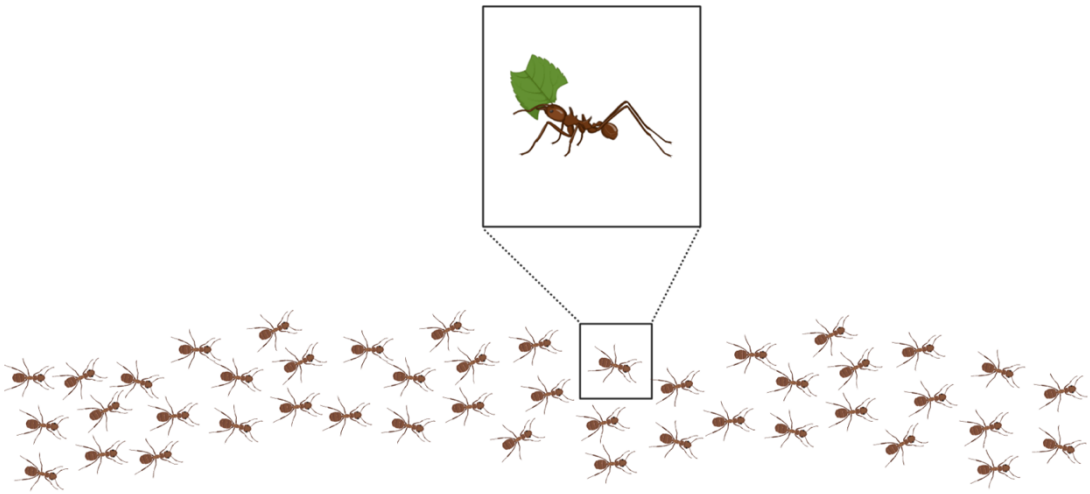

Figure 1.2: Length of an ant trail versus the average length of an ant which is 5 millimeters.

The Vicsek model for active matter was developed by Tamás Vicsek and his research group at Eötvös University in Budapest, Hungary, in 1995. The Vicsek model is a mathematical model that describes the collective motion of self-propelled particles for the collective motion of animals, known as the animal flocking Viscek model. The Viscek model is for discrete active particles John Toner and Yuhai Tu in 1995 proposed a model for a continuum version of the Viscek model.[13], [15] In the continuum model, hydrodynamic interactions are important, and by changing the friction, we can tune the system's dynamics. [3]
Another phenomenon is Motility-induced phase separation, or MIPS which arises due to the interplay between self-propulsion, particle interactions, and their surrounding environment. In MIPS, the collective motion of active particles can lead to distinct phases where active units with similar motility and direction of motion get closer together, and particles with different motility segregate from each other. The self-propulsion of the particles generates local density fluctuations, which in turn can induce attractive or repulsive interactions between the particles.[16] Collective motion and MIPS has also been seen in synthetic active matter systems. Janus particles are notable examples of synthetic colloids. They behave collectively and are self-propelled. Yi et al.[17] Studied Janus particles, half-coated with gold and half-coated with platinum. These Janus particles are dispersed in hydrogen peroxide solution, and their activity combines self-electrophoresis and diffusiophoresis; at high concentrations, they show clustering.

Molecularly imprinted polymer-based Janus particles are becoming increasingly fascinating for biological applications, particularly biosensors. They offer flexibility in design to cater to different biosensing applications, including antibody detection. The ability to design Janus nanoparticles based on gold or platinum makes them even more appealing from an electrochemistry perspective.[18]–[20]
Common non-equilibrium phenomena in biological systems can also be replicable in synthetic active matter, and theories apply to both systems. By knowing this, if we learn how to control and tune the collective motion, we can apply it to other active matter systems, and for every new system, when you can tame the chaos, there are applications.

In vitro studies on active matter

In vitro studies on active matter refer to experiments that investigate the behavior of self-propelled particles in a controlled laboratory environment. This category of active matter agents is made of biological or synthetic materials such as biopolymers or Janus particles.
Janus active matter refers to active matter systems consisting of asymmetric particles with different properties. These particles can exhibit unique behavior and dynamics compared to conventional active matter systems due to the added complexity introduced by the asymmetry. [21], [22]
Biopolymer-based active matter refers to systems made up of biopolymers, such as proteins, DNA, or other biological polymers. These systems exhibit complex behaviors and dynamics due to the interplay between the biopolymers' biological properties and the active particles' physical properties. For example, DNA curtains are nanoscale assemblies consisting of long, thin DNA molecules suspended in a solution and controlled by the electric field, DNA concentration, or other molecules. DNA curtains are often used as a model system to study the behavior of DNA and other biological polymers and to explore the potential applications of DNA-based materials. [23], [24]
In this thesis, the focus is on the biopolymer-based active matter. This field of study aims to understand the collective behavior of active particles and their interactions with each other and their environment.

Biopolymer-based Active Matter

Biopolymers are part of the cytoskeleton and exist in eukaryotic cells. Eukaryotic cells have three major filaments: actin filaments, intermediate filaments, and microtubules. These three filaments provide the structural framework and support for eukaryotic cells, helping to maintain their shape, organization, and function. Actin filaments made up of actin monomers are mostly near the cell's plasma

membrane, giving shape to the cell membrane and supporting the cell membrane. Actin filaments are the thinnest of these three filaments. The second category of filaments is Intermediate filaments. Intermediate filaments are thicker than F-actin and thinner than microtubules. They are ropelike and made up of fibrous protein. Intermediate filaments provide support for cell membranes in extracellular interactions. Microtubules are the largest and strongest filaments, giving the cell membrane shape, and are crucial for cell division.[6], [25] Cytoskeletal filaments and motor proteins can be combined, making a novel synthetic active matter system.[2], [6] Motor proteins can propel the filaments, and these systems can be used to study collective motion.

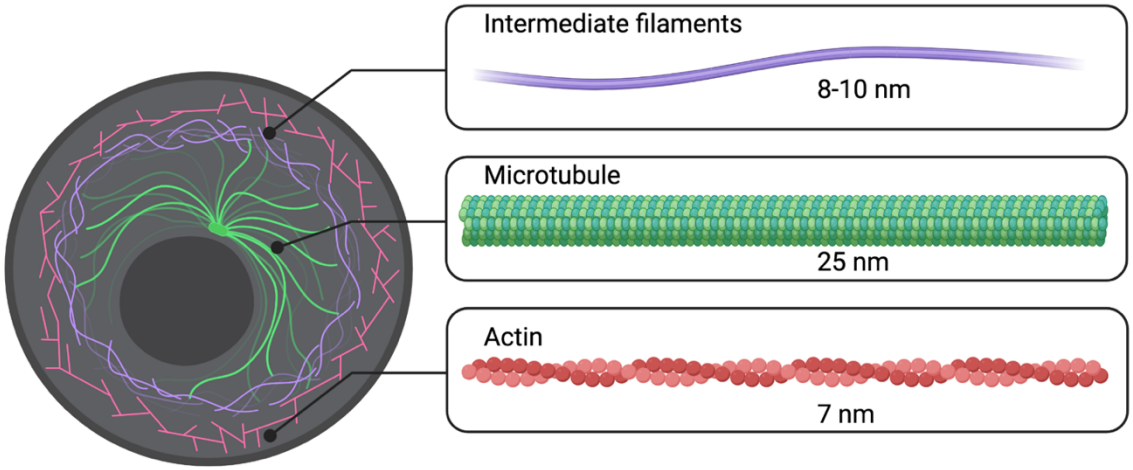

Figure 1.3: Schematics of filaments in the Eukaryotic cell. Actin filaments are the smallest filaments in the cell, and their thickness is approximately 7nm, the second thinnest filament is the intermediate filament which his 8-10 nm, and microtubules are the biggest filaments with 25nm thickness in the cell. The figure is made on BioRender.

Future application

In vitro studies on living or not living types of active matter can shed light on fundamental principles underlying the behavior and dynamics of active matter and have potential applications in fields such as biotechnology, soft matter physics, and material science. To go deeper into potential applications, one of the newest biotechnology research fields is Cell-ag or cell agriculture. Cell-ag involves manipulating and cultivating cells in an artificial environment, such as a cell culture dish or a bioreactor. Cell-ag aims to understand the behavior of cells and their interactions with each other and their environment and to develop new methods for growing and manipulating cells.[26] Saw et al. investigated cell sheets and their dynamics in 2D made of epithelial cells.[27], [28]

Another application of studies on active structures is in mixing because these individual units in an active network exhibit self-mixing and self-organizing behavior. Mixing is an essential aspect of fluid dynamics, which refers to combining two or more substances to produce a homogeneous mixture. In cell-ag, mixing ensures that cells are evenly distributed in the culture medium and that nutrients and other factors are evenly distributed throughout the culture. Proper mixing is crucial for maintaining the health and growth of cells in cell-ag systems.

In this thesis, two active systems are explored. Chapter 2 provides the necessary background information for Chapters 3-6. Chapter 3 focuses on the first active system, which is a microtubule-based active matter on a lipid bilayer. Chapter 4 discusses the dynamics and morphology of microtubule-based active nematic at the water-oil interface, focusing on the effect of oil viscosity and ATP. Chapter 5 explores the confinement of microtubule-based active nematic in different geometries using a robust experimental setup. Finally, Chapter 6 investigates the transition from chaotic to periodic motion in highly confined structures by examining the behavior of microtubule-based active nematic in cardioid-shaped geometries.

Chapter 2

Background

This chapter provides a necessary background for the subsequent chapters. It begins by introducing the components of microtubule-kinesin-based active matter and their active self-assembly, followed by a discussion of previously published works. The chapter then discusses liquid crystals and their nematic phase, which is the crucial background for the active nematic system. Next, it describes the topological defects and characteristics of the active nematic structure. The chapter discusses previous investigations into confinement's effect and the characteristic length scale of microtubule-based active nematic.

Biological building blocks of active matter

Microtubules

Microtubules are made of tubulin dimers; in the cell, they polymerize and depolymerize constantly.[6] Microtubules have a plus-end and a minus-end. They polymerize faster at the plus-end versus the minus-end[29]–[32] Polymerization of microtubules can be stabilized with Taxol to adjust the persistence length and keep it similar throughout experiments by preventing depolymerization.[6], [31]–[33] Different chemicals could promote tubulin polymerization. In my research, I am using two different chemicals for polymerization, guanosine triphosphate (GTP) and guanylyl 5′-α, β-methylene diphosphonate (GMPCPP). GTP promotes microtubule polymerization and makes them more flexible. However, GMPCPP makes microtubules three times stiffer. GMPCPP microtubules also depolymerize more slowly, i.e., they are more stable. (Figure 2.1a)[6], [31], [32], [34]

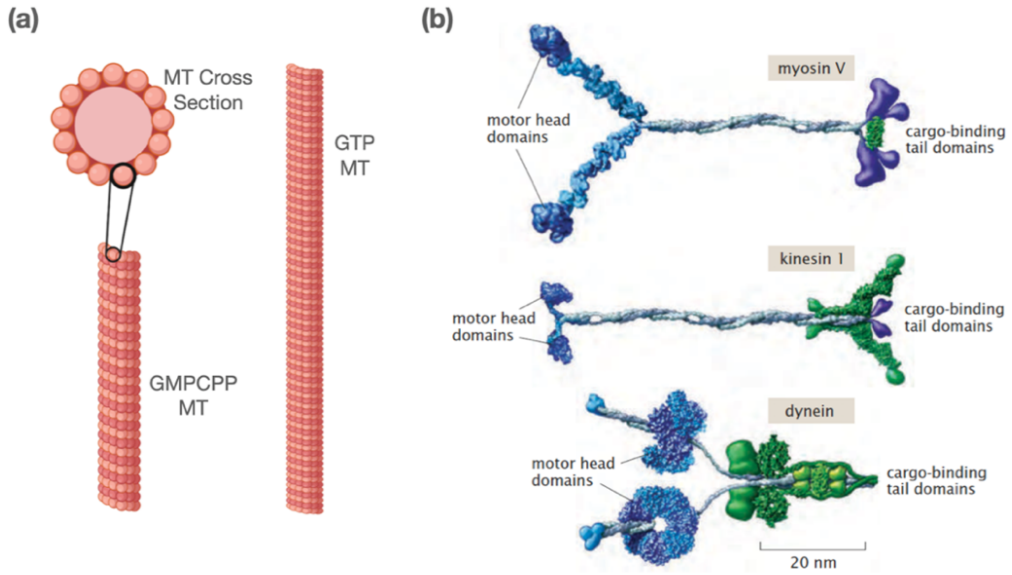

Figure 2.1:a) Schematics for two different microtubule filaments. GMPCPP microtubules are shorter and stiffer, and GTP microtubules are longer and more flexible. b) Three different types of motor proteins. From top: Myosin moves on actin filaments, Kinesin moves on microtubules from the minus end to the plus end, and Dynein moves on microtubules from the plus end toward the minus end. Image reproduced from The Molecular Motor Toolbox for Intracellular Transport, Vale, 2003 with permission.[35]

Motor Proteins

There are three main types of motor proteins: myosin, dynein, and kinesin (Figure 2.1b). Kinesins processes along the microtubule from the plus-end to the minus-end, converting chemical fuel (adenosine triphosphate (ATP)) into mechanical energy to walk.[6], [36], [37] The effect of local ATP concentration on a single motor protein's velocity has been studied by S. P. Gilbert et al.[38] shows that as we increase the ATP, the velocity increases until the system gets saturated with the fuel. It follows Michaelis-Menton kinetics[39], which demonstrates the relation between the reaction rate and the substrate concentration following the formula:

$$v = V_{max} \frac{[S]}{K_M + [S]}$$

Where *v* is the reaction rate, Vmax is the maximum reaction rate, S is the substrate concentration, and K_M is the Michaelis constant which shows the enzyme's affinity for the substrate. When the substrate concentration equals the Michaelis constant, the reaction rate has reached half its maximum value. When ATP binds to kinesin motor protein, the ATP hydrolyzes a phosphate group and turns into ADP. For this enzyme reaction, the substrate concentration is ATP.

Kinesins' step is 8nm, and they exert 5pN of force.[6], [36], [40] Conventional kinesin, or kinesin-1, is made of a motor domain connected to a coiled-coil stock and a tail domain. The tail domain binds to the cargo.[40] Some of the kinesin

motor proteins we use are tagged with Green Fluorescent Protein (GFP), and fluorescence microscopy is being utilized for quantitative studies.

Microtubule-based collective motion

Collective motion or swarm behavior of active matter is related to their self-assembly. Interactions between active agents can be attractive or repulsive depending on the distance and orientation between the active agents. These interactions can lead to the formation of clusters, bands, and vortices, which can have specific directionality without the input of external forces.[1]–[3] Microtubules propelled by kinesin are used to study the active self-assembly of structures and collective motion. In a microtubule gliding assay, motor proteins are anchored on a glass slide, and microtubules glide on top. By introducing ATP to the system, motor proteins propel microtubules forward, and microtubules start gliding on motors. Gliding microtubules can form a wide range of structures, from linear bundles to more complex systems like spools[12]under certain conditions. For instance, spools can be made with a biotin-streptavidin bond on microtubules, making them sticky and sticking to themselves.[12] In a biological cell, motor proteins for better efficiency in cargo transportation tend to move collectively. However, how they efficiently do this transportation still needs to be determined. Studies by S. R. Nelson et al·[41]on myosin Va with actin filaments on lipid bilayer demonstrate that transportation depends on lipid diffusion and the number of motor proteins. There are also theoretical studies by Sarpangala et al.[42] discussing the efficiency of transport by a group of motor proteins on a diffusive membrane and is highly efficient vs. a single motor.

In microtubule-based active matter, which is the focus of this thesis, I studied this cell-like structure *in vitro* by inverting the system. A lipid bilayer substrate on the glass lets motor proteins diffuse on the lipid bilayer, and they are not fixed and immobile.[43] The composition of the lipid bilayer was chosen by its fluidity at room temperature, which is the temperature at that I performed experiments, and the lipid should be similar to cell membranes at body temperature. The lipid bilayer is a mixture of DOPC (1,2-dioleoyl-sn-glycero-3-phosphocholine) and DGS-NTA (1,2-dioleoyl-sn-glycero-3-[(N-(5-amino-1-carboxypentyl) iminodiaceticacid) succinyl]). This mixture is in the fluid phase at room temperature (89.95 mol% DOPC, 10 mol% DGS-NTA, and 0.05 mol% Fluorescently labeled lipid), which is mostly DOPC and DGS-NTA, which enables kinesin motor proteins to anchor to lipid bilayer and still be diffusive. I also used a small amount of labeled lipid to check the uniformity of the lipid bilayer using fluorescence microscopy. Dr. Joseph Lopes measured the diffusion constant of this lipid mixture at room temperature, which was found to be $9.01 \pm 0.58\ \mu m^2/s$. [44], [45]

Liquid Crystals

Liquid crystals (LCs) are a state of matter with properties of both liquids and solids and exhibit phases between liquid and solid. They have fluid-like mobility of particles but with orientational or positional order. They are ordered but not in a fixed lattice, i.e., molecules can flow past one another as in a liquid. This unique combination allows liquid crystals to change their physical properties in response to external stimuli such as temperature, electric field, or pressure. Some of the ways in which liquid crystals change physical properties are the alignment of liquid crystals and phase transition, viscosity, and birefringence.[1] Liquid crystals exist in both natural and synthetic materials. Synthetic liquid crystals are designed and manufactured for specific applications, and one common example is liquid crystal displays (LCDs), which are widely used in electronic devices such as televisions, computer monitors, and smartphones.
In contrast, natural liquid crystals can be found in biological systems such as the lipid membranes of living cells. Lipid molecules in the cell membrane are arranged in a liquid crystalline phase, which is crucial for the function of the cell.[1], [44] In the following, I discuss the lipid membranes in more detail.

Lipid membranes

The cell membrane is made of a lipid membrane, a thin barrier enclosing living organisms' cells. It consists of a lipid bilayer comprising two layers of phospholipid molecules arranged with their hydrophobic tails facing inward and their hydrophilic heads facing outward. This arrangement results in a barrier impermeable to many ions and polar molecules. [1], [44], [45]
The lipid packing fraction refers to the space occupied by lipids in a lipid bilayer. It is defined as the ratio of the volume occupied by the lipid molecules to the total volume of the bilayer.[1], [44]The packing fraction of a lipid bilayer is a critical factor that affects its physical properties, such as fluidity, permeability, and stability. Various factors can influence the packing fraction, including the lipid molecules' size, shape, and composition, temperature, and the presence of other molecules in the bilayer. A higher packing fraction generally leads to a more ordered and stable lipid bilayer, while a lower packing fraction may result in a more fluid and dynamic bilayer.[1], [44]

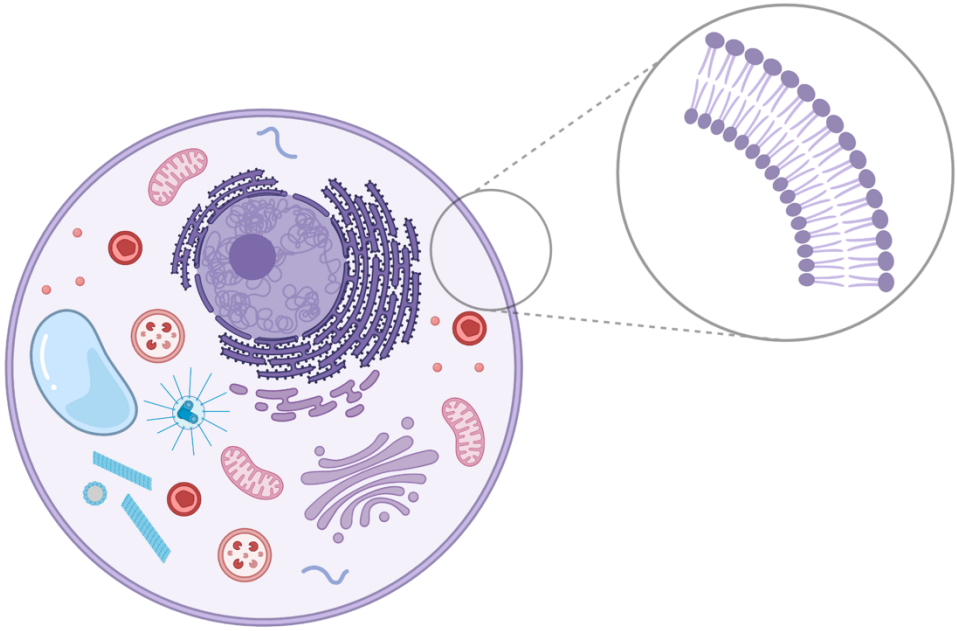

Figure 2.2: Schematics of a lipid cell membrane enclosing other cell organisms within the cell. The figure is made on BioRender.

A lipid bilayer has two main states in terms of its physical properties. The two states are the lipid gel phase and the lipid fluid phase. (See figure 2.3)[1], [44]

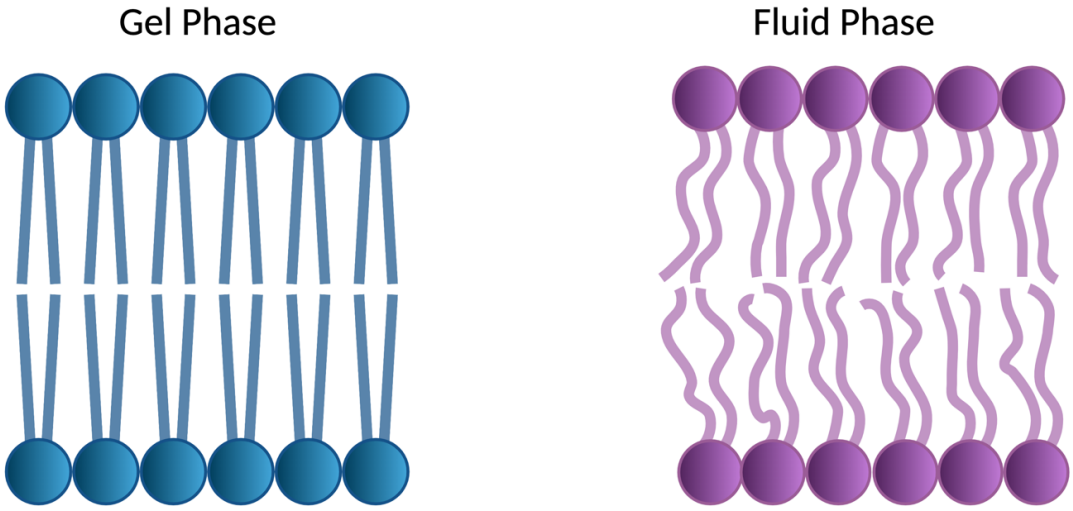

Figure 2.3: Two main states of lipid bilayers. Left the ordered or gel phase, and on the right, the fluid phase or liquid-disordered phase.

The lipid gel phase, also known as the solid phase, occurs when the lipid bilayer is ordered, and lipids are packed closely together, resulting in a more rigid and less fluid structure. This phase is characterized by a high degree of intermolecular

interactions and hydrogen bonding between the lipid molecules, which give the bilayer a high degree of stability.[1], [44]–[47]
On the other hand, in the fluid phase, the lipid bilayer is disordered. This phase is characterized by a lower degree of intermolecular interactions and hydrogen bonding in the polar head or the hydrophilic head of the lipid, leading to a more fluid and dynamic structure. The lipid fluid phase is always found at higher temperatures than the gel phase. The stability of a lipid bilayer can be disrupted by varying thermodynamic variables such as high pH or high temperatures.[1], [44]–[48]

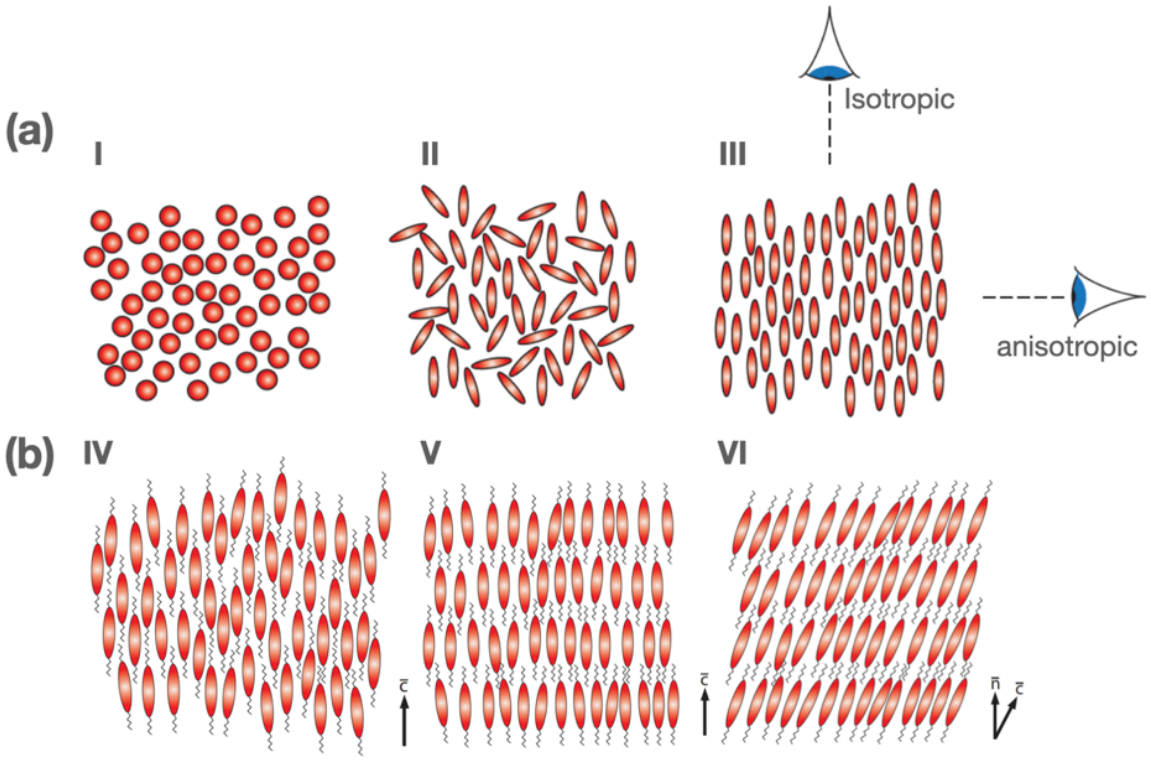

Figure 2.4: Liquid phases. a) Isotropy with different molecule shapes in bulk shown in panel [I, II]. In panel [III] when is viewed from top it is optically isotropic and from the side, it is anisotropic. b) Different phases of liquid crystals: Nematic [IV], smectic [V] and smectic C [VI]. Image is reproduced from Fundamentals of Soft Matter Science with permission.[1]

Nematic phase

LCs can exhibit different phases based on their orientational and positional order. (Figure 2.4) The nematic phase is a common liquid crystal phase in which the liquid crystal molecules exhibit orientational ordering but not positional ordering. The transition from disordered to nematic order is a first-order phase transition. In the first-order transition, the system needs latent heat to show the phase transition from isotropic to nematic; however, the change happens gradually and in a range

of temperature in the second-order phase transition. Orientational order in liquid crystals arises from the structural anisotropy of the molecules, which gives rise to their tendency to align in a preferred direction. This ordering is further driven by entropic effects, as the alignment reduces the system's entropy. The formation of topological defects is a consequence of this ordering, where regions of the liquid crystal have a different orientation from the bulk. These defects can have important physical properties and applications, such as in forming optical textures or in designing electronic devices. Liquid crystals also exhibit extraordinary sensitivity to interfacial events, which arises from the strong influence of surface properties on the orientation of the liquid crystal molecules. This sensitivity makes liquid crystals useful as probes of surface properties or as a means of controlling the orientation of molecules at interfaces.[1] The order parameter describes the degree of orientational order. The order parameter is between 0 and 1, with 0 indicating a disordered state and 1 indicating a highly ordered state. In liquid crystals, there are points, lines, or regions where the orientation is ill-defined, and liquid crystal molecules deviate from the surrounding of that region. Topological defects have a topological charge depending on the surrounding molecules and their orientation. The topological charge of a defect is often quantified by a winding number, which represents the number of times a closed curve around the defect rotates counterclockwise. This winding number is related to the topology of the director field and is a topological invariant that is robust against small perturbations. The topological charge is calculated as

$$q_{enclosed} = \frac{1}{2\pi}\int d\varphi$$

Where $q_{enclosed}$ is the total topological charge, φ is the orientation of the liquid crystal molecules at a point in space, and the integral is taken over a closed contour around the point defect. The resulting value of q determines the degree of twist or bend in the orientation of the liquid crystal molecules around the point defect. Thus, for 2π topological charge is +1, and with clockwise rotation, it will be -1 (Figure 2.5).[1], [4], [11], [49]

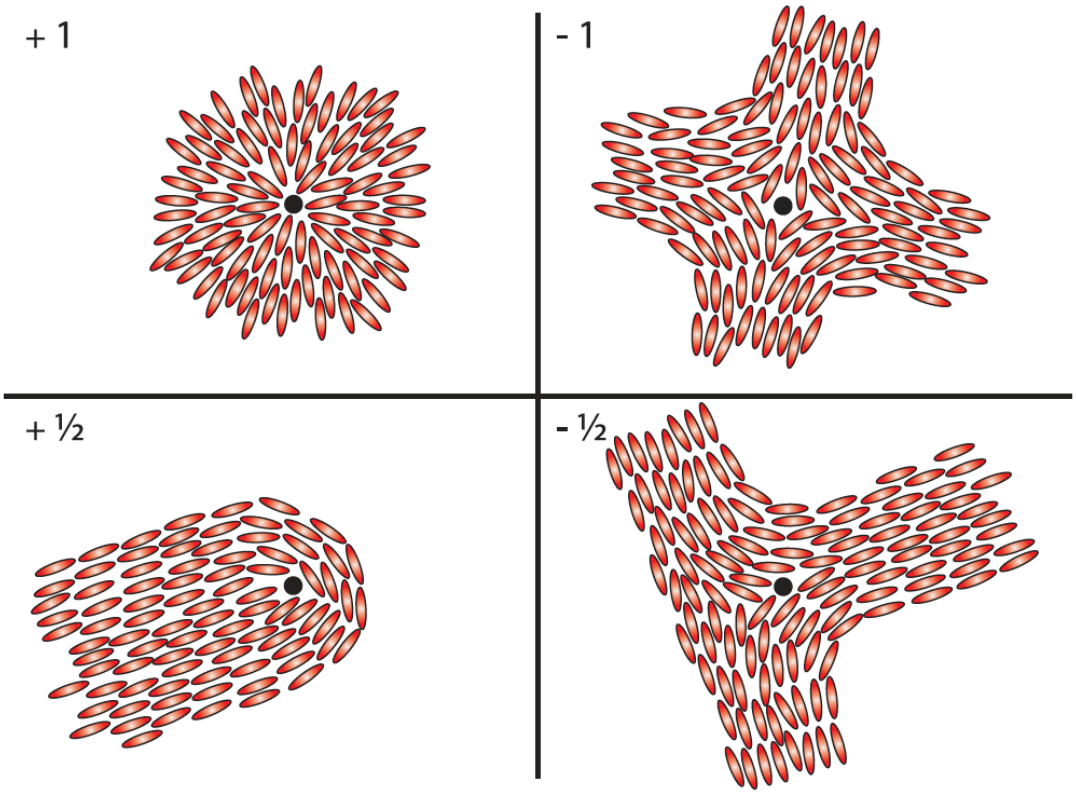

Figure 2.5: Topological defects in a liquid crystal phase and their topological charge. In the nematic phase, semi-integer defects commonly appear, with a topological charge of ±1/2 and in comet shape or trefoil shape. Image is obtained from Fundamentals of Soft Matter Science with permission.[1]

Active Liquid Crystals

Active nematic belongs to a class of liquid crystals made of active components but orientationally ordered with long-range order and topological defects. The can be made of cell and tissues[27] or bacterial colony[9], [50] or biopolymers[5], [10], [11]. Biopolymer-based active nematic systems are mostly made from actin filaments or microtubules assembled at a water-oil interface. Active nematic systems with actin filaments are contractile systems[37], and microtubule-based active nematic is extensile. They exhibit chaotic motion with the creation and annihilation of defects and the emergence of spontaneous flow.[1], [10], [51]
Microtubule-based active nematic is a new type of material that behaves like liquid crystals but is active, and it has potential new applications as a new type of material in soft robotics or drug delivery. Pattern formation in a microtubule-based active

network was first reported by F.J. Nédélec et al.[5], then by Sanchez et al.[10] became fully confined in a 2D plane and formed a nematic structure. In an active nematic, the microtubules are connected to each other with motor proteins. Kinesin 401(K401) with motor domains at both sides acts as an active cross-linker between microtubules and induces sliding force between filaments. K401 comprises two kinesins connected by Streptavidin and biotin (Figure 2.6). In a system with short and stiff microtubules, they behave similarly to rigid rods or liquid crystal molecules and transition to the nematic liquid crystalline phase, so we can use the physics of liquid crystals to study this system.[2], [10], [33], [52] On the microscopic scale, every microtubule combines, breaks, or buckles constantly, but on the macroscopic scale, the active bundles exhibit long-range order. Localized distortions in the director field of active nematic are topological defects. Topological defects in 2D active nematic are semi-integer, and in a bulk active structure, they are constantly annihilating and creating by moving in a 2D plane.

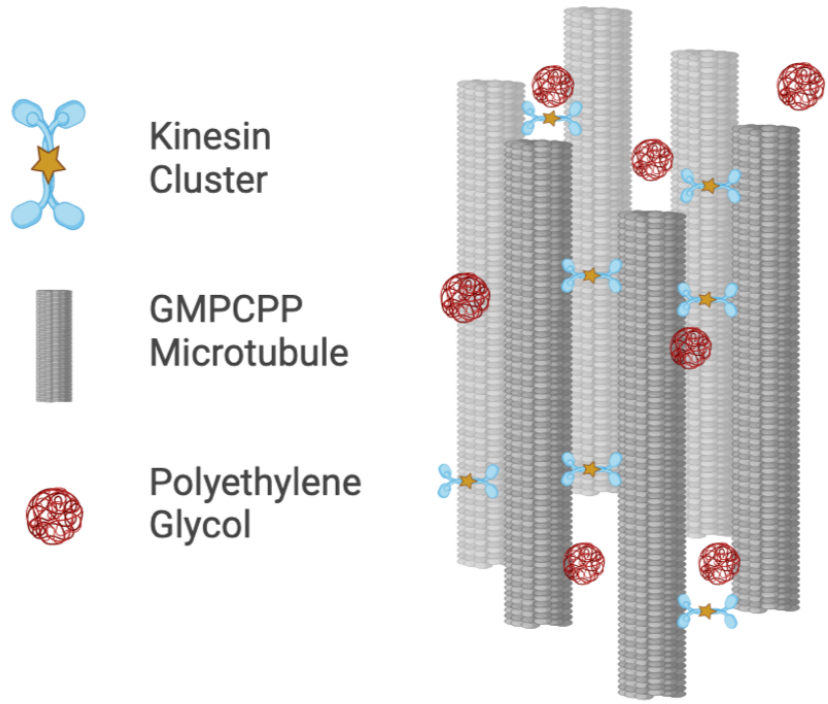

Figure 2.6: Schematic view of microtubule-based active bundles. Microtubules linked with kinesin clusters. Kinesin clusters are made of kinesin motor proteins and streptavidin-biotin. Bundles are formed and enhanced by the depletion force exerted by PEG depletants.

The orientation of liquid crystal molecules depends on their anchoring at the boundary. There are two main types of anchoring, homeotropic and planar anchoring. (Figure 2.7) In homeotropic anchoring, liquid crystal molecules tend to orient perpendicular to the boundary, and in planar anchoring, they tend to orient parallel to the boundary. The anchoring can be modified with surface treatment, and the desired anchoring can be promoted.[53], [54]

Figure 2.7: Schematic view of planar and homeotropic anchoring. In planar anchoring, liquid crystals' molecules are parallel to the boundary, and in homeotropic, they are perpendicular to the substrate.

Depletion Forces

The cell environment is crowded with all the cell organisms and cytoplasm. *In vitro* experiments often use crowding agents (e.g., Polyethylene Glycol or PEG) to add depletion force into the system and mimic the cellular environment.[6], [43]Depletion attraction happens when the smaller particle is mixed with other particles in the system, leading to aggregation between larger particles.[1] In figure 2.8, depletion attraction is illustrated and shows smaller particles bombard larger colloids with their Brownian motion. When the separation of the larger particles is larger than the diameter of the smaller particles, the bombardment is not uniform anymore. As a result, the larger particles get closer to each other. The depletion force is the net force applied on larger particles by smaller particles.[1]

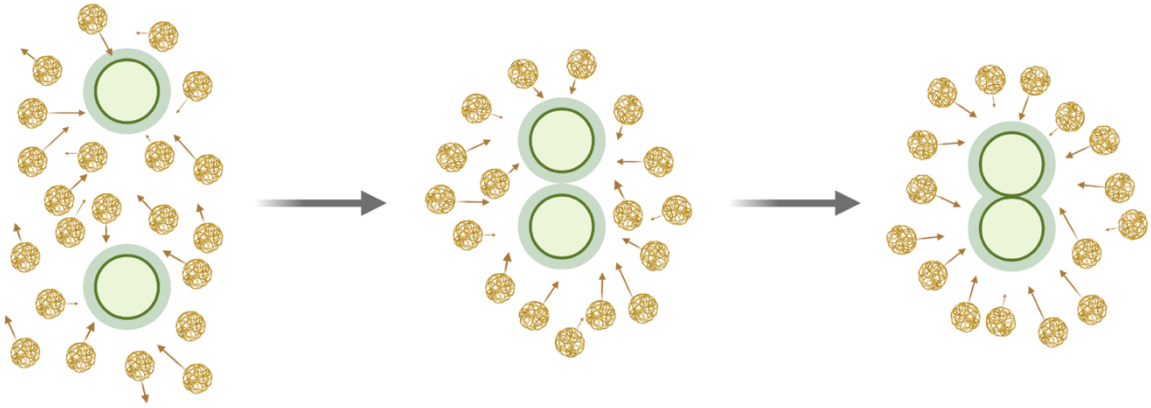

Figure 2.8: Schematic view of depletion force on colloidal particles.

The polymer used as a depletant in a solvent takes on a globular conformation due to entropic. An ideal polymer chain must take on a more compact conformation to minimize the excluded volume and maximize the entropy. This conformation can be quantified using various techniques, including static light scattering, small-angle X-ray scattering (SAXS), and size-exclusion chromatography. Quantification is based on the polymer's radius of gyration (Rg). [1] Polyethylene glycol is a

common depletant in biomaterials because it is non-toxic and safe. Based on its molecular weight, which measures the polymer chain size, the radius of gyration in a solution can be calculated. The radius of gyration is defined as the root mean square distance of the monomer units from the center of mass of the polymer chain.[1]A larger Rg value indicates a more extended and flexible polymer chain, while a smaller Rg value suggests a more compact and rigid chain. In microtubule gliding assay, (Figure 2.9), crowding agents exert force from different directions on microtubules.[43], [55] When the distance between filaments becomes smaller than the size of the crowding agent, filaments are forced to get closer and form bundles, also known as an excluded volume effect.[1], [6], [56]

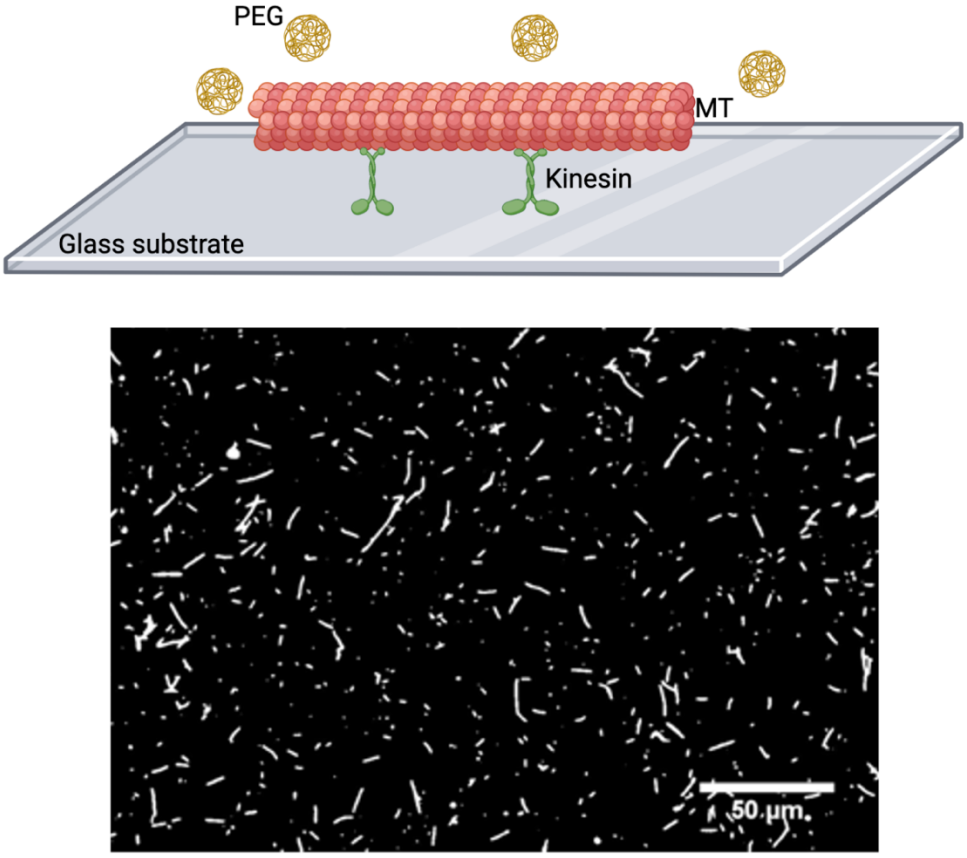

Figure 2.9: Top: Schematic view of microtubule gliding assay with depletants. Bottom: Fluorescent image of microtubules gliding on glass. Scale bar 50µm

Characteristics of microtubule-based active nematic

Active nematic structures are characterized by their unique behavior, which is distinct from traditional liquid crystals. Sanchez et al.[10] in 2012 confined this self-mixing structure in 2D and in the active nematic phase. The motion is described as active turbulent by different research groups and in 2019, Tan et al[11]. Used chaos theory to explore the chaotic behavior of this system. They focused on the self-mixing behavior for the first time and used topological defects as imaginary self-mixing rods in the fluid. The active motion of microtubules in an active nematic system generates stresses that can cause the system to become unstable, leading to chaotic and turbulent behavior. Active nematic structures also exhibit self-mixing behavior, where the particles' orientation can influence the system's flow.

Active turbulence or chaotic behavior can be quantified in different ways, for instance, topological entropy.[11], [57], [58] Topological entropy can be used to quantify the quality of mixing in our active nematic system. Adler, Konheim, and McAndrew first introduced as a metric in 1965.[59] In 2D active nematic, Tan et al.[11] discussed and measured topological entropy with different methods. The first method uses local stretching, and the second method is global mixing.[11], [57] Microtubule bundle extension within the network was measured using beads tracking and defect tracking in local stretching. Topological defects in the global mixing method are considered as stirring rods that create a braid like Taffy stretching or stretched and folded fluid lines in the paint.[11], [57], [60]
In 2D Microtubule-based active nematic topological defects constantly create and annihilate +1/2 (CCW π rotation) and -1/2 (CW π rotation) defects. (See figure 2.10) Previous studies have shown that -1/2 defects are less motile than +1/2 defects.[10], [11], [33], [61]

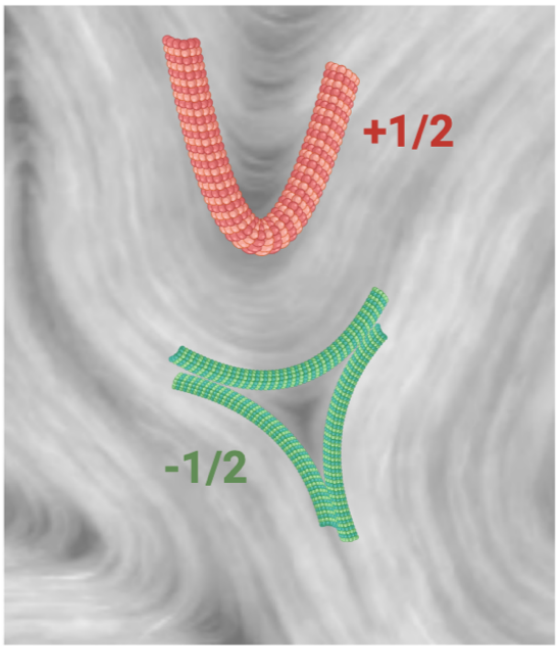

Figure 2.10: Microtubule-based active nematic with semi-integer topological defects. Comet shaped or +1/2 defect is red, and trefoil or -1/2 topological defects are shown with green.

Confined active nematic

Microtubule-based active nematic under confinement can exhibit different dynamics. Without activity, there is no flow; with activity in weak confinement, their dynamics are similar to the bulk, chaotic, or active turbulence described by Doostmohammadi et al.[62] in stronger confinements, when the confinement highly influences the network dynamics, the structure demonstrates a dancing motion[28], [63] or, in lower activities, potentially periodic motion.[64] Geometrical confinement is a strong tool to alter the dynamics of active nematics. Confinement can dampen spontaneous flow or enhance the motion in one direction.[61]
In 2014, F. C. Keber et al.[65] designed an experiment to constrain microtubule based active nematic in a vesicle. In that experiment, microtubules are active, the vesicle can be deformed, and topological defects are constrained to the surface of the vesicle. A combination of all of these produced different dynamical states. That study was one of the first to provide results for the importance of geometry on dynamics and vice versa. Figure 2.11 shows active nematic constrained on the vesicle and deformed vesicle by microtubules' dynamics.

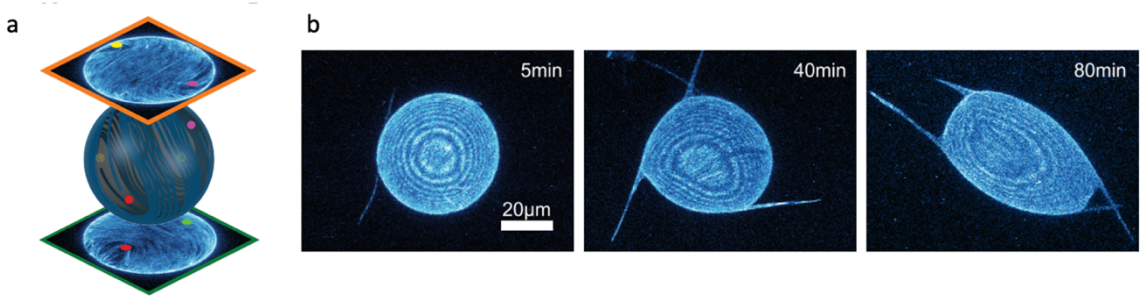

Figure 2.11: Microtubule constraint on the lipid vesicle. a) Topological defects on a lipid vesicle. b) Microtubules on a lipid bilayer deforming the lipid vesicle. Image is obtained from Topology and dynamics of active nematic vesicles [65] *with permission.*

Depending on the geometry variety of defect dynamics will be observed; for example, in a narrow channel, Shendruk et al.[63]simulated dancing disclination or topological defects swapping in a narrow channel. Another example is shown in figure 2.12, which is active nematic in a toroidal droplet by P. Ellis et al.[66], indicating that the net topological charge is negative in negative gaussian curvature regions. Near the positive gaussian curvature, the defect density is higher.[66] Also, the microtubule-based active matter was confined in a circular shape for the first time by A. Opathalage[54]and they categorized them based on the size of the confining wells into three categories of weak, medium, and strong confinement. Defect dynamics in different sizes of wells have been studied, and it shows that in strong confinement, they observed a +1 defect that wasn't stable.[54]

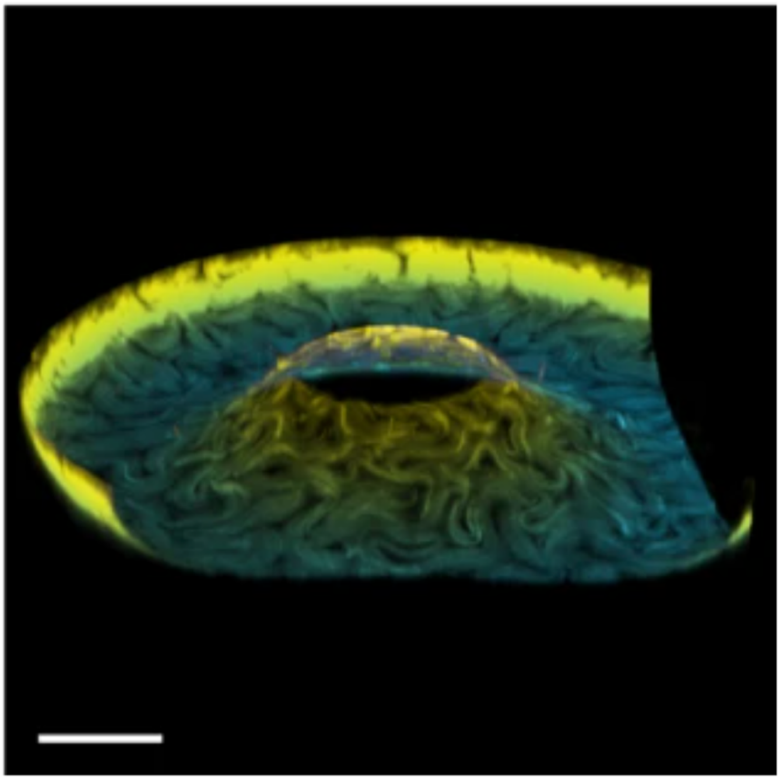

Figure 2.12: Microtubule-based active nematic confined in a toroidal droplet by P. Ellis et al. Image obtained from curvature-induced defect unbinding and dynamics in active nematic toroids [66] *with permission.*

Mixing and braiding

Fluid dynamics is an interesting field that applies to different flows, for instance, laminar flow, turbulent flow, and chaotic flow. Laminar flow is a smooth flow and does not represent fluid mixing. Turbulent flow exhibits a high level of mixing, and chaotic flow also shows high mixing, but usually, the mixing is exponential, and mixing with the surroundings is low. In a chaotic system, small perturbations to the initial conditions of the system can lead to vastly different outcomes in the long term. Exponential mixing describes the rate at which these perturbations spread out and become uncorrelated, destroying any initial patterns or structures in the system. Mathematically, exponential mixing is characterized by an exponential decay of the correlation function between two trajectories in the system. This decay occurs over a characteristic timescale known as the Lyapunov time, which is related to the rate at which the perturbations grow. Fluid mixing is complex and highly dependent on the mixing protocol; we can achieve different mixing qualities with other protocols such as laminar mixing versus turbulent mixing. Mixing in nonequilibrium systems refers to combining substances to create inhomogeneities or gradients. For example, ocean mixing occurs through several processes, including wind-driven surface, tidal, and mixing due to temperature and salinity

gradients. In the ocean, mixing plays a critical role in distributing nutrients and other substances that support marine life.
The system is out of equilibrium in microtubule-based active nematic, and microtubules are self-mixing. Jean-Luc Thieffault discussed a method to measure the quality of mixing or topological entropy by following the mixing rod exchange pattern. Rod exchange patterns are similar to braid, and each rod represents a strand in a braid. A complete motion of the mixing rod can be described as a braid. Chaos is a result of the topology of rod motion. Depending on the fluids and how critical good mixing is, different numbers of rods can be used. The mixing protocol and mixing pattern change the mixing result. The best mixing with three rods can be achieved by following the golden braid, the classic three-strand braid. Silver braids are another classic braid that rods showing counterclockwise or clockwise interchange. Braids are like dancing particles; with more rods, different braid groups can be created.[60], [67]
As previously reported by Tan et al.[11] mixing fluids by stirring rods can inspire exploring mixing in microtubule-based active nematic. The mixing of fluids can be studied with mathematical models that apply to active nematic fluids. In fluid mixing, the goal is to achieve efficient mixing and quantifying it. Topological entropy, which is a measure of mixing can be quantified in different ways, for instance, by measuring global mixing or local stretching. In microtubule-based active nematic, +1/2 defects can be assumed as invisible stirring rods. We can measure the microtubule-bundles stretching in the active nematic fluid and find the Lyapunov exponent in local stretching. The Lyapunov exponent measures the stretching between two neighboring points in fluid and can be measured by the velocity gradient.

Characteristic Lengthscale

The characteristic length scale is an essential parameter for describing the behavior of the active nematic phase. In this phase, there are typically two characteristic length scales of interest: the length scale associated with the internal parameters, such as the length of microtubules, and the length scale associated with the balance between elastic and active stress. The length scale associated with the internal parameter is often called coherence length. This is because it describes the size of the defect core, and it is in the same range as the length of the microtubules. In this project, the length of the microtubules is approximately 2 μm. The motor protein concentration and the depletion force exerted by depletants like polyethylene glycol (PEG) are other internal parameters that can change the coherence length scale. Increasing the concentration of motor proteins and crowding agents can make the active nematic fluid stiffer and more like gels.[2], [8] The coherence length scale is defined as follows:

$$L_s = \sqrt{\frac{K}{A}}$$

Where L_s is the nematic coherence length, K is the Frank elastic constant corresponding to the bend and splay deformation of microtubule bundles, and A is the material constant related to the aspect ratio of microtubules.[3], [51], [68]
The other length scale is the active length scale in the active nematic phase. The material's balance between elastic and active stresses defines the active length scale.[3], [49], [51] The active length scale can be controlled by different parameters that control the activity and change the elastic constant of the active network, such as silicone oil on top of active nematic and ATP in the network. The active length scale in the nematic phase can be written as follows:

$$L_a = \sqrt{\frac{K}{|a|}}$$

Where L_α is the active length scale and the material's activity parameter, the activity parameter sign in extensile or pusher systems is positive, and in contractile or puller systems is negative.[8], [11], [33], [51], [61], [69]
Active length scales and the effect of different parameters on them will be discussed in more detail in chapter 4.

Summary

In this chapter, the background of the following chapters has been discussed. I started with microtubule-based active matter and its components, such as microtubules and kinesin motor protein. Then I discussed the membrane-bound transport and their self-assembly. Next, I discussed other researchers' prior work on active self-assembly, specifically microtubule-based self-organization. This is the required background for chapter 3. Next, I discussed liquid crystals and the background related to active liquid crystals. Microtubules' self-assembly pattern in 2D can be nematic and resemble liquid crystals' molecules. Then I discussed dense microtubule bundles in the nematic phase: their characteristics, and different ways to alter their dynamics. One of the ways that have been discussed more in detail with background is geometrically confined active nematic structures. Active nematic structures in the past decade gained much interest from scientists showing self-mixing. This part is the background related to chapters 4,5, and 6.
The focus of this dissertation is continuing the work on microtubule-based self assembly structures. The focus is on confining the active material in 2D and subjecting it to lateral confinement in various geometries to control its motion. The primary objective is to leverage confinement to modify the dynamics and demonstrate efficient self-mixing patterns in a controlled manner.

Chapter 3

Nematic order and dynamic lane formation in membrane coupled microtubule swarms

Introduction

Several research groups have described microtubule gliding on immobile motor proteins.[12] [55], However, microtubule gliding on diffusive motor proteins remains understudied. Gliding on diffusive motors was inspired by nature. Cells membrane and organelles membrane in eukaryotic cells are made of lipid molecules. Membranes are mostly made of two layers of lipid or a bilayer. In a simplified *in vitro* experiment, by combining 2-3 types of lipids, motor proteins can be anchored to the lipid and have similar fluidity to a cell membrane at room temperature.

In eukaryotic cells, kinesins walk on microtubules carrying cargo. They carry cargo in a group, and their attachment is diffusive to the cargo.[70] [42]

In this experiment, microtubules glide on motor proteins, and motor proteins are attached to a diffusive lipid bilayer similar to a cargo. [70] In 2019, Tjioe et al.[71] discussed that a group of kinesins was needed to smooth cargo transportation over a long distance. In 2022, Niranjan Sarpangala and Ajay Gopinathan[42] published a theoretical study on the cargo fluidity relation and enhancement of load-sharing and processivity of a group of kinesins. Based on these studies, they concluded that a group of motor proteins is needed efficient transportation of diffusive cargo.

Previously published studies by Tanida et al. in 2020[56]discussed the gliding of microtubules on motor proteins with varied exclusion effects on microtubules. Varying the volume exclusion effect using a depletant, they achieved global orientation and observed microtubule clusters. Alfredo Sciortino and Andreas R. Bausch also investigated the actin-myosin system on a lipid bilayer and observed polar lanes and clusters in high filament-density active systems.[72]

In my work, I present the experimental setup for microtubule gliding on motor proteins and motor proteins diffusing on the lipid bilayer substrate. In a high-density microtubule system, microtubules get close to each other and form bundles and lanes on the macroscale. When the microtubule density is above the critical

concentration, microtubules transition from disordered to highly ordered and nematic phases. Also, we have seen evidence that microtubules restructure their initial uniform distribution of motor proteins as they move in bundles.

Experimental Details

In this *in vitro* experiment, the substrate is a lipid bilayer. For the lipid bilayer, I chose 18:1 (Δ9-Cis) PC (DOPC)[1] for the 89.5 mol% of the lipid mixture and 10 mol% of 18:1 DGS-NTA(Ni)[2] and 0.05 mol% of 18:1 Cy5 PC[3] which is a fluorescently labeled lipid to check lipid bilayer formation using fluorescence microscopy. (Figure 3.1)

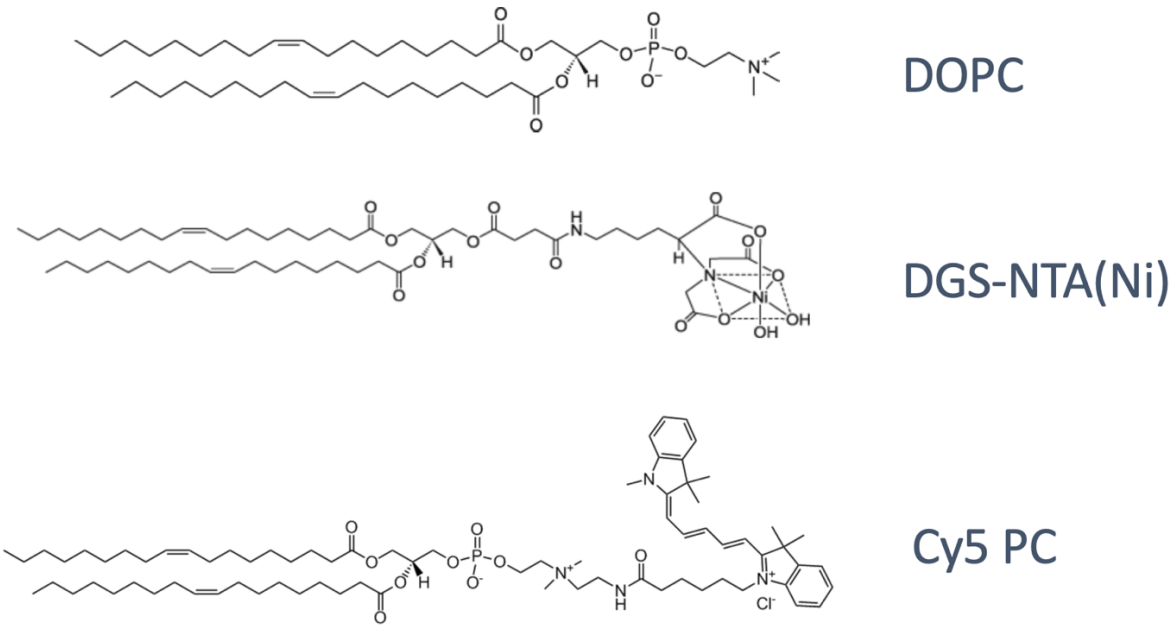

Figure 3.1: All the lipids in this experiment are 18:1, which indicates 18 carbons in the fatty acid chain and one double bond. The double bond shows that the lipid is unsaturated.

- *DOPC or 1,2-dioleoyl-sn-glycero-3-phosphocholine-N-(Cyanine 5)*
- *DGS-NTA(Ni) 1,2-dioleoyl-sn-glycero-3-[(N-(5-amino-1-carboxypentyl) iminodiacetic acid)succinyl] (nickel salt)*
- *Cy5 PC 1,2-dioleoyl-sn-glycero-3-phosphocholine-N-(Cyanine 5)*

This lipid mixture is fluid-like at room temperature. Motor proteins are attached to DGS-NTA lipids and are diffusive on the lipid bilayer, which is more similar to their *in vivo* behavior than a typical gliding assay. (Figure 3.2)

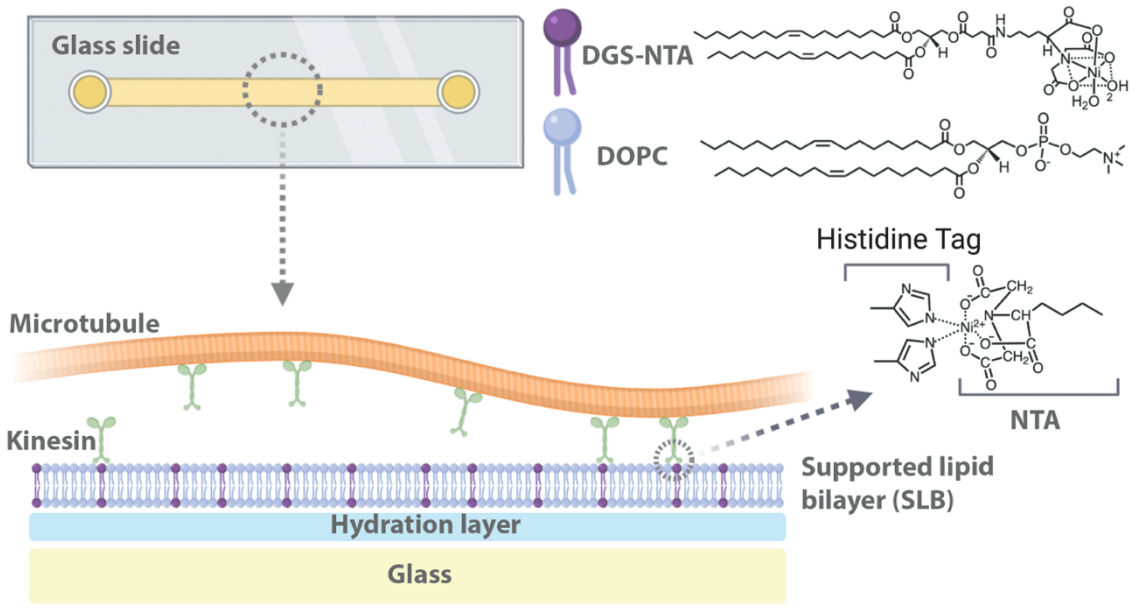

Figure 3.2: Schematic view of the experimental setup. A supported lipid bilayer (SLB) is formed on a hydration layer in the flow cell. Motor proteins are anchored to DGS-NTA lipids and microtubules gliding on motor proteins.

In this project, microtubules were labeled with rhodamine fluorescent dye, which allowed us to do fluorescence microscopy. We prepared microtubules by polymerizing homemade tubulin (a precise method and protocol can be found in the appendix). We did experiments over a wide range of microtubule concentrations from 0.05 mg/ml to 0.70 mg/ml. In all experiments, just 1.8% to 13% of microtubules were labeled, yielding clear and not overpowering bright images. Experiments were carried out in a standard flow cell constructed using a double sided adhesive sheet (*GRACE Bio-Labs*) with a thickness of 0.12mm.

Measuring motor diffusion in the membrane

In a typical gliding assay, microtubules glide on motor proteins, but in our experiment, motor proteins are not immobile compared to the gliding assay experiment. We used the Fluorescence Recovery After Photobleaching (FRAP) technique to find the diffusion constant of the bilayer-coupled motors.[45], [73]perform this measurement, fluorophore-tagged molecules are stimulated by a 488 nm laser suitable for GFP's 489 nm excitation peak, causing photobleaching. Although photobleaching is irreversible, the photobleached molecules diffuse away from the bleached area and are replaced by diffusive non-photobleached molecules. Therefore, the bleached region recovers its fluorescence over time. We can find the recovery time by measuring the time-dependent intensity. (Figure 3.3)

The imaging and photobleaching were carried out on a confocal laser scanning microscope (Zeiss LSM 880) using the ZEISS ZEN imaging software. The selected region for photobleaching was a circular area with a diameter of 32.6μm. We did imaging on an unbleached region (same size region) and then used it to normalize the bleached region's intensity as a time function. The normalized power is fitted to the Soumpasis diffusion equation[74], to calculate the diffusion constant. In the Soumpasis diffusion equation, ω is the diameter of the bleached area, and $\tau_{1/2}$ is the intensity half-life, which is found to be 155.7 s.

$$D = \omega^2 / \tau_{1/2}$$

In this experiment, the measured diffusion constant for motor proteins was D_{KIN} = 1.72 ± 0.27 $\mu m^2/s$ which is less than the diffusion constant of lipids in the fluid bilayer as expected and similar to other reported measurements.[75] Dr. Joseph Lopes previously measured the diffusion constant for our lipid bilayer as 9.01 ± 0.58 $\mu m^2/s$.[44]

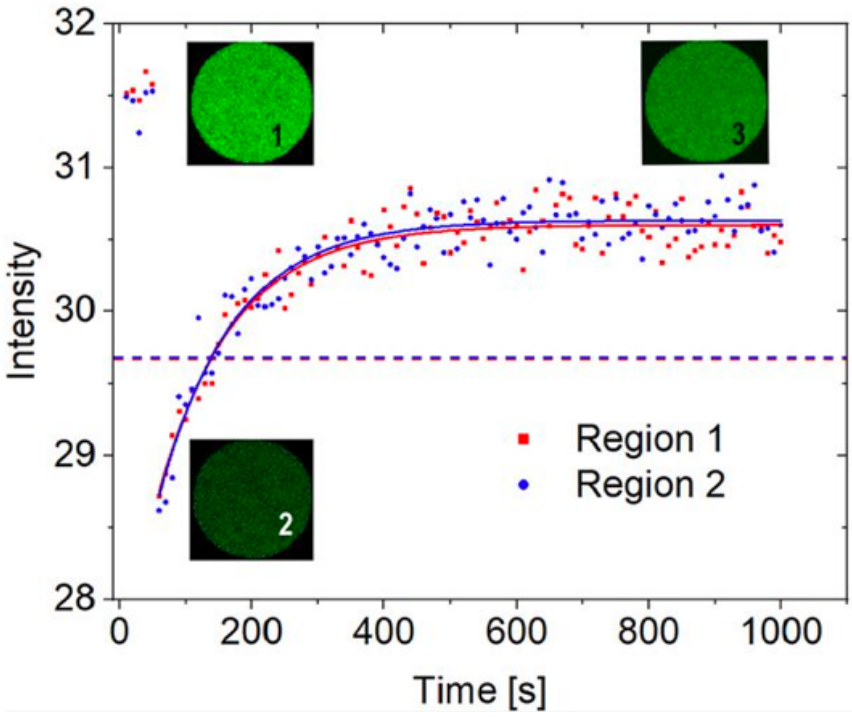

Figure 3.3: Fluorescence Recovery After Photobleaching (FRAP) is used to measure kinesin lateral diffusion in the lipid bilayer DKIN = 1.72 ± 0.27 $\mu m^2/s$. In the figure, FRAP images are shown, indicating (1) fluorescence intensity before photobleaching, (2) immediately after bleaching, and (3) after recovery.

Results

Active Bundling

Microtubules bundle together in the presence of depletion force, and this bundling is referred to as microtubule snuggling in the literature.[43] The depletion-induced bundling dampens the velocity of microtubule gliding as well.[43] In this experiment, diffusive substrate promotes active bundling without affecting the activity of microtubules. We called this term active bundling in microtubules. In the figure below (Figure 3.4), we compared the glass substrate to the lipid bilayer. The only difference is the mobility of the motor proteins. The experiment below has a high microtubule concentration (0.27 mg/mL), and only 6.9% of microtubules are labeled with Rhodamine fluorescent dye. In these experiments, I did not use a crowding agent such as PEG to exert depletion force. These experiments let us compare the effect of substrate and diffusing motor. In figure 3.4 (left), microtubules tend to cross over and are isotropic; however, by only changing the substrate in figure 3.4 (right), they are more likely to make active bundling and dynamics lanes of microtubules, even in the absence of depletants.

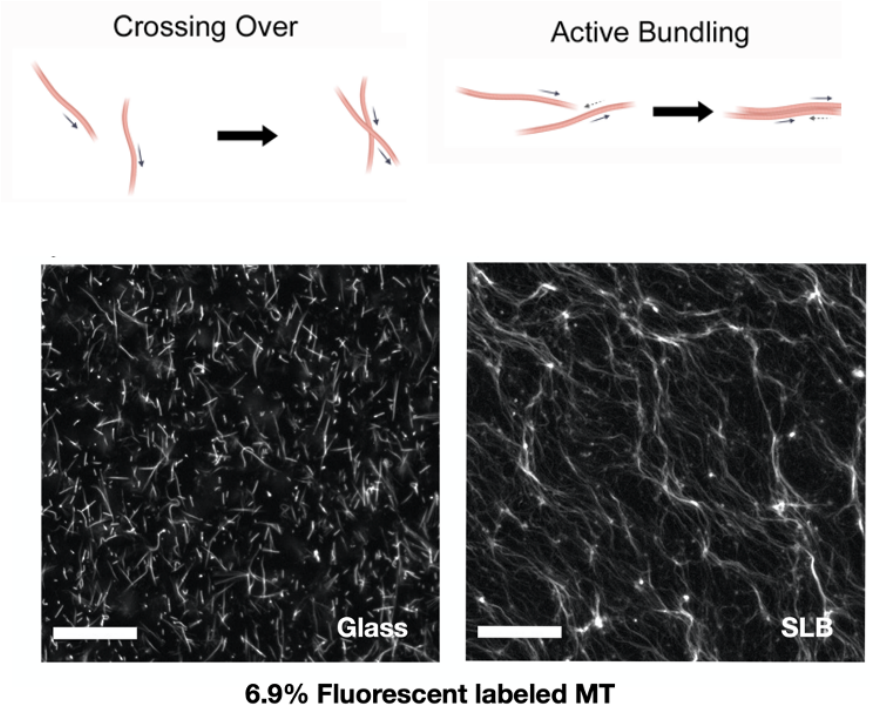

Figure 3.4: Fluorescence images of microtubules gliding on glass vs. the supported lipid bilayer (SLB). Microtubule concentration in both experiments was 0.27 mg/mL (6.9% of the filaments fluorescently labeled) with a kinesin concentration of 300 nM. Each panel overlays ten consecutive frames (total time = 50 s). On the left, microtubules gliding on glass without depletants are isotropic

and exhibits widespread crossing behavior. On the right, gliding on a lipid bilayer, microtubules display active bundling and collective motion. Scale bar 50 μm.

Microtubule dynamics and non-equilibrium phase diagram

I calculated V_{rms} for three different ATP concentrations (0.05mM, 0.1mM, and 0.5mM) and compared the calculated velocity to the Michaelis-Menton curve.[76] V_{rms} of microtubules' filament were derived using the Particle Image Velocimetry (PIVLab) application on MATLAB.[51], [77]–[79]

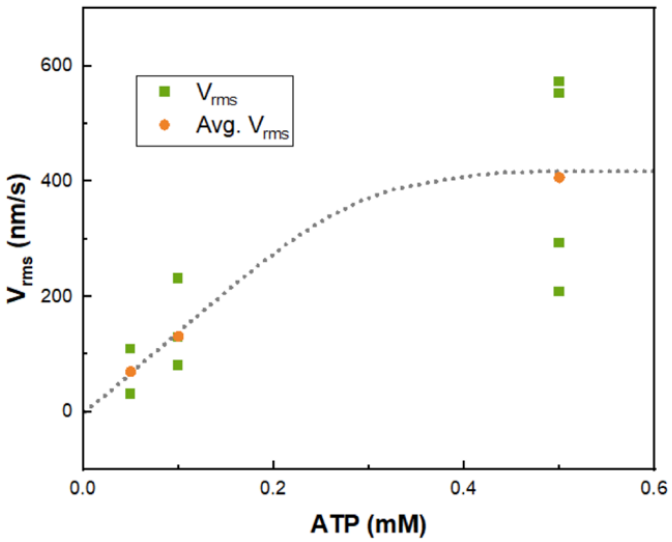

Figure 3.5: V_{rms} of microtubules as a function of ATP concentration Dashed line is a guide for the eye. Kinesin concentration is 300nM.

The concentration of microtubules was varied to study the phase transition from ordered to disordered behavior and to explore different phases. Results show that the system transitions from disorder to order as we increase microtubule concentration. In medium microtubule concentrations, dynamic apolar lanes appear, and nematic order is observed for a densely packed microtubule system. We divided the phase diagram into four states: isotropic, lane formation, the coexistence of lane formation and nematic order, and nematic order. (Figure 3.6 and 3.7)

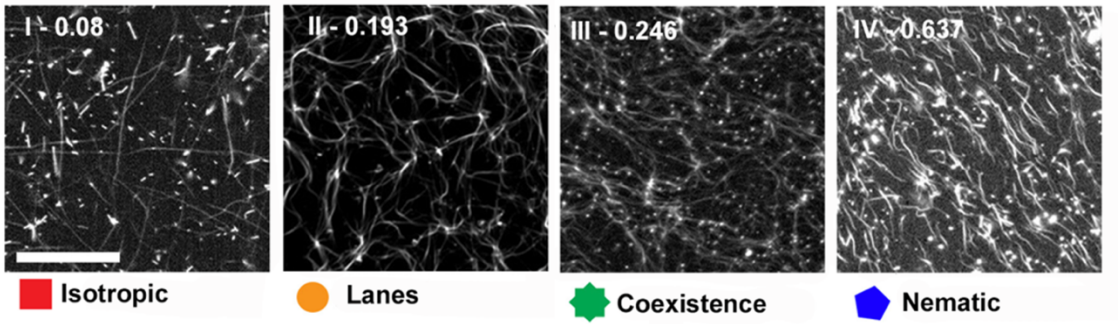

Figure 3.6: The emergence of global nematic order and locally ordered lanes. Panels representative fluorescence micrographs for the steady-state behavior of the system under different conditions. Each image panel shows a combined stack of 100 frames recorded 60 min after the start of the experiment; this visualization highlights the collective motion. 1.8 to 13% of microtubules are fluorescently labeled and visible. (Concentration of labeled microtubules 0.0125 mg/mL). A steady-state global nematic alignment predominates at higher microtubule densities, whereas lower microtubule concentrations produce apolar lane formation. (Scale bar, 50 μm.)

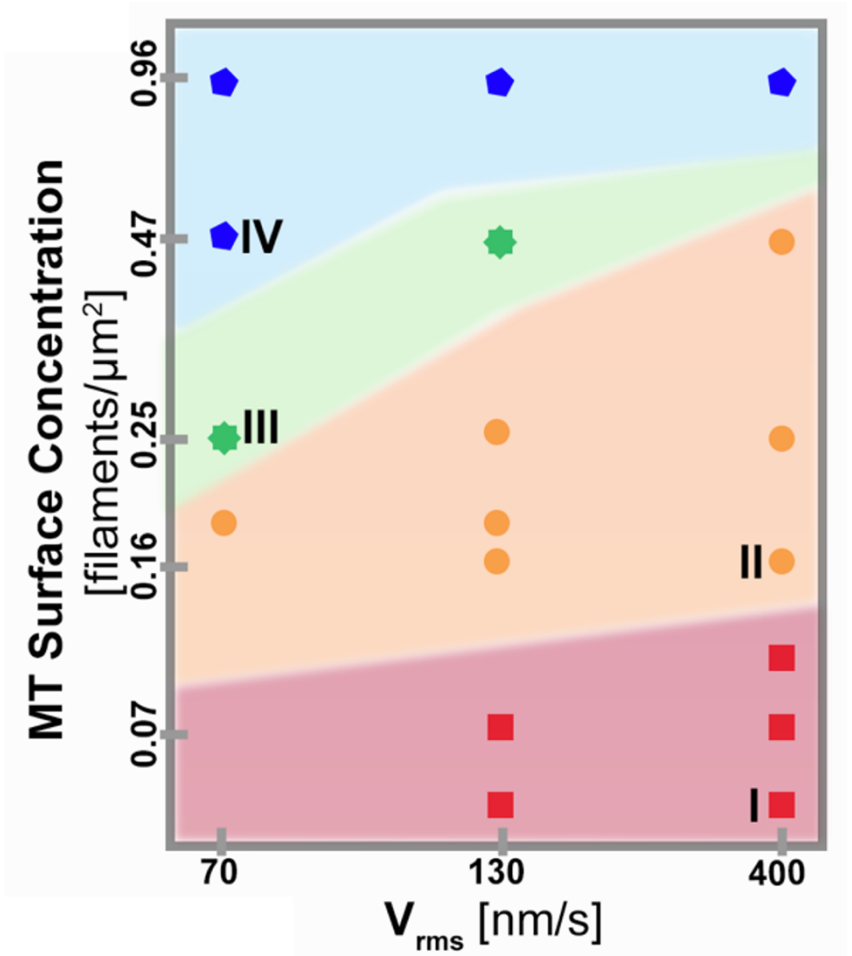

Figure 3.7: Nonequilibrium phase diagram demonstrating the effects of microtubule concentration and ATP concentration on the collective motion of membrane-bound microtubules.

I calculated the nematic order parameter between 0 (disordered) and 1(highly ordered) to study order in our system and associate different concentrations to a state. For measuring order parameters, I made a binary stack of frames and used the "OrientationJ" plugin on ImageJ to find the angular distribution of microtubules. A histogram of angles in a bin size of 5 degrees for each frame is measured. The population of tips in every bin resembles a vector, and by adding all the vectors together, we can find the order parameter of each frame. This method is published by Inoue et al.[43]

$$S = \frac{1}{N}\sqrt{\left(\sum_{i=0}^{36} R_i \cos 2\theta_i\right)^2 + \left(\sum_{i=0}^{36} R_i \sin 2\theta_i\right)^2}$$

Here S is the order parameter, *N* is the number of angles (angle bins), *R* is the bin frequency in each container, and θ is the bin angle.
Using this method, for regions of 250*μ*m*250*μ*m, we calculated order parameter, and we used the following threshold to determine the state of the order:
Nematic S > 0.25, Coexistence 0.20 < S < 0.25, Lane formation 0.10 < S < 0.20, and Isotropic 0 < S < 0.10.

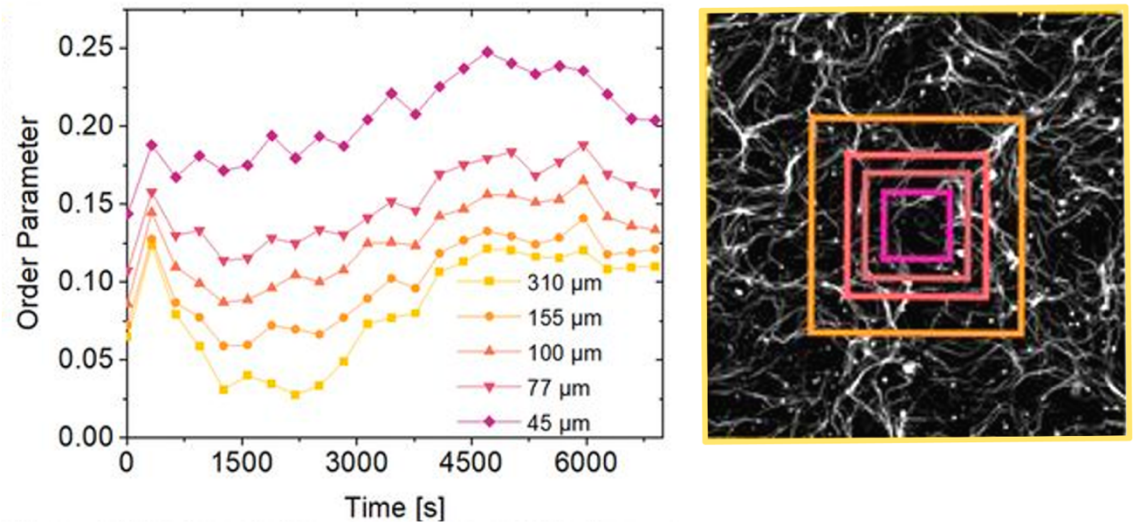

Figure 3.8: Measured order parameter as a function of time for different sizes of regions in the same experiment. Size of regions respectively are: 310μm ´ 310μm, 155μm ´ 155μm, 100μm ´ 100μm, 77μm ´ 77μm, 45μm ´ 45μm. As the region's size is decreased, the order parameter increases, and it verifies local order in the lane formation phase.

Using the same order parameter technique, we found that after we flow materials into the cell, it takes approximately 30 minutes for phases to form. Even when we don't have a global order, we can see the local lane formation phase by changing the region of interest (ROI) and making it smaller. In figure 3.8, we measured order parameters for different sizes ROIs; yellow is 310*μ*m*310*μ*m, showing a low or not

globally ordered parameter. We decrease the ROI size to 45μm*45μm, and we see an increase in the order parameter (magenta color) which verifies local lane formation and locally ordered phase.

Bidirectionality of microtubule lanes

Previously published studies on actin by Alfredo Sciortino and Andreas R. Bausch show a high-density actin gliding assay on a fluid lipid bilayer exhibiting the emergence of polar lanes in a nematic-like phase.[72] Also, several studies on bacteria show polar lanes and polar growth of bacteria in high density.[50] Considering all previous works on a similar system but with different rod-shaped filaments, a polar lane in high density is expected. However, the microtubule lanes that we observed were bidirectional and apolar. (Figures 3.9 and 3.10)

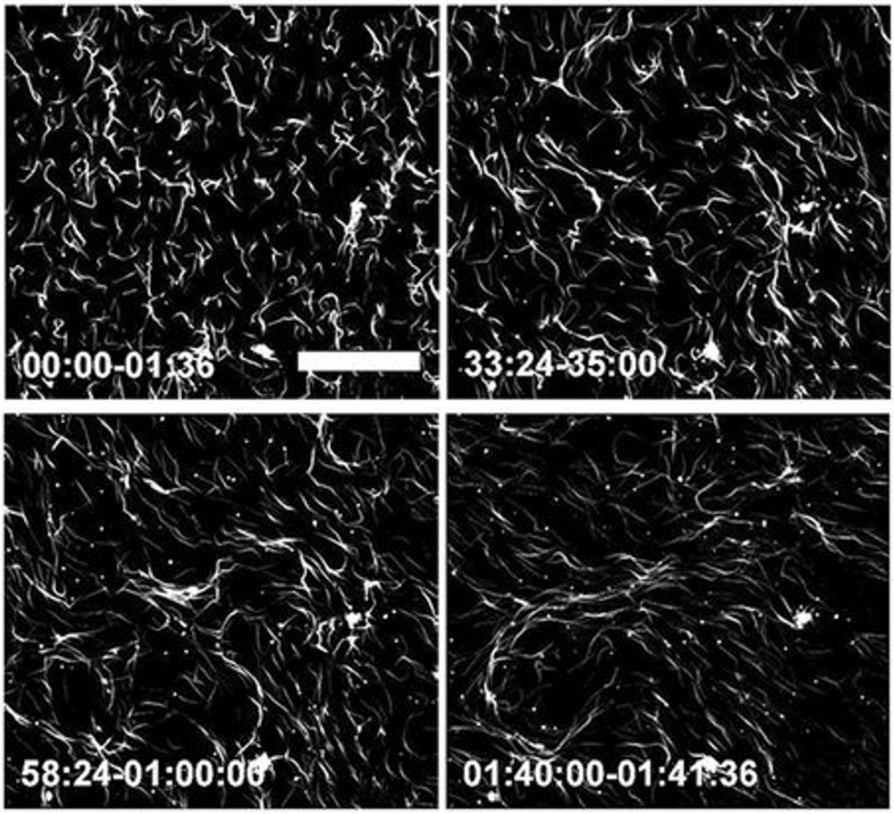

Figure 3.9: The time sequence of fluorescent-tagged microtubules shows the lane formation process during 48 min 30 sec. (6.9% of the filaments are fluorescently labeled). Each image is a stack of 10 consecutive image frames. After 30 min, local alignment and dynamic apolar lanes begin to form and gradually become more ordered. microtubule concentration = 0.18 mg/mL and kinesin concentration = 300 nM. (Scale bar, 50 μm.)

This finding was new, and to quantify the polarity of the lanes, I measured the total flux across a plane in the lane of microtubules for different randomly selected regions. When microtubules crossed from the right to the left, I counted them as

+1, and when they traveled from left to right, I counted them as -1. The total flux is near zero, showing bidirectionality for all four phases. (Figure 3.10)

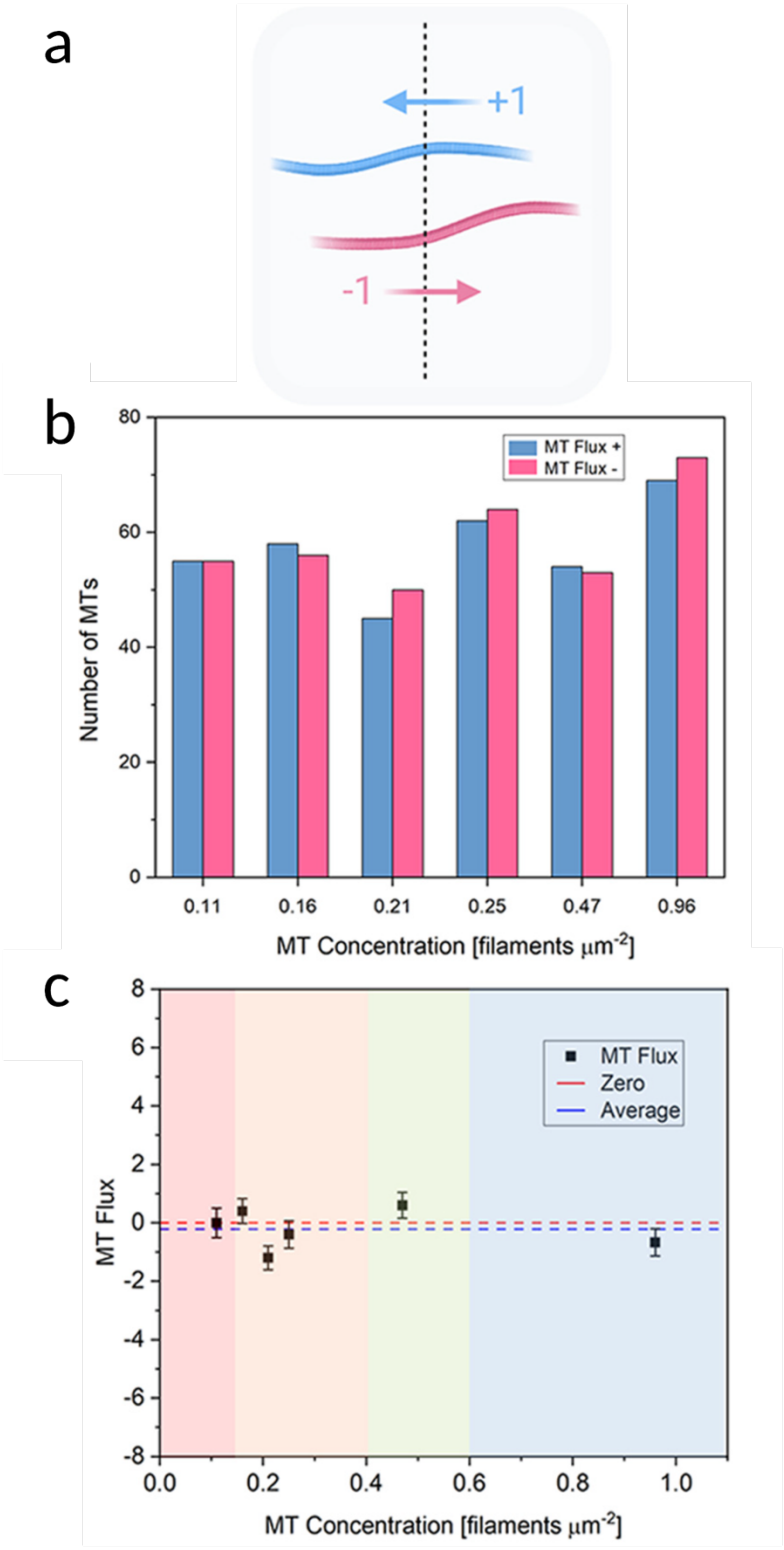

Figure 3.10: Top) Schematic showing gliding microtubule flux measurements across a plane indicated by the dashed line. Middle) Bar chart plotting the total number of microtubules crossing in either the positive or negative direction (+1 or –1). For each microtubule concentration, five regions on the microscope slide were selected. In each area, the microtubules were counted, crossing the plane over five different 10-s time intervals, and combined. Bottom) Total flux as a function of microubule concentration calculated from data in G. The graph indicates phase using colors corresponding to the phase diagram in figure 3.7.

Motor protein redistribution in the lipid bilayer

Another finding from this project was that microtubules redistribute motor proteins in the lipid bilayer. As the microtubules move in the lanes described in the previous sections, they redistribute motor proteins. We verified this by observing a uniform motor protein distribution at the beginning of the experiment. After a few minutes of microtubules gliding on diffusive motor proteins, it is possible to observe the formation of lanes of motor proteins, as they are no longer uniformly distributed. Figure 3.11 (a-c) shows how a narrow trail of kinesin is left behind as microtubules pass the point indicated in figure 3.11. This phenomenon is challenging to capture because motor proteins cannot be seen individually (tiny and low intensity).

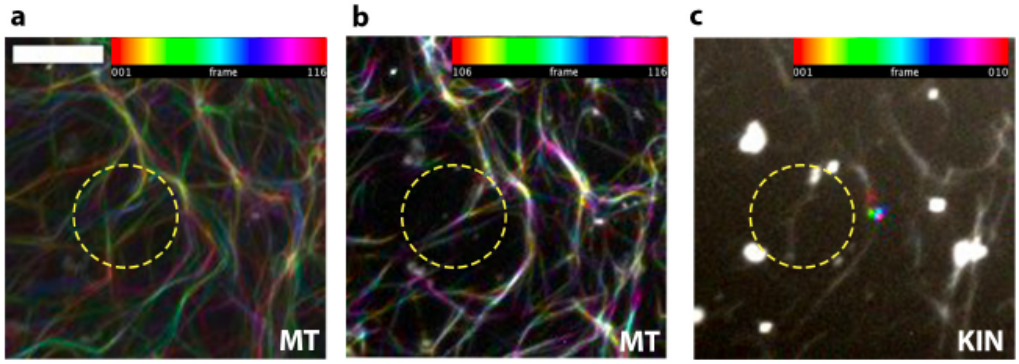

Figure 3.11: a) A color-coded stack of microtubules in 116 frames. b) A color-coded stack of 10 last frames of microtubules, their position in the last 10 frames indicated with the yellow circle. c) A color-coded stack of kinesin showing the trail left behind.

We tried this experiment without microtubules as a control experiment to see if motor proteins restructure on the lipid bilayer independent of microtubules. We observed that they remained uniform throughout the investigation. (Figure 3.12)

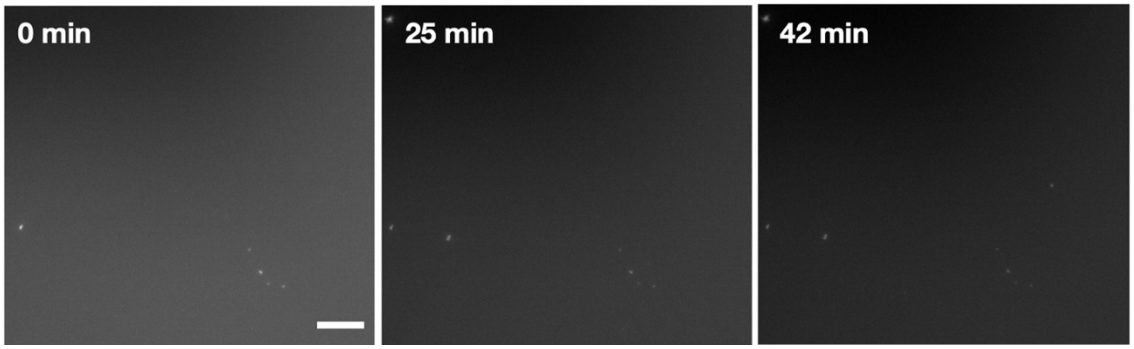

Figure 3.12: GFP-tagged motor proteins on a lipid bilayer without microtubules. The distribution of motor proteins is uniform at the beginning of the experiment, and during 42 min of imaging, the motor distribution remains uniform. Scale bar 100μm

Using ImageJ software, we could check the intensity histogram count of motor proteins throughout the experiment. As we expected, the final image is dimmer than the initial frame because of the photobleaching of motor proteins. (Figure 3.13)

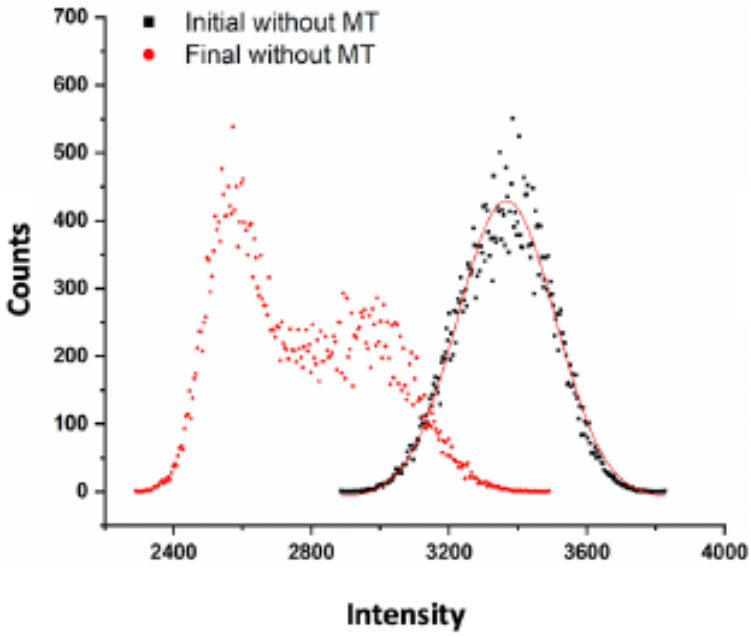

Figure 3.13: Intensity histogram count of GFP labeled motor proteins shows that initially, motor proteins are brighter, and because of photobleaching during the experiment, they get dimmer as expected.

Thus, the control experiment confirms that motor proteins stay uniform in a flow cell without microtubules. In another experiment, we added unlabeled microtubules (invisible) and only did imaging on motor proteins. Motor proteins were initially uniformly distributed; after 16 min and 30 sec, they formed some lanes.

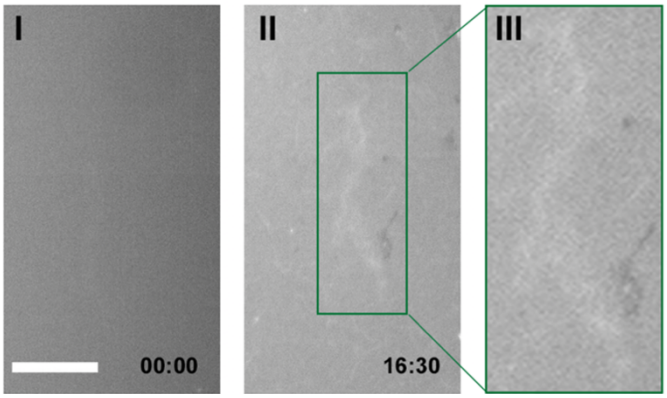

Figure 3.14: An example of kinesin redistribution in the lipid bilayer substrate in response to a microtubule-enriched lane. At time t = 0 s (I), GFP-labeled kinesin in the membrane is very uniform in distribution. After 16 minutes and 30 seconds, significant inhomogeneities emerge in kinesin distribution in the same area (II, III). The kinesin distribution is not correlated with individual microtubules. Scale bar 20μm

I used the same method described for the control experiment and plotted the intensity histogram count; however, we have photobleaching throughout the investigation. Still, the final frame is brighter than the initial state, showing possible motor protein clustering.

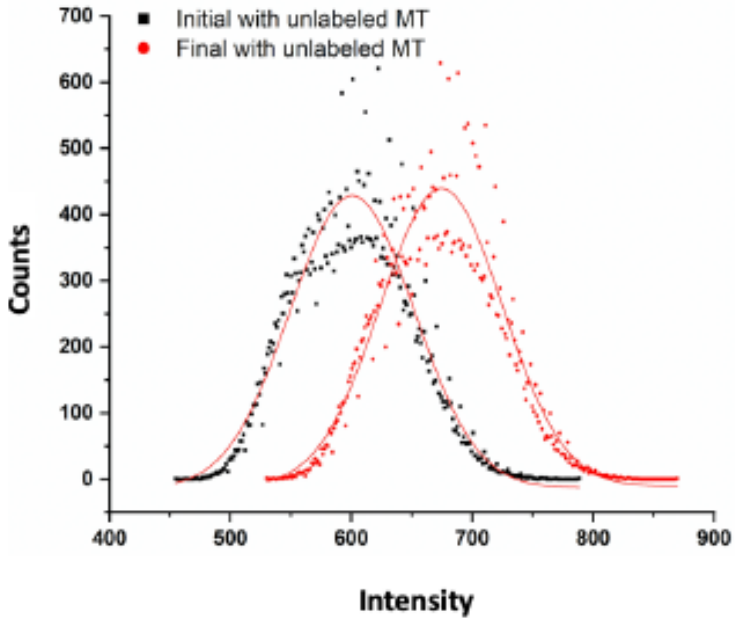

Figure 3.15: In an experiment with unlabeled microtubules and labeled motor proteins, intensity histogram count and its gaussian fit show motor proteins get brighter during the investigation for a small region even when photobleaching is happening, which confirms the restructure of motor proteins due to microtubules' lane formation.

Global rotation of microtubules

We noticed a global counterclockwise rotation in microtubules in a flow cell with an imaging system from the top. The rotation process is slow compared to other publications[56], [80], but the direction is the same. Our system's rotation rate is about 20 degrees/hour and counterclockwise. (Figure 3.16) The reason for the rotation is potentially related to the chirality of microtubules and the packing of tubulin dimers.[56], [80]

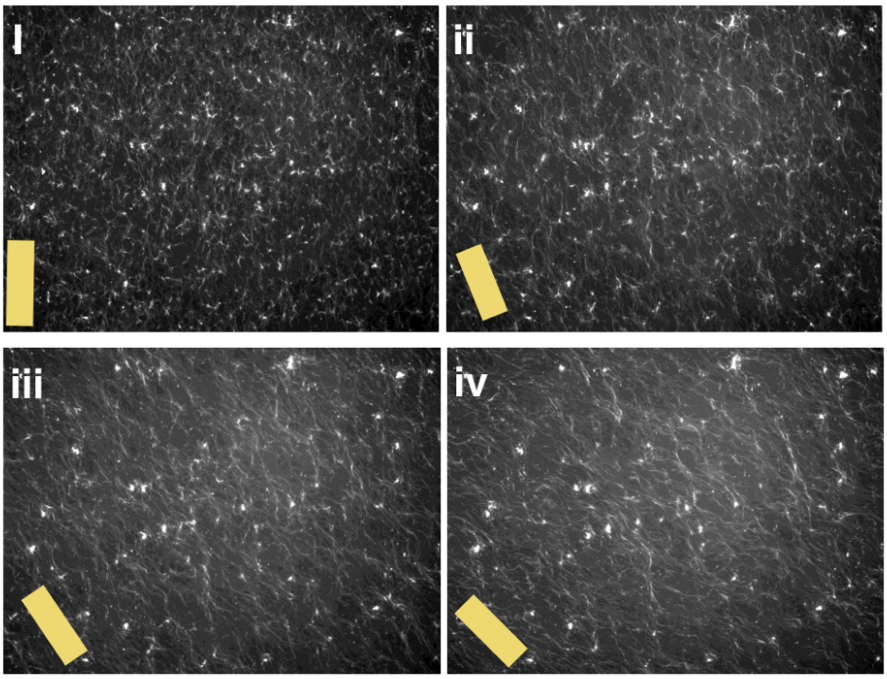

Figure 3.16: Counterclockwise global rotation of GTP microtubules. Imaging from the top showing 20-degree rotation per hour.

To learn more about the chirality of the microtubules I performed TEM imaging of GTP and GMPCPP microtubules. The results showed that the tubulin dimers and their pitch angle could be clearly identified and specified. The lack of contrast is an issue for TEM microscopy in samples without heavy metals. Uranyl acetate is a uranium salt that produces the highest electron density and high contrast for TEM microscopy on biological samples.[81] Using a staining protocol from Prof. De Alba's lab at UC Merced, I stained microtubules with uranyl acetate for TEM imaging.[82] I used a 1mg/mL concentration of microtubules on a carbon-coated TEM grid. I added 4μL of microtubules on top of a grid, waited 5-10 min, and washed it three times with 40μL of HPLC water. After washing, I stained the microtubules with three 40μL droplets of Uranyl Acetate and left the grid overnight

under the fume hood to dry before TEM microscopy. (Figure 3.17). A Talos F200C G2 Transmission Electron Microscope was used to perform the TEM.

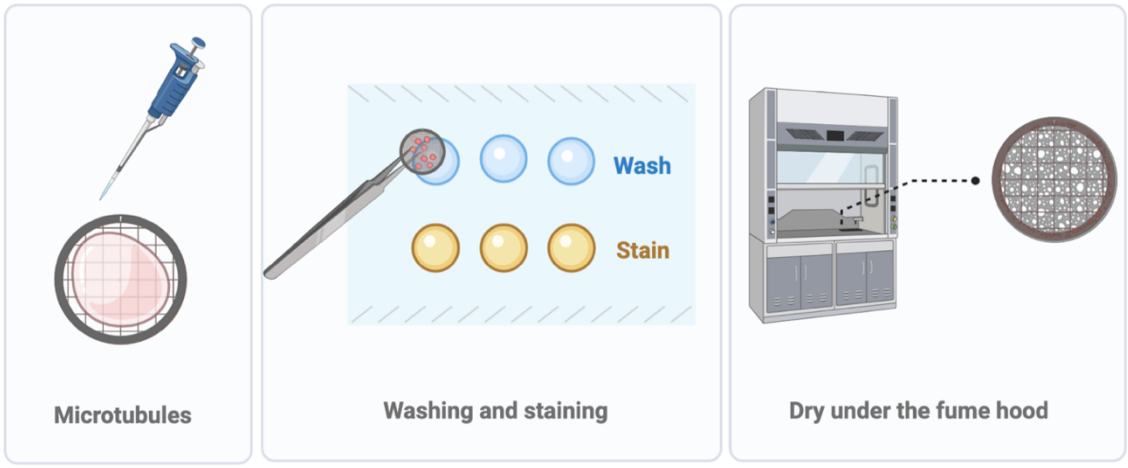

Figure 3.17: TEM sample preparation. From left to right, microtubules are added to the grid and waited 10 min. The TEM grid was washed with HPLC water and stained three times with uranyl acetate. After the staining procedure, the sample stayed under the fume hood overnight to dry. Image made on BioRender.

Negatively stained microtubules appear dark in TEM images. In figure 3.18, we can see TEM images of the GTP and GMPCPP microtubules.

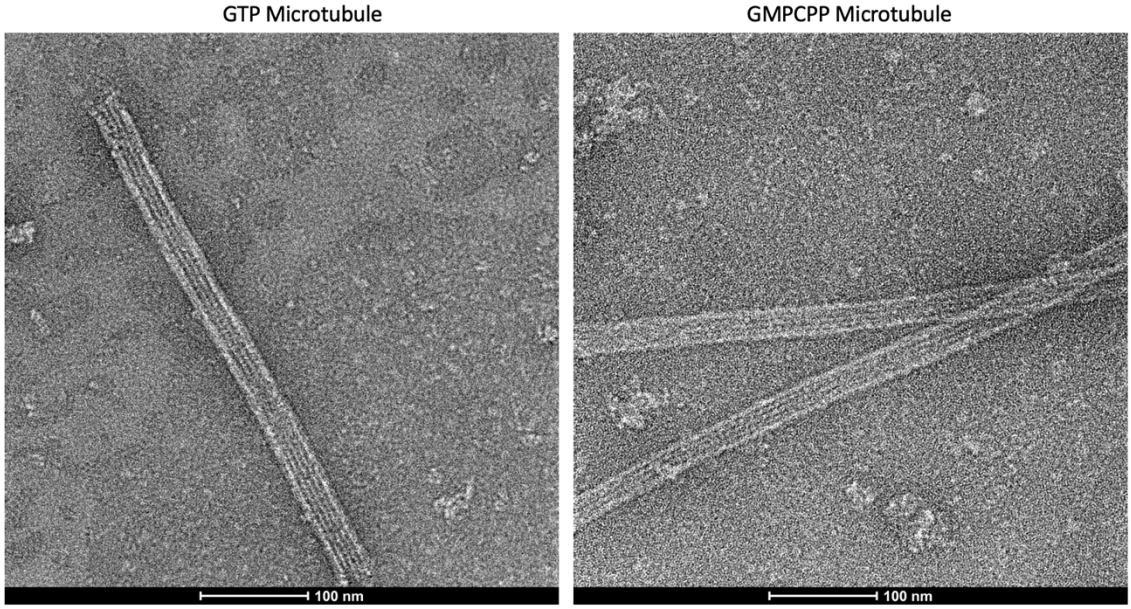

Figure 3.18: Transmission Electron Microscopy (TEM) image of GTP microtubule. The microtubule is negatively stained by uranyl acetate, and the dark spots show the stained proteins.

The negatively stained microtubules are flattened and appear thicker than 25nm.[31], [32], [34] , and protofilaments of microtubules can be observed as a dark spot. The pitch angle, which measures microtubule chirality, is defined in figure 3.19, and I measured it for over 12 different TEM images of GTP and

GMPCPP microtubules. For GTP microtubules, the measured pitch angle is 8.5176±0.392, and for the GMPCPP microtubules, the pitch angle is 15.5032 ±0.283.

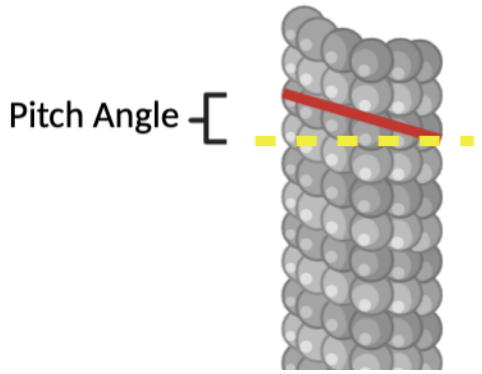

Figure 3.19: Schematic view of a microtubule and the pitch angle. Image made on BioRender.

These findings may help to explain the rotation that has been observed. However, since the pitch angle for GMPCPP microtubules is almost double that of GTP microtubules, it is interesting to compare the rotation of GMPCPP microtubules on the lipid bilayer. These results provide valuable insights for further investigations.

Conclusion

This chapter describes experiments focused on microtubule gliding on diffusive motor proteins on a lipid bilayer substrate. The results demonstrate a transition of the active microtubule state from isotropic to nematic, focusing on the dynamic apolar lanes and active nematic. These different states are susceptible to microtubule concentration. By increasing the microtubule concentration, the system becomes more and more ordered. The first phase after isotropic is the formation of dynamic apolar lanes. The nematic phase is distinct from the active nematic system introduced by Sanchez et al.[10], in which microtubules are connected with crosslinkers. In a gliding assay on a glass substrate with immobile motor proteins, microtubules tend to cross over each other and are in an isotropic state without crowding agents. However, motor proteins are diffusive on the fluid lipid bilayer, microtubules cross each other more, and the lipid bilayer promotes active phase formation by inducing filament-filament alignment. We measured the order parameter for different regions of interest (ROIs), which increased as we decreased the ROI size. This result shows that even when there isn't a global order parameter in the lane formation state, there is still a local order parameter. Moreover, we observed the redistribution of motor proteins with the gliding of microtubules on a lipid bilayer.

All these findings are supported by active hydrodynamic theory and simulations using a continuum model obtained from coarse-graining a collection of motor-propelled rods.[83] This new self-organizing behavior can lead us to configurable materials emphasizing colocalization and self-repairing structures with mechanical work. Our paper on this work, *"Active nematic order and dynamic lane formation of microtubules driven by membrane-bound diffusing motors,"* has been published in the Proceedings of the national academy of sciences (PNAS).[83] In future work, with the collaboration of different research groups, we will investigate the global rotation of microtubules.

Acknowledgments

I thank all the authors of the "Active nematic order and dynamic lane formation of microtubules driven by membrane-bound diffusing motors" published in 2021 at PNAS. Also, David Quint for his help with image analysis. The University of California Merced Imaging and Microscopy Facility (IMF) and Kennedy Nguyen with TEM microscopy training and assistance. The data in this work were partly collected with a confocal microscope acquired through NSF MRI Award DMR-1625733. We acknowledge generous funding from the NSF DMR-1808926. Center for Cellular and Biomolecular Machines at the University of California, Merced (HRD-1547848) also supported the project. I also acknowledge BioRender, I made figures of this chapter using BioRender.

Chapter 4

Tuning the active length of microtubule-based active nematics

Introduction

In 2011, Nedelec et al.[5] discovered that microtubules and motor proteins could create self-organizing patterns using kinesin clusters instead of individual kinesins. Later, Sanchez et al.[10] was the first to present the creation of an active nematic structure using the same active nematic mixture but assembled at an water-oil interface. Depletion forces forced microtubules into bundles, and because they were confined in 2D, they exhibited nematic order. In this microtubule-based active nematic quasi-two-dimensional, defects with +1/2 charge (comet-shaped) and -1/2 charge (trefoil) are frequently observed. These defects are constantly created and annihilated due to the activity present in the system.[10], [11], [61]
In this chapter, the active nematic experimental setup and the importance of ATP and silicone oil viscosity on the morphology of active nematic will be discussed.

Background

Several studies, directly and indirectly, investigate active length scale change in microtubule-based active nematic. There are research studies on the effect of the thickness of the oil layer in active nematic systems and the oil's viscosity.[84], [85] Also, there are studies on different concentrations of ATP in the network and its relation to the dynamics of the active nematic phase. We need to know about two popular distinct experimental setups for sandwiching the active layer at the water and oil interface to discuss the previously published studies.
The first method is the flow cell method depicted in figure 4.1 In the flow cell method, there is a layer of an engineered oil, and the active network flows on top of the oil layer in an aqueous layer. [11], [61]

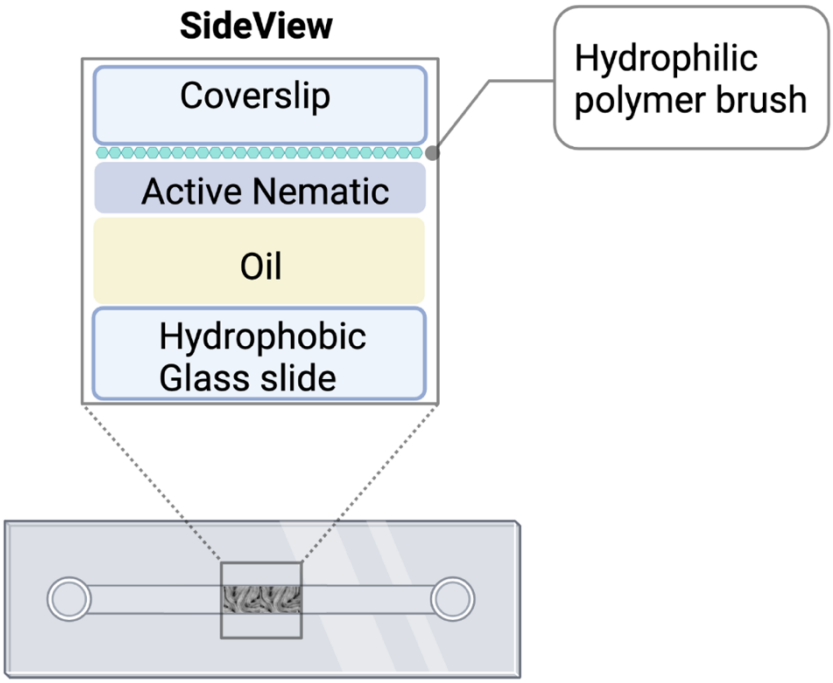

Figure 4.1: Schematic view of the flow cell method. In this method, the active nematic layer is sandwiched on top of the oil layer.

The second method is the inverted method, in which a PDMS well is attached to a hydrophilic glass slide, and a layer of oil is located on top of the active network.[85] I used the inverted method for the work described in this chapter and will discuss the details of the experimental setup.
Kristian Thijssen et al. studied the effect of the oil layer in the flow cell method, and they published the results in “Submersed micropatterned structures control active nematic flow, topology, and concentration.”, PNAS (2021).[84] Their publication indicates that the thickness of the oil layer underneath the active nematic can influence the active length scale. As we decrease the thickness of the oil layer, the active length gets smaller, and there are more defects in the same region of interest.

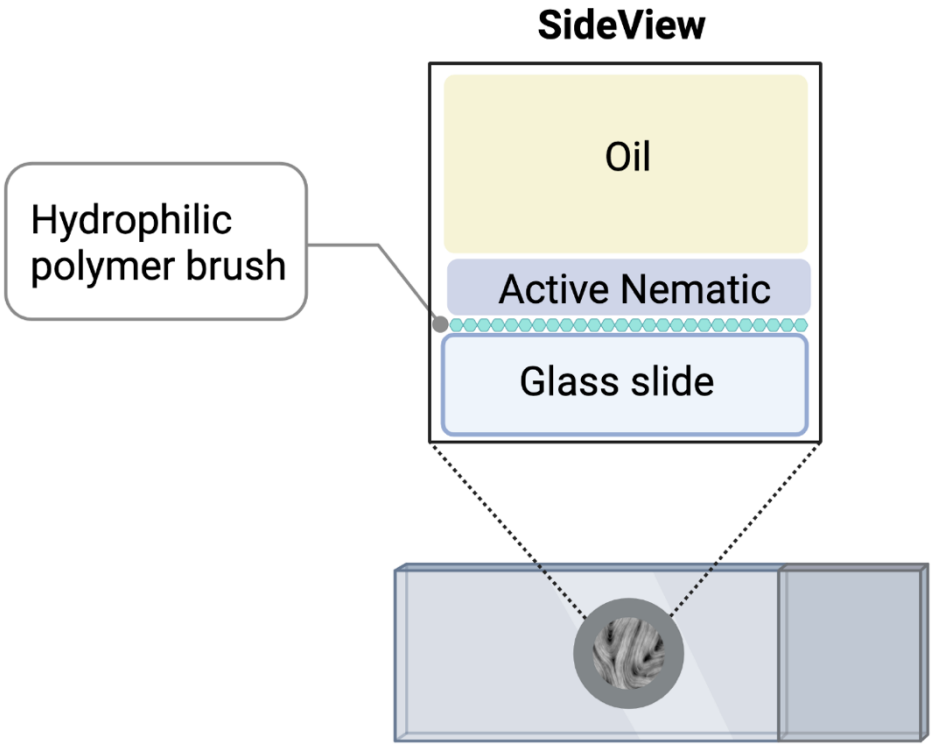

Figure 4.2: Schematic view of the inverted method. In this method, the active nematic layer is sandwiched underneath of the oil layer.

Guillamat et al.[85] published the inverted method and the effect of oil viscosity on top of the active nematic film. The paper is “Probing the shear viscosity of an active nematic film,” (2018).[85] The article shows that the higher oil viscosity decreases the active length and the lower oil viscosity with the same thickness results in a higher active length.
Also, Lemma et al.[61] demonstrated the effect of varying ATP concentration on active length, which alters the active stress exerted by kinesin motor proteins. Figure 4.3 shows that the active length scale at lower ATP is longer than for the high ATP experiments.

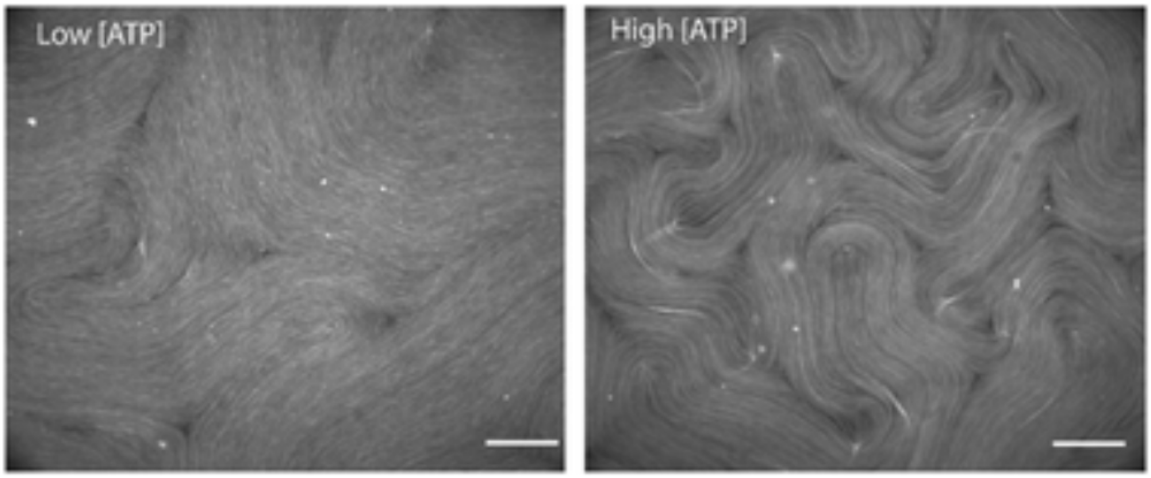

Figure 4.3: Microtubule-based active nematic with low and high ATP. The figure was adapted with permission from "Statistical properties of autonomous flows in 2D active nematics" by Linnea M. Lemma et al. at Soft Matter (2019).

In the following section, I will describe the experimental methods and the effective parameters for tuning active length in microtubule active nematic.

Experimental Details

Microtubule polymerization

Purified unlabeled tubulin from pig brain is purchased from PureSolutions at 20 mg/ml. GMPCPP microtubules are more appropriate in an active nematic because they are more stable and stiffer, which resemble liquid crystal molecules. I polymerized microtubules with only 4% fluorescently labeled tubulin (Rhodamine labeled tubulin purchased from cytoskeleton). 96% of the microtubule is made of unlabeled tubulin. Unlabeled and labeled tubulin are mixed on ice and incubated for 10 min. Centrifuge the tubulin mixture at 4 C and 352,700 x g for 10 min. The supernatant was removed and stored in a vial. Incubate supernatant with 0.6 mM GMPCPP (Guanosine-5'-[(α,β)-methylene]triphosphate, Sodium salt) at 37 C for 30 min.[51] Also, some of the microtubules for this project were purchased from the Brandeis Biomaterials Facility, and those microtubules are labeled with Alexa Fluor 647. GMPCPP has been used for polymerization in both microtubules, which are approximately 2 μm.

.

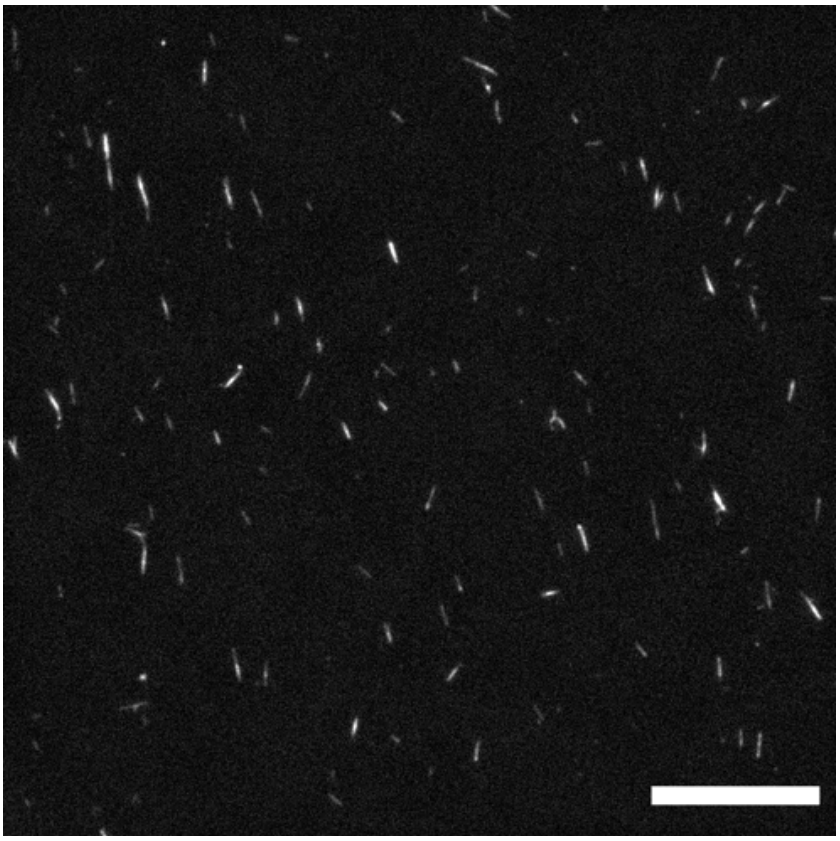

Figure 4.4: GMPCPP polymerized microtubules, 4% labeled with Rhodamine. Scale bar 30μm

Kinesin Streptavidin clusters

K401 motors are double-headed, attached with a helical stalk, and can be purified from *E.coli* following the protocol by Edgar C. Young[86] The two 401 amino acid segments make a two-headed dimeric motor.[87]Double-headed motors are processive, and they are faster than single-headed motors. K401 motors take approximately 100 steps before they detach from microtubules.[87], [88] In this setup, we want to use motor proteins as crosslinkers between microtubules, so they must be connected to microtubules from both ends. Biotin-Streptavidin binding is a strong binding and appropriate to attach four K401 and make a motor cluster. Kinesin-Streptavidin clusters or KSA is made of 24 vol% 0.7 mg/mL K401 motors, 27 vol% of 0.325 mg/mL streptavidin, and 3 vol% 5mM dithiothreitols (DTT) (to prevent aggregations) in 46 vol % M2B buffer (80 mM PIPES (1,4-Piperazinediethanesulfonic acid, pH 6.8), 1072 mM $MgCl_2$, 1 mM EGTA (ethylene glycol-bis(β-aminoethyl ether)-N, N, N′, N′-tetra acetic acid)).

Active MIX

Active MIX consists of KSA, microtubules, and ATP for the activity. Prepare MIX by adding KSA to 6 wt % 20kDa polyethylene glycol (PEG) to induce bundling of microtubules, 3 vol % ANTIFADE solution, and 5vol% Pyruvate kinase/lactic

dehydrogenase (PKLDH) at 70 mg/mL for ATP regenerative system. The ANTIFADE solution prevents photobleaching and includes AO1 (250 mM dithiothreitol, 65mM Catalase) and AO2 (750µM Catalase, 3mM Glucose Oxidase) in a 1:1 volume ratio. In addition, 20mM Trolox, another antioxidant used to reduce damage caused by fluorescence microscopy. To make the MIX active, add ATP and microtubule to MIX and let it form the network.

Water-oil interface

The active MIX needs to be sandwiched between the water-oil interface to confine in 2D and become an active nematic. We made a PDMS well for active nematic confinement with a diameter of approximately 5 mm.[51] To make PDMS well, we mixed elastomer base and elastomer agent in a ratio of 10:1 and degassed the mixture under a desiccator for 1 hour, and then cured. It is in the oven for 4 hours at 60 C. The glass substrate is coated with an acrylamide polymer brush to prevent proteins from sticking. To the glass slide and make the glass slide hydrophilic. The PDMS well is glued to the acrylamide-coated glass slide with UV glue. We added 60µl of Silicone oil with 685.6 (±11.7) mPa s viscosity. Eventually, we inject 0.75 µL of active MIX under the oil layer and wait approximately 1 hour for active nematic network formation and a better 2D phase.

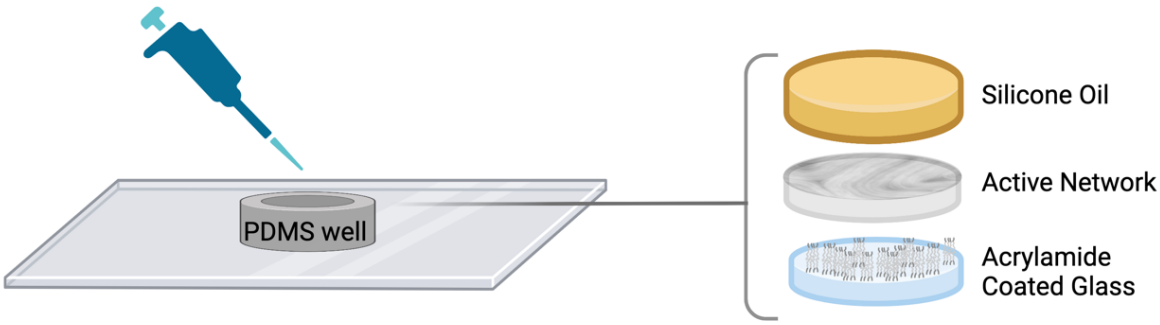

Figure 4.5: Schematic view of the experimental setup. Layers from the bottom to top show an acrylamide-coated glass slide, active nematic on the top, and a layer of silicone oil on top of the network. All the layers are confined in a PDMS well attached to the acrylamide-coated glass slide.

Imaging

Microtubules are labeled with Alexa 647 fluorescent label, and we did fluorescent microscopy with a Leica DM 2500 P fluorescent microscope and Hamamatsu ORCA-flash 4.0 LT CMOS camera, and a 5x objective. Image sequences were taken with 500ms exposure and 2s time interval between frames.

Results

Change in morphology due to activity

The experiment started with a saturated ATP level (1000mM). I used an ATP regeneration system composed of Pyruvate Kinase/Lactic Dehydrogenase or PK/LDH enzymes from rabbit muscle. Without an ATP regeneration system, the network stays active for 1-2 hours after adding ATP. In contrast, the ATP regeneration system keeps the network active for approximately 6 hours. Therefore, assuming ATP remains at saturation in long experiments needs to be more accurate in figure 4.6, I show the root mean squared velocity (v_{rms}) of microtubules in the active phase over a long period, measured using Particle Image Velocimetry (PIVlab) on MATLAB.[77]–[79]

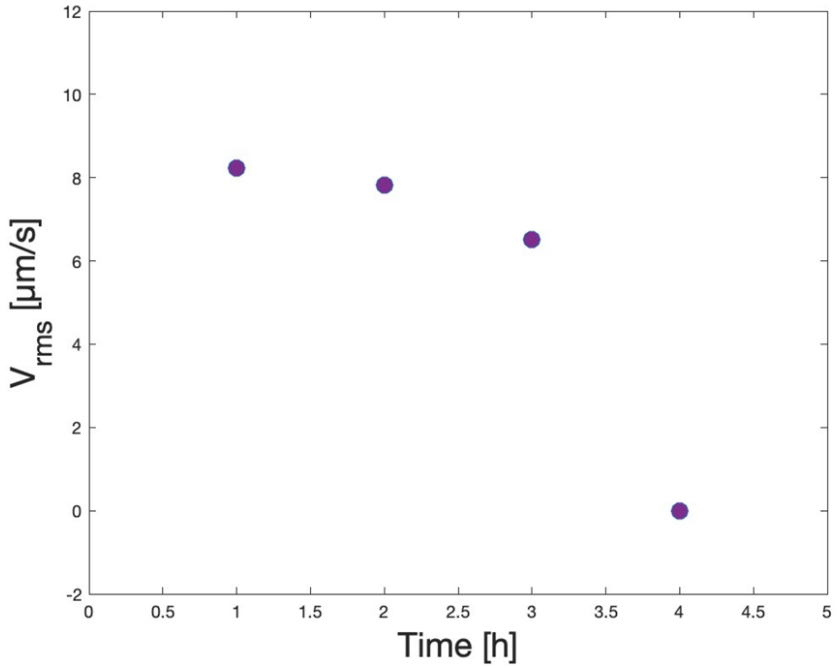

Figure 4.6: Root mean square velocity of microtubules starting one hour after adding the ATP to the network. Four hours after adding the ATP, the system runs out of ATP and is not mobile anymore.

In the long active nematic experiment, the root mean square (rms) velocity of the microtubule changes, and the morphology of the nematic phase also varies. We can recall that the active length scale balances elastic deformation and active stress. If the elastic stress in a system remains constant, the utilization of ATP will

cause the active stress within the system to change. Therefore, the active length will increase as the ATP is consumed to balance elastic and active stress. This increase in active length is necessary for the system to continue functioning properly, enabling it to compensate for the decrease in active stress resulting from ATP consumption. Different ways to find the active length scale in bulk include finding the mean defect separation, director correlation length, vorticity correlation length, or velocity correlation length.

In 2016, Hemingway et al.[69] published “Correlation lengths in hydrodynamic models of active nematics” in Soft Matter. The ways mentioned above to measure the active length scale were discussed in that work.

I used mean defect separation to measure the active length. Mean defect separation is calculated based on the areal density of defects. To find the areal density of defects, I counted the total +1/2 and -1/2 defects for four different regions (1066*1066 μm^2) in the active phase at different times in figure 4.7, I plotted defect count vs. time for both +1/2 and -1/2 defects.

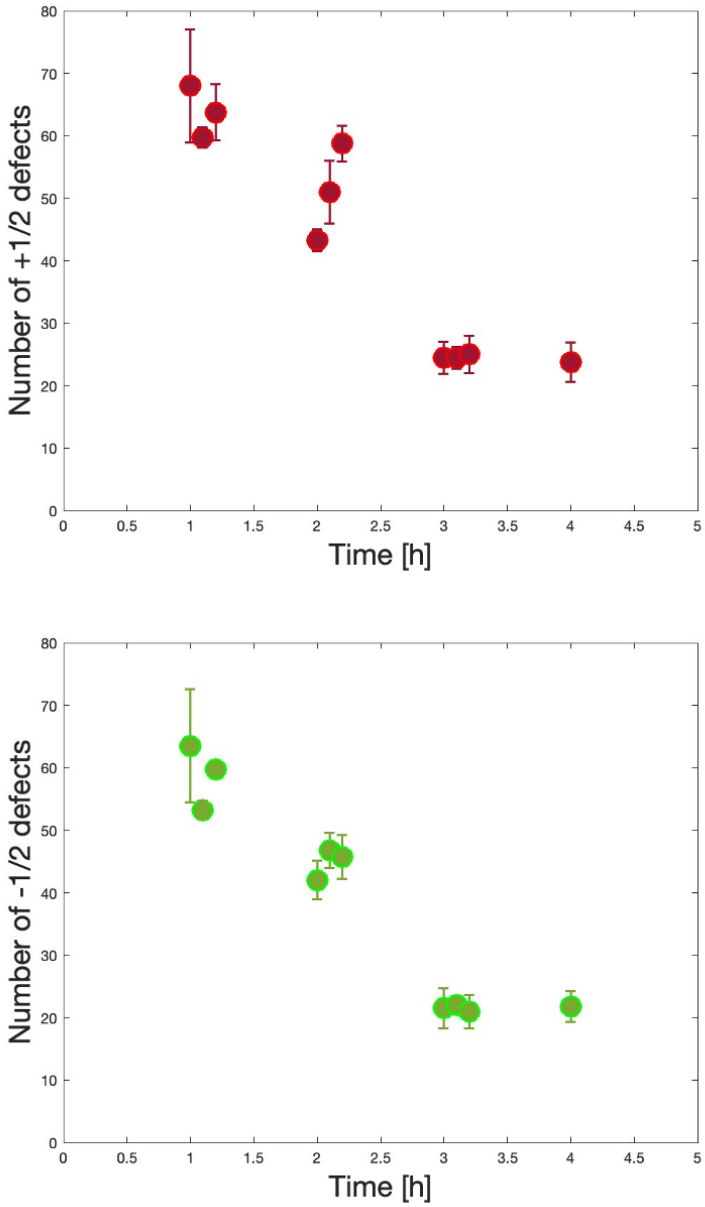

Figure 4.7: Number of semi-integer defects for four regions at every time stamp vs time.

Based on the defect counts plots, both +1/2 and -1/2 defects decrease as the motor proteins lose activity. Next, the defect density is calculated and plotted for the 1066*1066 μm^2 field of view.

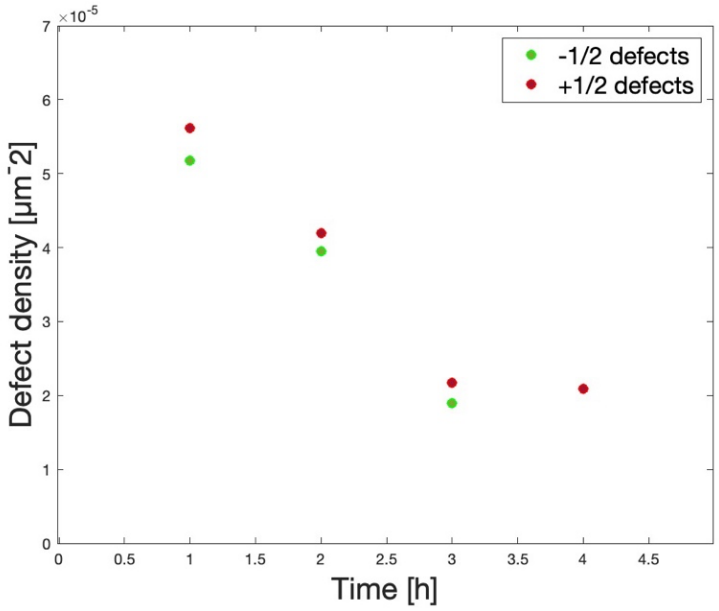

Figure 4.8: Total number of defects per field of view. The first three data points for each defect are the average of three different times (each 6 min apart) and a total of 12 regions. For example, the last data point for T=4h is a one-time stamp, and four areas for +1/2 and -1/2 defects.

The mean defect separation, *la,* is calculated using a method from Hemingway et al.[69] $l_a = \sqrt{\frac{1}{n_d}}$. In this formula is the areal density of defects, which we calculated earlier. The mean defect separation is plotted in Fig 4.9; as the network loses activity, mean defect separation increases. Four hours after adding the ATP to the network, I observed that the microtubules were immobile, and the average number of +1/2 and -1/2 defects was the same as each other.

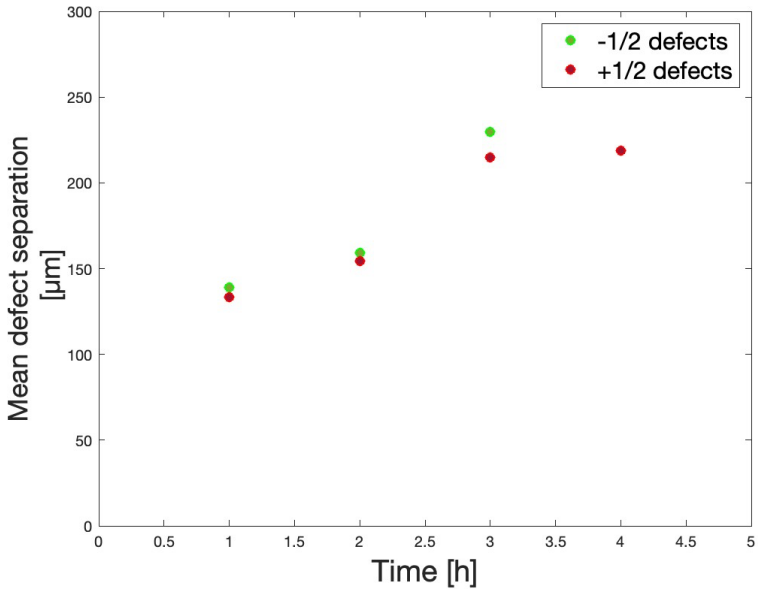

Figure 4.9: Mean defect separation calculated from the areal defect density shown in figure 4.6. for +1/2 and -1/2 defects.

Relaxation of the nematic phase without activity

In the presence of ATP, motor proteins walk on the microtubules and push them for gliding. They are active crosslinkers in the active nematic phase. When the network is wholly depleted of ATP, motor proteins remain attached to the microtubules but now function as a passive crosslinker. The switch from active to passive crosslinker causes the bundles to contract. After a few hours, up to 2 days, the network morphology changes due to bundle contraction in figure 4.10; gaps between defects and microtubule bundles are shown to increase in size, and the structure has more voids.

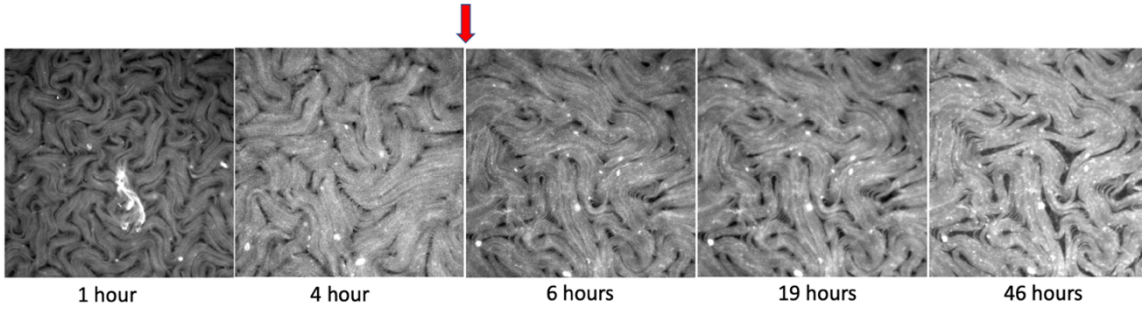

Figure 4.10: An overview of extended imaging of a microtubule-based nematic network. In the first four hours after adding the ATP system was active, the gaps became more extensive after the network became immobile, and bundles were more contracted. The red arrow indicates the time that system became inactive.

The images can be binarized using software such as ImageJ to quantify the microtubule contraction and increase the size of the gaps and voids in the post-activity phase. Binarization involves converting the grayscale image into a black-and-white binary image with either black or white pixels.
The histogram function in ImageJ can quantify the changes in the binary image. The histogram displays the distribution of pixel intensities in the image. By analyzing the histogram, we can determine the number of dark (black) pixels versus the total number of pixels in the field of view. This information can quantify the changes in the size and distribution of gaps and voids in the post-activity phase.
By comparing the histograms of the images, we can observe the changes in the number and distribution of dark pixels, which correspond to the gaps and voids. Figure 4.11 shows the increasing ratio of the dark pixels over the total number of pixels versus time.

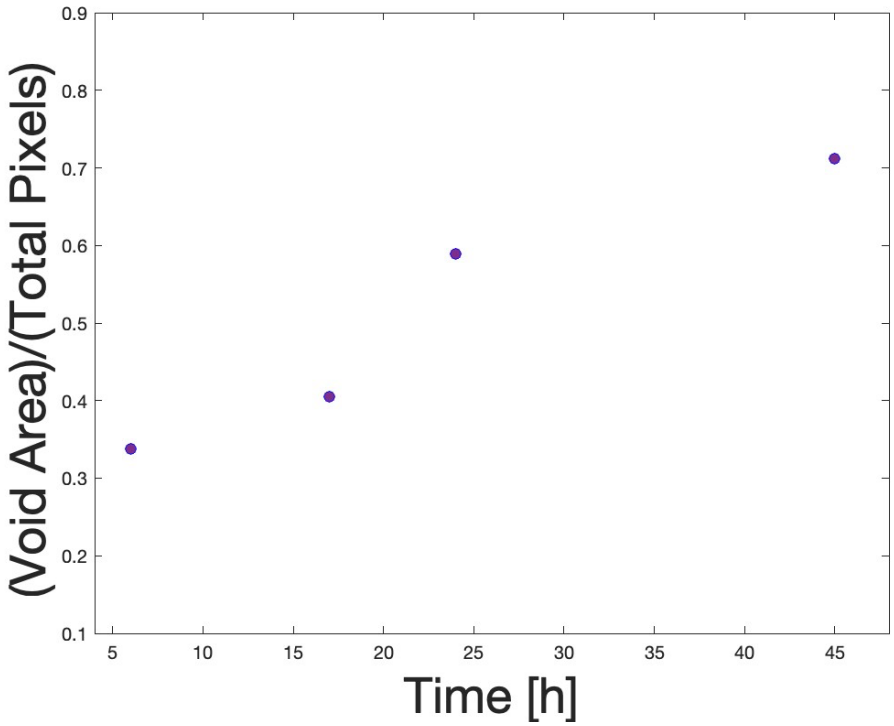

Figure 4.11: Ratio of dark pixels or voids versus time in binarized images.

Change in morphology due to frictional damping

In a typical experimental setup, the active nematic quasi-2D structure is confined at an oil/water interface. The oil viscosity can alter the active length scale but not disrupt the active nematic phase. I varied the oil viscosity to find the proper oil viscosity based on the active length scale for my future experiments. As Pau Guillamat et al.[85] previously demonstrated the active length scale and the oil

viscosity relation in a similar setup, I expected to observe an active length change in the active nematic phase. For this experiment, I used five different oil viscosities, previously measured by Dr. Amanda Tan using a Stresstech HR rheometer.[51] In figure 4.12, the viscosities from left to right, respectively, are 382.2 (±6.4) mPa s, 554.2 (±9.1) mPa s, 685.6 (±11.7) mPa s, 939.4 (±16.4) mPa s, and 1144 (±19.2) mPa s. From this data, I observed that the number of defects from left to right increases, which means the active length scale decreases, and this is consistent with the published work from Pau Guillamat et al.[85] However, they experimented with a broader range of oil viscosities, and the difference between each experiment is more distinct.

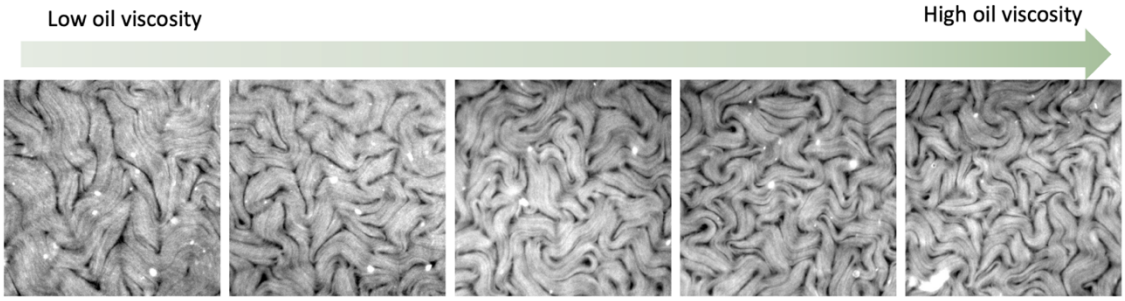

Figure 4.12: Defect density changes as the oil viscosity on top of the active nematic layer change. The higher oil viscosity causes more frictional damping, and the defects are denser.

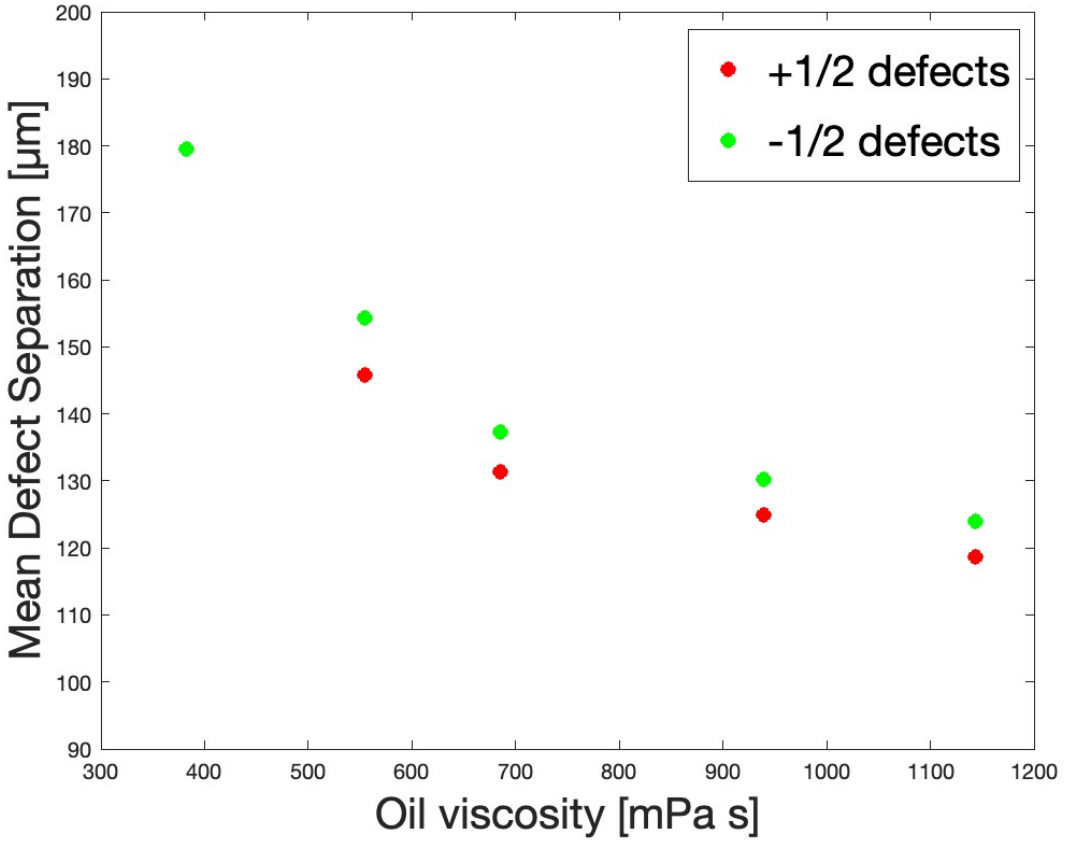

Figure 4.13: Mean defect separation versus oil viscosity demonstrating mean defect separation decreases when oil viscosity increases for both +1/2 and -1/2 defects.

The same method has been used to measure the mean defect separation by counting semi-integer defects for different oil viscosities. In figure 4.13, the mean defect separation between defects decreases as oil viscosity increases.

Conclusion

In this chapter, we measured active length in active nematic as a function of ATP concentration and oil viscosity. The active length scale increased as the fuel source, or ATP, was depleted. The active length scale changes when the ATP or fuel is consumed, and to keep the balance between elastic stress and active stress, the active length scale increases until the network stops. After the structure does not have sufficient ATP to remain active, the motor proteins no longer exert force on microtubules. Still, they can stay connected and act as a passive crosslinker, and this causes a contraction in microtubule bundles. Due to this transition from active to passive crosslinkers, the nematic phase becomes more contracted, and more voids appear. I also varied the oil viscosity in the experimental setup because published works exhibit active length changes with

different oil viscosity. I confirmed with our setup and oils that we have available in the laboratory we observed the same results. The oils I used viscosity were slightly different, and the mean defect separation was noticeably different and decreased as I increased the oil viscosity.

Acknowledgment

I want to acknowledge my former lab mate, Dr. Amanda Tan, for training me on this project. Also, she measured the viscosity of five different oils that we used. I want to acknowledge our funding resources from NSF DMR-1808926. NSF-CREST also supported the project: Center for Cellular and Biomolecular Machines at the University of California, Merced (HRD-1547848). Finally, we acknowledge the Brandeis Biomaterials Facility Materials Research Science and Engineering Center DMR-2011846 for some of the materials used in this work. I also acknowledge BioRender, I made schematic figures of this chapter using BioRender.

Chapter 5

Confining Microtubule-based active nematic in microfluidics

Introduction

Active Nematics follow non-equilibrium physics, and their behavior is not predictable with equilibrium physics such as classical thermodynamics. With strong collective motion, the microtubule-based active nematic is chaotic, and its complex structure can be studied with hydrodynamic theory.[3], [11], [63], [89] These structures are fascinating when micro-scale microtubules move collectively and show macroscale structures, but their dynamics still need to be fully understood. There are different ways to control the dynamics of microtubule-based active nematic and their collective motion, for instance, changing the characteristics of microtubules and varying their fuel source or the depletion force between microtubules. Another parameter that can be varied is the surrounding of the active matter, such as lateral confinement.
For this purpose, this chapter discusses the challenges of confining active nematic inside microscale geometries and proposes a simple and robust experimental setup.

Background

Self-organizing and self-mixing microtubules are confined in 2D between the water-oil interface. Semi-integer defects are constantly annihilating and creating in the nematic phase, and they are chaotic or, as described by Amin Doostmohammadi et al.[62], active turbulence state. Tan et al. studied mixing and braiding in this chaotic system. If mixing two fluids or dyes is imagined, the +1/2 defects act similarly to the mixing rod in mixing two fluids. They investigated the active turbulence and the mixing quality in microtubule-based active nematic in bulk. Naturally, this question arises, how does the quality of mixing or the dynamics of microtubules changes as we confine the structure? Shendruk et al.[63] in 2019, theoretically investigated microtubule-based active nematic in thin channels.

Based on their simulation and theoretical model, dancing defects or swapping defects are predicted. In the same year, Hardoüin et al.[90] experimentally demonstrated the periodic motion of defects in a thin channel. There are previously published studies on other geometries, like Microtubule-based active nematic inside a vesicle[65] microtubules confined inside spherical confinements[54] and inside torus shape geometries.[66] Recently Hardoüin et al.[91] published about the active boundary layer in microtubule-based active nematic, discussing the role of confinement in defect dynamics theoretically and experimentally. In their work, the active boundary layered is defined for the first time. It represents the anchoring of the microtubule bundles on the wall and topologically polarizes the confining wall.
Every confinement that has been experimentally investigated before, it has been challenging. In this chapter, a robust experimental method will be discussed that would be suitable for various geometries. In developing this method, the priority was a high experimental success rate and simplicity. In the upcoming chapter, the dynamics of defects under strong confinement are discussed in detail.

Experimental details

The experiment is designed to confine the active network on a micro-patterned polydimethylsiloxane (PDMS) device. For example, we could confine microtubule based active nematic in a range of ellipses, channels, and circular wells.

Active MIX

Active MIX and its detailed component have been discussed in chapter 4. The active MIX comprises fluorescent tagged GMPCPP polymerized microtubules with an approximate length of 2μm. Also, consist of biotinylated kinesin or K401-bio mixed with streptavidin to make kinesin clusters. Polyethylene glycol or PEG to induce microtubule bundling and PK/LDH for ATP regeneration. We also made an antifade solution from Glucose, Glucose Oxidase, Catalase, and DTT to prevent photobleaching during imaging. We added ATP before the experiment to activate the MIX and make the active network.

PDMS microfluidic device

Confinements were designed in the CAD software “Autodesk Fusion 360” Using the “Phrozen Sonic mini” 3D printer and Aqua 8k resin, the master mold was 3D printed.

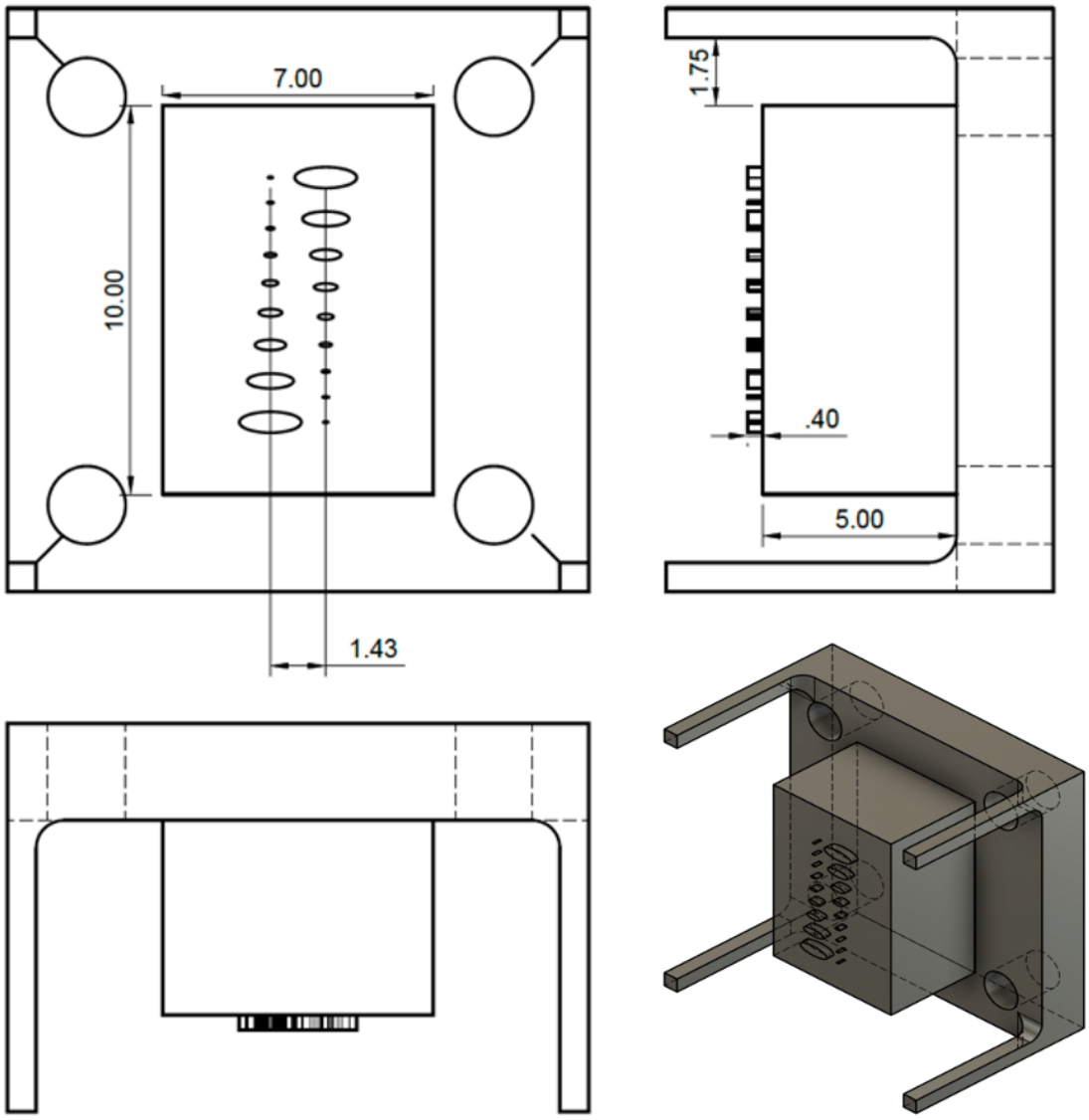

Figure 5.1: CAD design for a master mold with ellipse-shaped pillars on the surface.

Depending on the geometry and details, the cleaning method after 3D printing can be adjusted. I used isopropyl alcohol (IPA) to rinse immediately after the print, followed by IPA spray to clean the features precisely, and 20 min in a stirring cleaning station filled with IPA. Excessive cleaning will damage the master mold and decrease the pillars' height. I used a profilometer (Bruker Dektak XT) to check the pillars' size and uniformity. (Figure 5.2) With the described cleaning method, the height of the pillars was measured to be 20 μm less than the original 3D design.

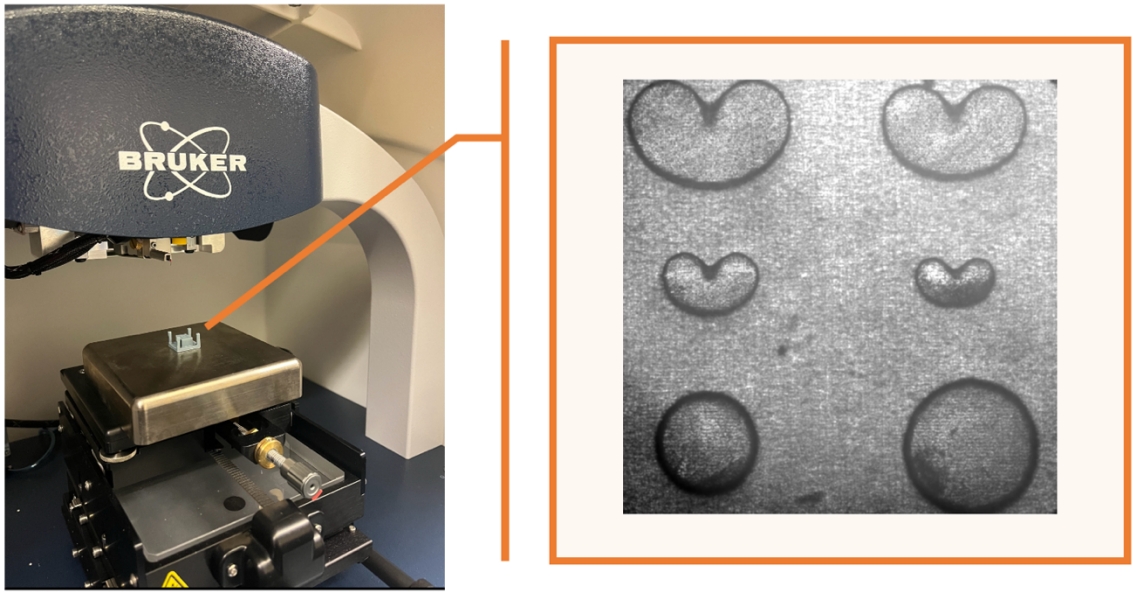

Figure 5.2: Profilometry of pillars to measure their height and sharpness of the edges after cleaning and before PDMS deposition.

After cleaning the master mold with pillars in different geometries, it is cured with UV for 45 min and thermally for 2 hours at 120 C to minimize monomer release when working as the master mold.[92]
A layer of Polydimethylsiloxane (PDMS), (a mix of 184 Silicone elastomer base, and 184 Silicone elastomer curing agent in a 10:1 ratio) is added to on top of the master mold in an appropriate container and degassed for 1 hour under a desiccator to remove bubbles. Then, the clear PDMS mix on top of the mold is cured in the oven at 60 C for at least 4 hours. From 3D printed pillars, microfluidic wells with desired geometry have been prepared. (Figure 5.3)

Figure 5.3: On the left is an example of the 3D printed master mold with a grey resin; on the right is a clear PDMS microfluidic device with wells on the substrate.

The PDMS device is coated with a polyacrylamide polymer brush to make it hydrophilic and prevent proteins from sticking to the PDMS. PDMS wells can be kept in the acrylamide solution for up to four weeks, but I made fresh-coated PDMS wells biweekly to have a uniform acrylamide coating.
Before the experiment, PDMS-coated devices must be rinsed thoroughly three times with deionized water and dried with pressurized nitrogen gas. To increase the hydrophilicity of the PDMS device, I used plasma cleaner after drying it with pressurized nitrogen. The plasma cleaner that I used was Harrick Plasma PDC-001-HP at low power for 1 min.
Figure 5.4 shows the contact angle of the water droplet on an acrylamide-coated PDMS before and after plasma cleaning. Before, plasma cleaning was slightly more hydrophilic than PDMS without coating, but plasma cleaning increased the hydrophilicity significantly, and water spread on the PDMS uniformly.

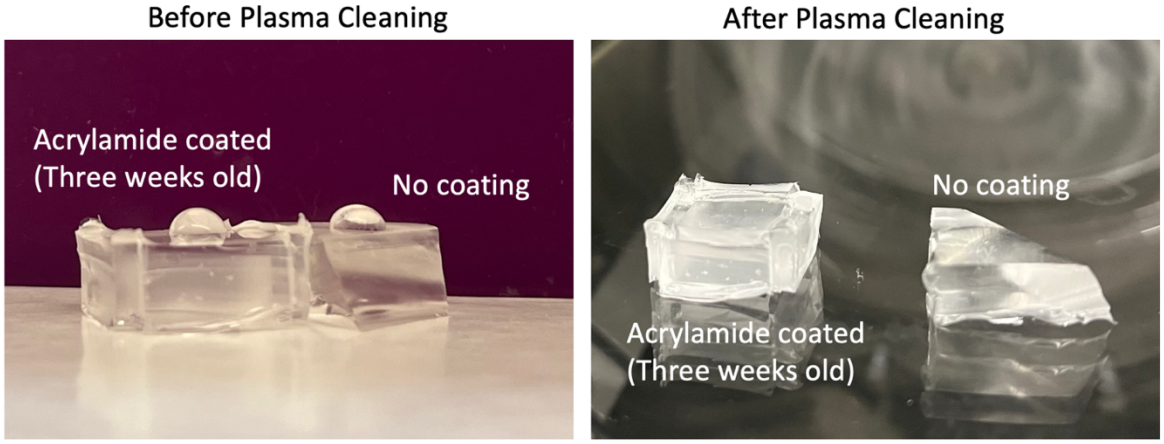

Figure 5.4: Prior to the plasma cleaning, the water droplets create a larger contact angle on both PDMS pieces, and after plasma cleaning, water droplets spread on the PDMS uniformly in both PDMS without coating and coated PDMS with acrylamide which indicates hydrophilicity of the PDMS after plasma cleaning.

To confine the active material inside the wells, the active network should be injected into the wells and then immediately covered by approximately 2mm silicone oil (100-1000 cSt) to build a confined 2D network. The experimental setup is shown schematically in figure 5.5.

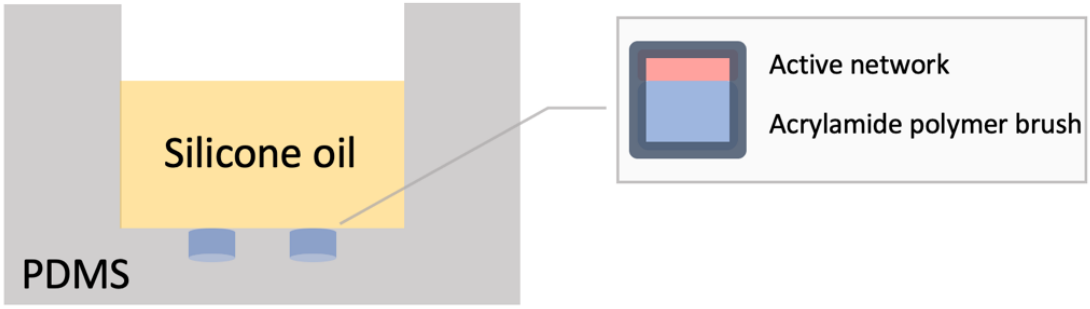

Figure 5.5: Schematic side view of the experimental setup and coating.

In figure 5.6 an example of a confined microtubule-based active nematic in a circular well has been shown. Depending on the precision of the 3D printer, and the cleaning protocol, active nematic can be confined in challenging geometries with sharp corners and cusps with a high success rate and relatively in a short time.

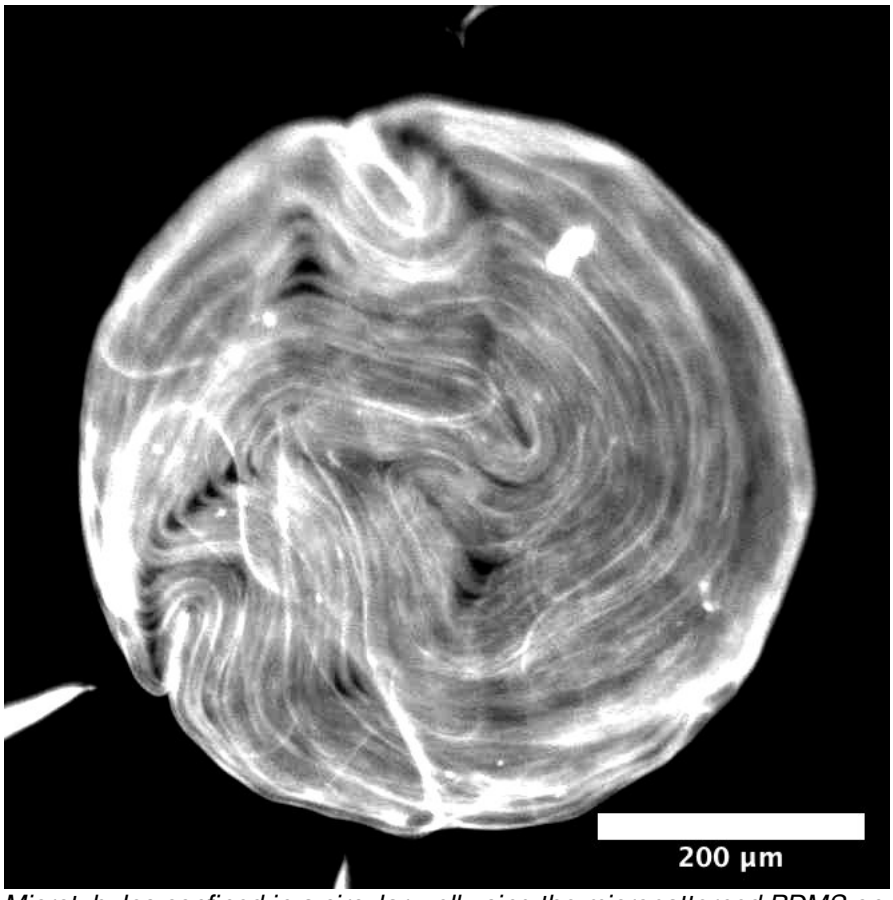

Figure 5.6: Microtubules confined in a circular well using the micropatterned PDMS on the substrate.

Activity can affect the network formation, at higher ATP concentrations, the network forms faster, and at lower ATP concentrations, it might take 1 hour for the network to create an active nematic structure.[3], [8], [11]
For imaging, we use fluorescent microscopy and GMPCPP microtubules labeled with rhodamine or Alexa Fluor 647.
In my setup, the depth of the wells is 80-120μm; in some cases, depending on the geometry and depth of the well, multi-layer active nematic has been observed, and it is challenging to do imaging when there are layers of bright active nematic. (Figure 5.7) In this case, the use of a bucket centrifuge is applicable. We used a bucket centrifuge at 212 x g for 15 min at room temperature to enhance the 2D network.

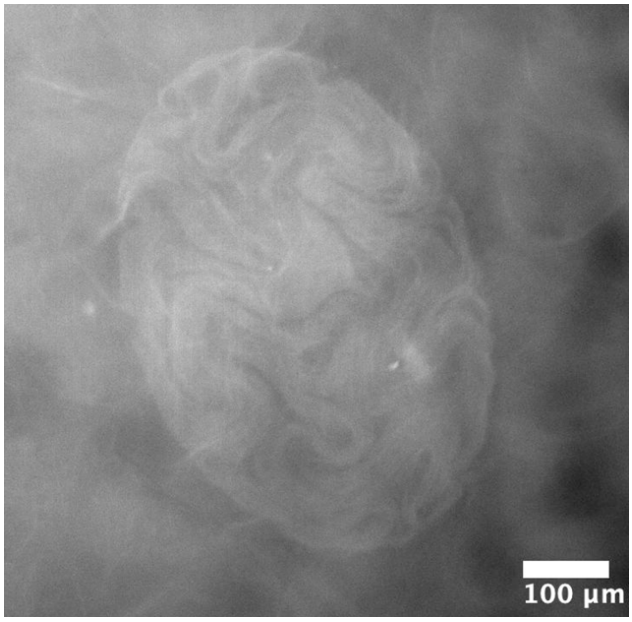

Figure 5.7: Multilayer active nematic structure. Microtubule-based active nematic is confined inside the ellipse well, but also, there are multilayers of active nematic on the surface, making the imaging harder.

This method has been published in JoVE journal [93], and after the preparation of the desired design, it is robust and has a high success rate in confining aqueous active structures. The full schematic of the protocol is shown in figure 5.8.

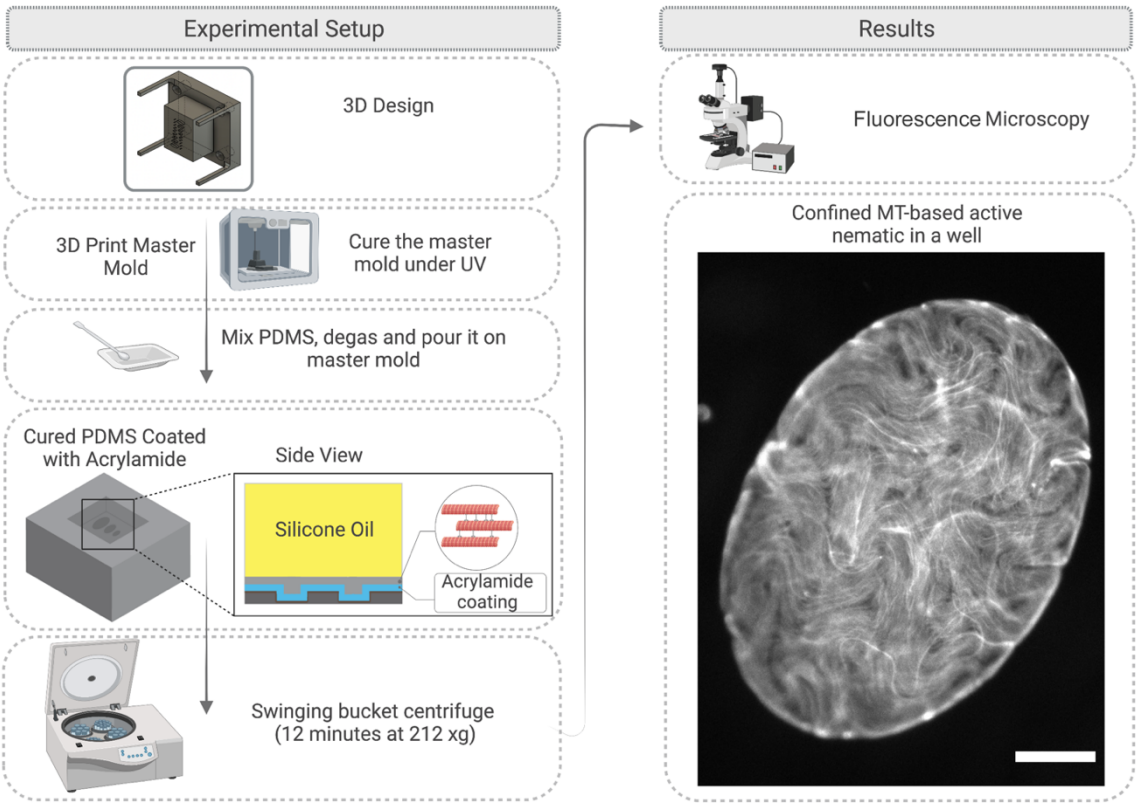

Figure 5.8: Schematic view of the protocol for confining microtubule-based active nematic inside an ellipse-shaped well. Scale bar 200μm

I also used different methods that worked, but the success rate needed to be higher and more complicated. Here I will briefly discuss other methods and some tips regarding achieving the best confinement in the simplest way.

Alternative methods

Initially, I was inspired by P. Guillamat [85] to confine microtubule-based active nematic between a water-oil interface in an open-face PDMS well. In that published method, the substrate was plain glass coated with acrylamide. I prepared a photomask of our desired designs; after photolithography with SU8, a negative photoresist, and a mask aligner, I prepared pillars in different geometries. In photolithography with SU8, it could be challenging to make stable pillars higher than 50μm. After preparing the pillars, I used PDMS deposition to create wells with desired geometry. When PDMS was cured, I peeled it off, and I used plasma cleaner to attach the PDMS to a glass slide. Eventually, I stuck the PDMS well on top of the PDMS wells. Because it was two separate pieces of PDMS on top of each other, achieving a good adhesion even with UV glue was challenging, and I decided to make one piece mold using the 3D printer.

For PDMS coating, I started using polyvinyl alcohol or PVA to make it more hydrophilic and prevent protein absorption, but with PVA, I was making multilayer coating, and the PVA would fill the well, and active nematic was forming on top of the well, and not inside of the well. (Figure 5.9)

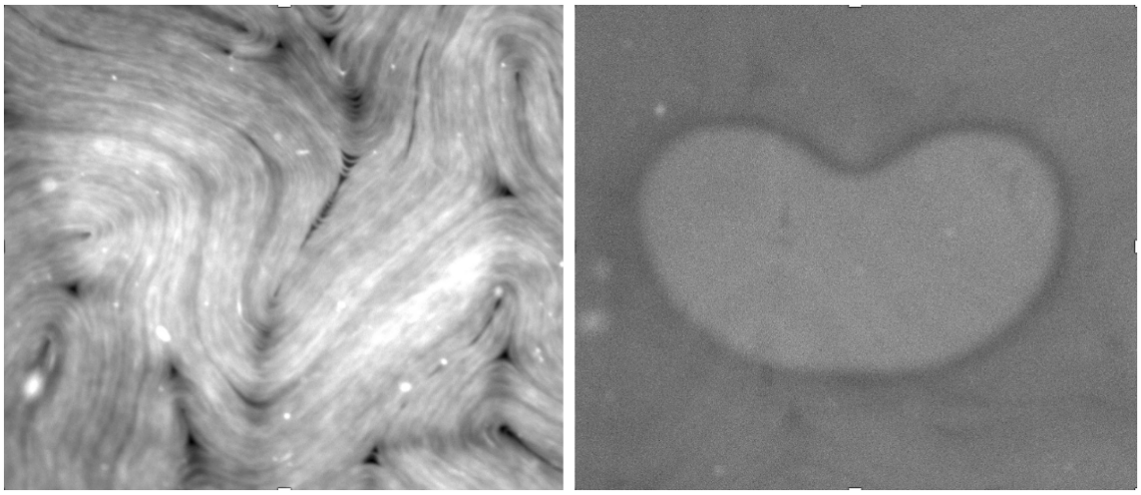

Figure 5.9: Cardioid geometry is coated with PVA and filled the well. The active network is formed only on top of the cardioid and is not confined inside the well. This could happen with not drying the well properly as well.

Experimentally, I obtained the best uniform and thin coating layer with an acrylamide polymer brush. I also tried the Nanoscribe ultra-precise 3D printer at Caltech's Kavli Nanoscience Institute (KNI) facilities. The precision is excellent, but microscale geometries are time-consuming, and the result and experimental setup would be more like the photolithography method.

Another factor that plays a role in active nematic confinement is the proper active length and well-size ratio. The ratio needs to be adjusted, and you want to see the minimum number of defects in the well. If the geometry is too small compared to the active length, materials tend to stay on top of the well and cannot be confined inside.

For better confinement and to prevent material exchange between different wells, I kept the wells at least 200μm separated. In cases where they were closer, there is a higher chance of material exchanges between them, and it is more difficult to achieve an entirely confined network within a well. In figure 5.10, there is an example of spacing between wells.

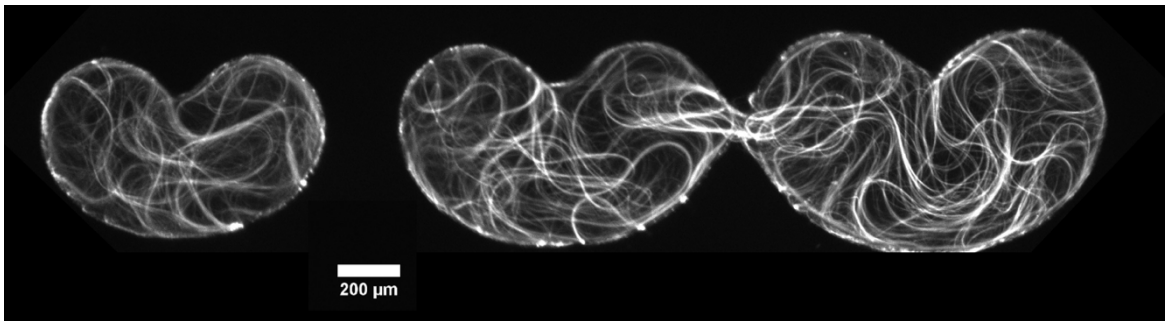

Figure 5.10: Microtubules confined in cardioid-shaped wells with different spacing between the wells. When wells are close to each other, there is a material exchange between the wells, and the material is not fully confined within one geometry. At least 200µm space between wells is recommended.

Another factor that plays a role in better confinement and its imaging is the thickness of the oil. In an imaging system from the top of the microfluidic device, the working distance of the objective matters, and I used 5x and 10x objectives with 14mm and 12mm working distances to be able to image from the top of the oil layer. As we increased the oil thickness, the quality of the images decreased. Also, if the oil layer is not thick enough, the structure will likely stay in 3D instead of 2D and quasi-2D. For our confined system, we found the optimum oil thickness of about 2 mm or 100μL. (Figure 5.11)

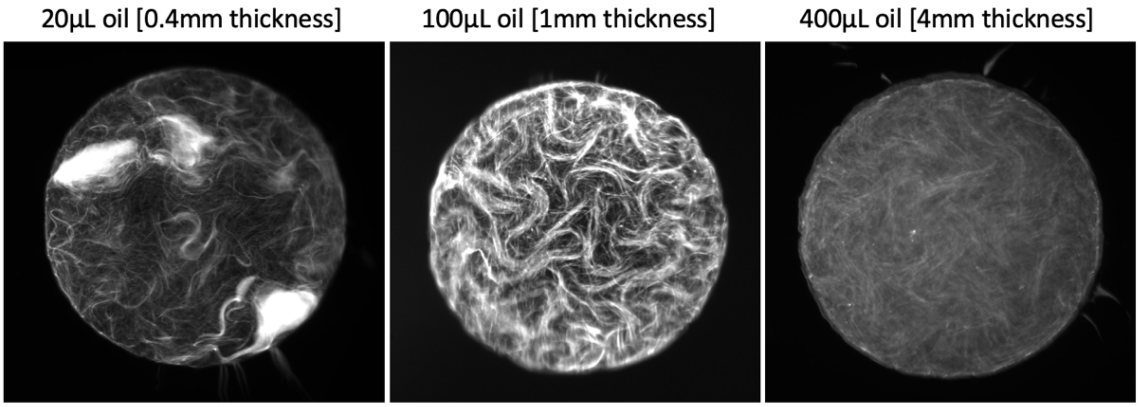

Figure 5.11: Microtubule-based active matter with different oil thicknesses. From left to right, the thickness and volume of the oil increased. With 20µL oil, the oil is not sufficient to confine the material in 2D. 100µL oil is our ideal range, equivalent to 2mm thickness. The 2D network is enhanced at higher oil thickness, but the imaging gets harder, and the network looks blurry. The radius of the confinement is 350 µm.

Conclusion

This chapter introduces a new robust method for confining microtubule-based active nematic inside different macroscale geometries. We are making a biopolymer-based active structure made of microtubules and motor proteins. We confine them in 2D and enhance their collective behavior to observe active nematic structures with active topological defects. I demonstrated an efficient experimental setup to study this system in different geometries and confine them laterally. Based on prior theoretical studies and experiments, we know that geometrical confinement can influence the dynamics of the active nematic network. The experimental method and some alternative methods have been described in detail. This method applies to other aqueous active systems. This master mold design can be used for different geometries and geometries with non-trivial total topological charges. Eventually, geometrical confinement can help us better understand the dynamics of the active nematic structure and control the defects' motion. Controlling their dynamics will be a significant steppingstone for designing microbots[94] and drug delivery systems.

Acknowledgments

I thank all the authors of the “Forming, confining, and observing microtubule-based active nematics” published in 2023 at JOVE. Also, Dr. Jordi Ignes for his valuable advice on the experimental setup, and Dr. Bin Liu and Salvador Diaz for assistance in 3D printing the mold. We acknowledge generous funding from the NSF DMR-1808926. NSF-CREST also supported the project: Center for Cellular and Biomolecular Machines at the University of California, Merced (HRD-1547848). We acknowledge the Brandeis Biomaterials Facility Materials Research Science and Engineering Center DMR-2011846 for some of the materials used in this work. Also, I acknowledge Kavli Nanoscience Institute for the training on ultraprecise Nanoscribe and photolithography.

Chapter 6

Active turbulence to periodic motion in microtubule-based active nematic

Introduction

Microtubule-based active nematic exhibit active turbulence or chaotic dynamics, one of these systems' main characteristics. Active turbulence is different from traditional turbulence. Turbulence is a state of fluid motion characterized by chaotic, irregular fluctuations in velocity, pressure, and other fluid properties.[3], [11], [62]

Active turbulence is a type of turbulence that arises in systems where the constituent particles are self-propelled and generate their own motion. Examples of active particles include bacteria[9], algae, and synthetic microswimmers.[3] In active turbulence, the interplay between the self-propulsion of the particles and the fluid-mediated interactions between them can lead to the formation of complex flow patterns that exhibit similarities to traditional turbulent flows.[51]

One of the key differences between active turbulence and traditional turbulence is the energy source driving the flow. In conventional turbulence, the energy input comes from external sources, such as a pump or a wind field, which creates an imbalance in the flow and drives the formation of vortices. In contrast, in active turbulence, the energy input comes from the self-propulsion of the particles, which can generate their own flow and creates vortices. Another important characteristic that they exhibit is self-mixing behavior.[11] In general, mixing is an important phenomenon that happens everywhere around us, and in the industries such as the chemical industry, polymer industry, construction industry, and food and beverage is crucial because of efficiency. In the food industry, imagine mixing food coloring in a taffy. Taffy pullers efficiently mix the dye by pulling and stretching the taffy with a set of large hooks in a specific order.[60] (Figure 6.1)

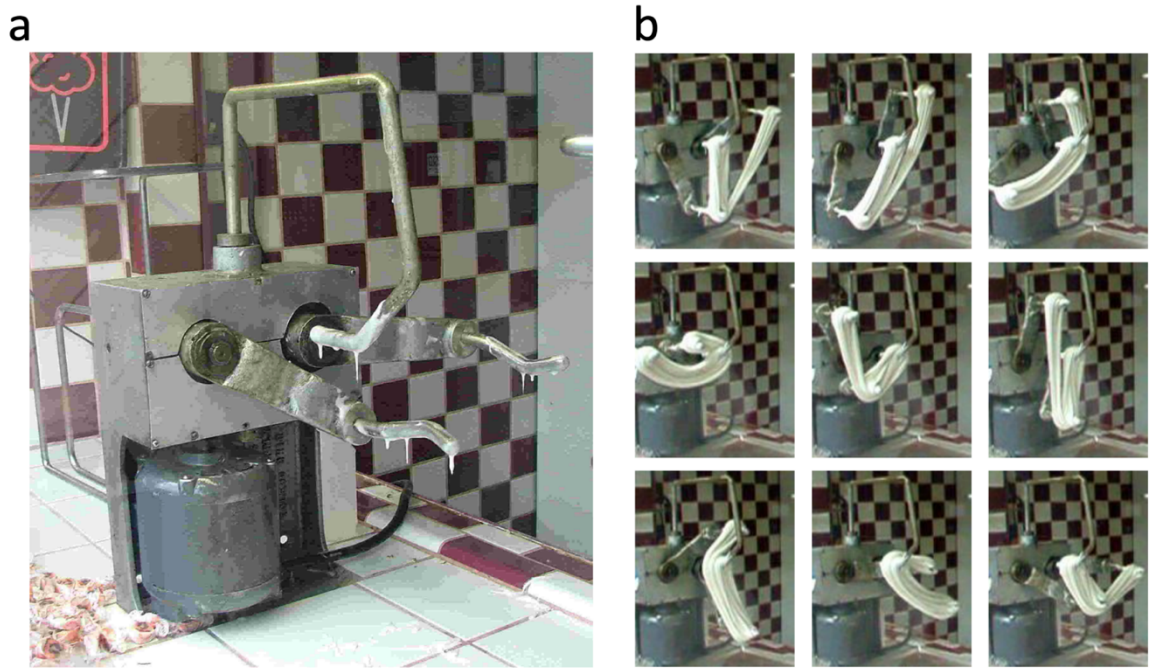

Figure 6.1: a) Taffy-pulling machine b) The complete process of pulling and stretching taffy in snapshots. The image is taken from "Topological Optimization of Rod-Stirring Devices" by Matthew D. Finn and Jean-Luc Thiffeault at SIAM Review (2011).[60]

Mixing in fluid dynamics can be investigated to better understand geophysical flows in the atmosphere and the ocean.[60], [95], [96] Mixing can be quantified in different ways depending on the context and application; one of the approaches is to measure how well a particular fluid mixing has homogenized the fluid. It is defined as the ratio of the variance of the dye concentration or tracer after mixing with the initial fluid.

As discussed in chapter 4, the structure of microtubule-based active nematic is like an ordered fluid. This active nematic is a self-mixing network with imaginary rods. These imaginary mixing rods swap their positions and mix or stretch microtubule bundles. The minimum stretching rate of the microtubule bundles is the concept of topological entropy, and with topological entropy, the quality of mixing in this system can be measured. Topological entropy can generally be either positive or zero, but it cannot be negative. The value of topological entropy is related to the rate at which material lines in a flow are stretched and folded. The topological entropy is zero if the flow is such that the material lines are not exponentially stretched or folded.

On the other hand, if the stretching and folding of material lines in a flow are exponential, then the topological entropy is positive.[11], [51], [60], [97] The dynamics of mixing in active nematics can be complex and depend on many factors, such as the particles' density and activity, the system's geometry, and the strength of any external fields or confinement. The quality of mixing in microtubule-

based active nematic has been investigated by Tan et al. (2019).[11], [51] In Tan's work, the analogy is postulated that +1/2 or comet-shaped defects act like stirring rods in fluid mixing experiments. The mixing behavior is similar to braiding patterns.

Theoretically, we expect specific braiding patterns in confined structures with efficient mixing. Shendruk et al.[63] investigated confined channels. In a confined but wide channel, there is active turbulence, but as the width of the channel changes, the narrower it gets, it becomes more affected by the channel, and it exhibits dancing disclination. They simulate defects' Ceilidh dance, a Scottish dance in which partners or defects swap their positions repeatedly. Figure 6.2 shows the simulation of defect patterns in a narrow channel. In this simulation, -1/2 defects are shown with magenta color and residing closer to the channel walls, and +1/2 defects are shown with green color dots and closer to the center of the channel.[63]

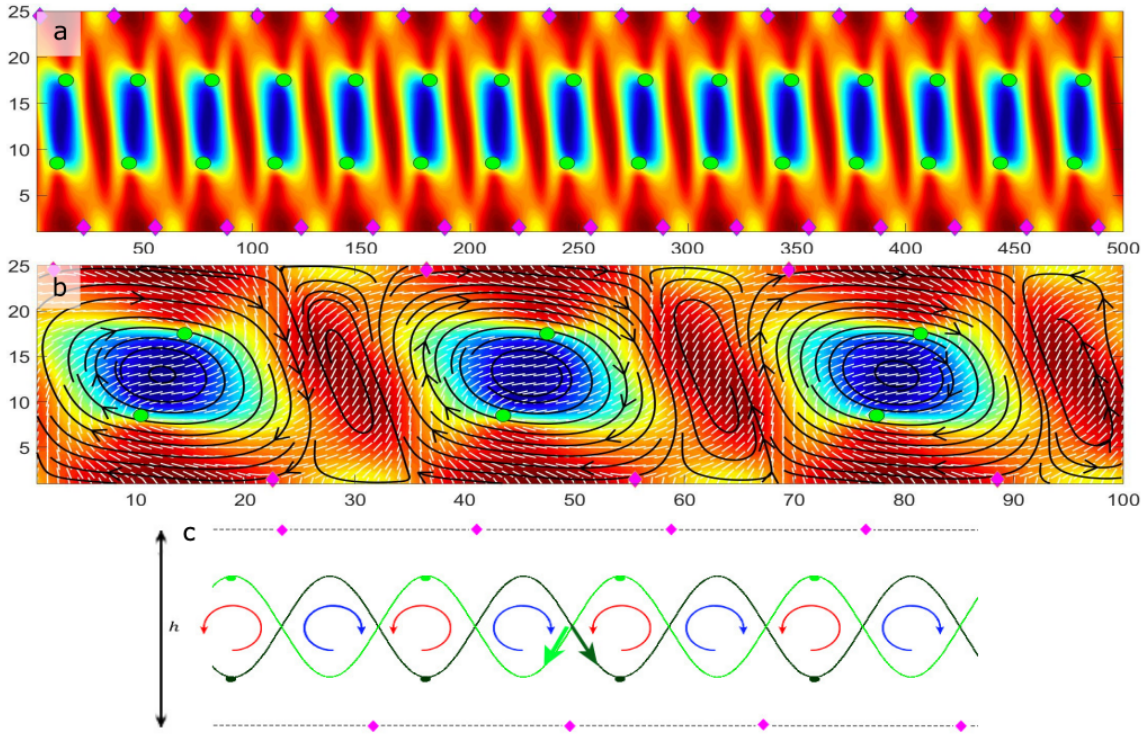

Figure 6.2: Dancing defects in a narrow channel. a) Demonstration of vorticity field of highly ordered vortex lattices. In this simulation, magenta color diamonds show -1/2 defects at the wall, and the green dots are dancing +1/2 defects in the mid-region. b) Zoom view of director field and streamlines. c) Ideal schematic of defects' Ceilidh dance. The image is taken with permission from "Dancing disclinations in confined active nematics" by Tyler N. Shendruk et al. at Soft Matter (2017).[63]

Hardoüin et al.[90] experimentally confined active nematic in narrow channels and confirmed the theoretical studies. (Figure 6.3)

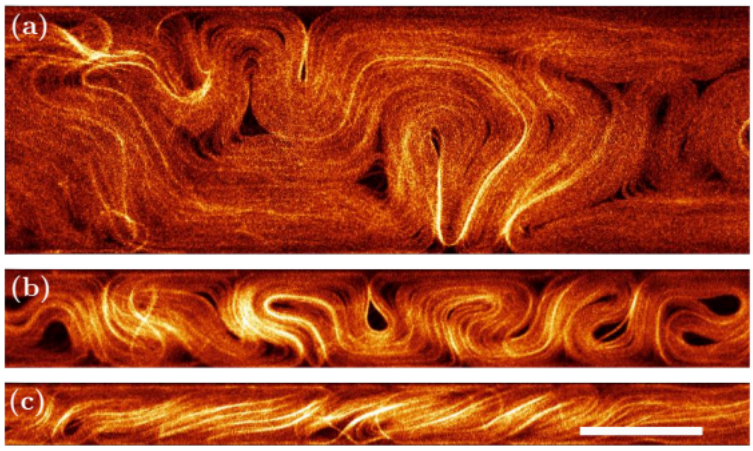

Figure 6.3: Microtubule-based active nematic confined in different sizes of channels. The image is taken with permission from "Reconfigurable flows and defect landscape of confined active nematics" by Hardoüin, J., Hughes, R., Doostmohammadi, A., et al. at Nature Communications Physics (2019)[90]

Dancing defects in channels form a braid known as the "silver braid," which shows a counterclockwise or clockwise interchange of defects. Figure 6.4 shows a schematic for the theoretical understanding of silver mixing. In this figure, similar to microtubules in a narrow channel, +1/2 defects are interchangeably swapped in clockwise and counterclockwise directions.

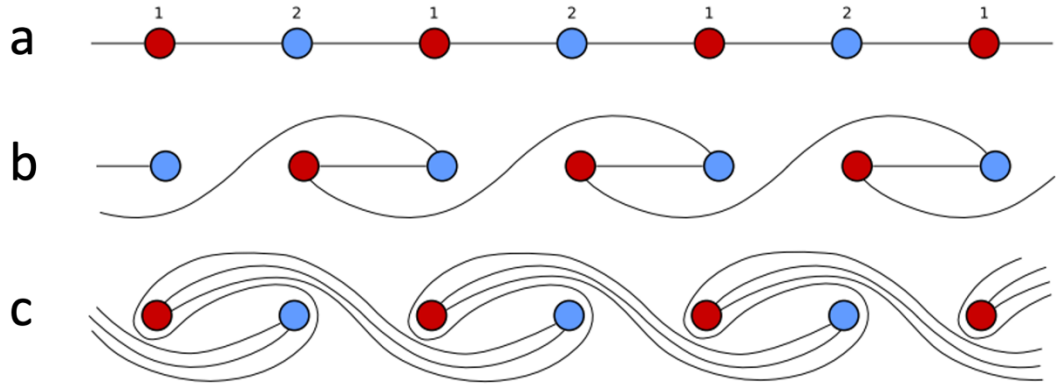

Figure 6.4: a) Stirring rods on a periodic lattice. b) Clockwise interchange of rods at 2 & 1 position. c) Counterclockwise interchange rotation of rods at positions 2 & 1. The image is taken from "Topological Optimization of Rod-Stirring Devices" by Matthew D. Finn and Jean-Luc Thihffeault at SIAM Review (2011).[58]

Different braiding patterns have been used on human hair for as long as 3000 years. Archeologists found a 3,300-year-old woman with braided hair in Egypt. This a significant leap in time, and now we are discussing the orders of biopolymers as closed braids. The traditional three-strand braid, commonly known as the golden braid, has caught our attention. We aim to replicate this braid and study its periodic motion by using active nematic material confined in a cardioid-shaped well. Jean-Luc Thiffeault, in his book, “Braids and Dynamics”,[60] mentioned the three-strand braid. If the rods follow a figure-eight pattern, they make a cardioid shape pattern, and moving rods in a figure-eight pattern accelerates the mixing immediately.[57], [60] (See figure 6.5)

Figure 6.5: Mixing a black dye inside a clear fluid using three rods following a figure-eight pattern made this cardioid shape. The image is taken from “Topology of chaotic mixing patterns” by Jean-Luc Thiffeault at Chaos: An Interdisciplinary Journal of Nonlinear Science (2008). Experiments performed by E. Gouillart and O. Dauchot.[57]

The figure-eight patterns and the golden braid mixing differ from active turbulent behavior. This chapter uses cardioid shape confinement to replicate the golden braid and show the periodic dynamics. The cardioid shape has a topological boundary charge of +3/2 and in 2D active nematic is common to observe +1/2 and -1/2 defects. To achieve the total topological charge of +3/2 with comet-shape defects, we need three +1/2 defects, and as Tan et al.[11] discussed, +1/2 defects act as stirring rods in mixing fluids. For a golden braid pattern also, three mixing rods (virtual) are needed. Eventually, the cardioid shape minimizes the bending energy of microtubules, and it is a favorable design to reproduce the golden braid and periodic motion.

Results

Using the method described in chapter 5, I designed cardioid-shaped pillars on a master mold. The size of the cardioid depends on the active length, and active length can be varied with different parameters such as ATP and oil viscosity. In the

experiment, to achieve the golden braid and its efficient mixing, we need to fit the minimum number of defects in the cardioid, three +1/2 defects with a total topological charge of +3/2.

Depending on all these parameters, I prepared PDMS micropatterned devices with cardioid-shaped wells in different sizes with a depth of approximately 100μm. We were able to identify three different dynamics regimes based on the size of the confinement. Strong confinement with minimum defects, intermediate confinement with defect creations, and weak confinement showed active turbulence similar to bulk-like active nematic. Opathalage et al.[54] published similar results for circular-shaped confinement. The researchers identified four distinct categories of dynamical behavior within the circular confinement. In the largest confinement, the system exhibited bulk-like behavior. In the second largest confinement, which is half the size of the largest, there was only weak dynamical variation due to confinement and a reduced number of defects. The intermediate confinement exhibited a fascinating doubly periodic spiral pattern, with occasional creation of defects from the boundary and the maintenance of a +1 topological charge. Finally, the smallest confinement represents a case of strong confinement. While it is still debated whether it is a +1 defect or merely a void in the middle, confinement highly influences the system's behavior. (Figure 6.6)

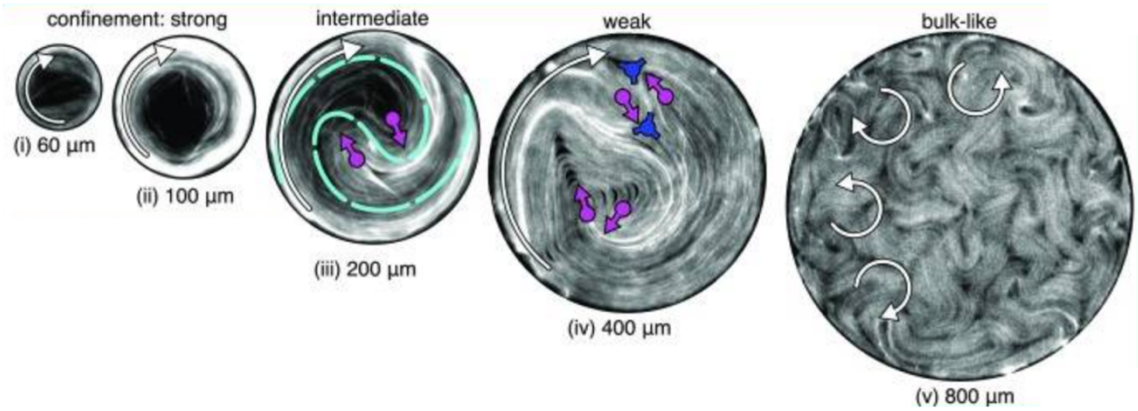

Figure 6.6: Microtubule-based active nematic inside bulk-like, weak, intermediate, and strong circular confinements. The image is taken from "Self-organized dynamics and the transition to turbulence of confined active nematics" by Achini Opathalage et al. at PNAS (2019)[54]

In the following, I will discuss cardioids' weak, intermediate, and strong confinement regimes with a total topological charge of +3/2 and enclosed active nematic.

Weak confinement

Under weak confinement, the effect of the confining geometry on the dynamics of the active nematic phase is minimized. Microtubules at the boundary are affected by the wall and its curvature but not the material in the center. In this chapter, we focused on the big picture and the whole cardioid as a system. As I discussed in chapters 4 and 5, the collective behavior of microtubules is chaotic and unpredictable. Semi-integer defects are constantly created and annihilated everywhere in the cardioid, but theoretically, we expect the total topological charge within the cardioid to remain at +3/2. However, counting the total topological charge is challenging because of the highly dynamic behavior and the constant creation and annihilation of many semi-integer defects. The lifetime of a defect in a highly dynamic and chaotic nematic phase is also short. In figure 6.7, several defects have been tracked manually using the MTrackJ plugin on ImageJ/FIJI.
Every track point is 10s apart, and defects are tracked from creation to annihilation. The defects tracking exhibits their short length, which corresponds to their lifetime. The braiding pattern is not organized, defect creation is happening anywhere in the cardioid, and it is not restricted to the boundary or bulk.

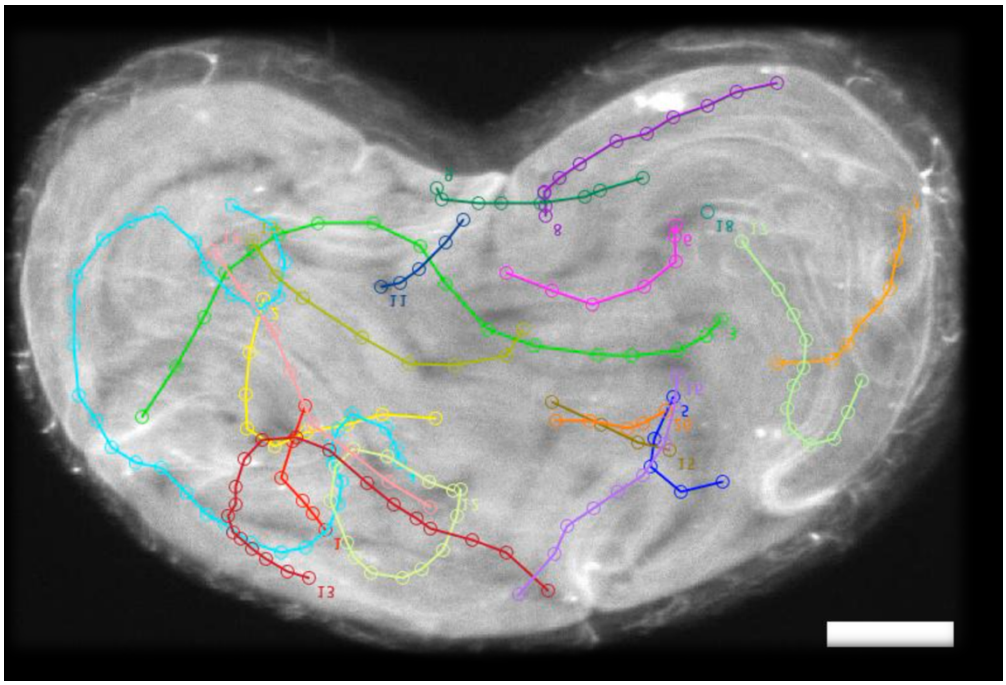

Figure 6.7: Weak cardioid confinement. Bulk behavior of microtubules and defect tracking using the MtrackJ plugin on ImageJ. The time window of the tracked defect is 2 m 20 s. Scale bar 100μm

Intermediate confinement

Under intermediate confinement, defect creation is observed only at the boundary. The total topological charge of the cardioids remained +3/2 throughout the experiment in this regime. At every defect-creation event at the wall, I observed a -1/2 defect which, most of the time, stayed at the boundary but sometimes would join the bulk and eventually annihilate. When the confinement level was intermediate, the trajectories of the defects were somewhat reminiscent of a figure-eight pattern. Still, they did not remain in this shape over time because more defects were present than the minimum number required to form a stable figure-eight pattern. Hardoüin et al.[91] recently published a paper about a population of motile defects near the boundary in confined active nematics and called it the active boundary layer or ABL. ABLs happen in laterally confined active nematics and can feature exclusively -1/2 defects at the boundary. In the intermediate confinement, the defect creation occurs at the boundary, similar to their definition of the active boundary layer. In intermediate confinement, the defect's lifetime is longer compared to weak confinement because there are fewer creation and annihilation events, and it is limited to the boundary.

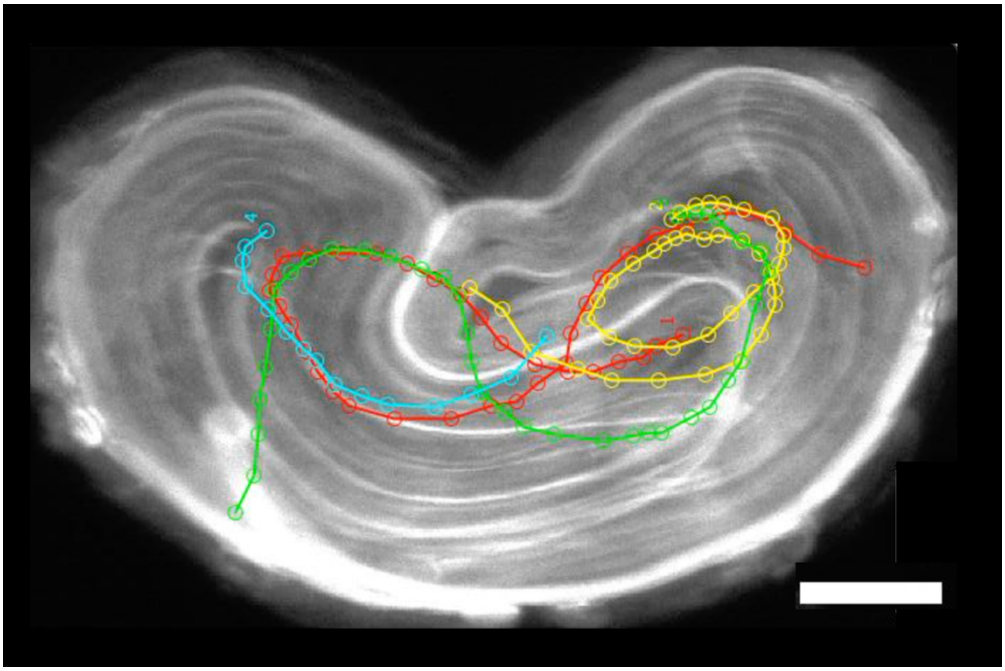

Figure 6.8: intermediate confinement of microtubules with defect creation at the boundary. Defects have been tracked using the MtrackJ plugin on ImageJ, and the time window of the defect tracking is 13 m 20 s. scale bar 100μm

Strong confinement

Under strong confinement, the number of defects is minimized, and we observe only three defects. Three +1/2 defects act similarly to stirring rods in mixing two fluids.[60] As Jean-Luc Thiffeault discussed, mixing two fluids using three rods with a golden braid pattern makes a figure-eight.[60] (Figure 6.9)

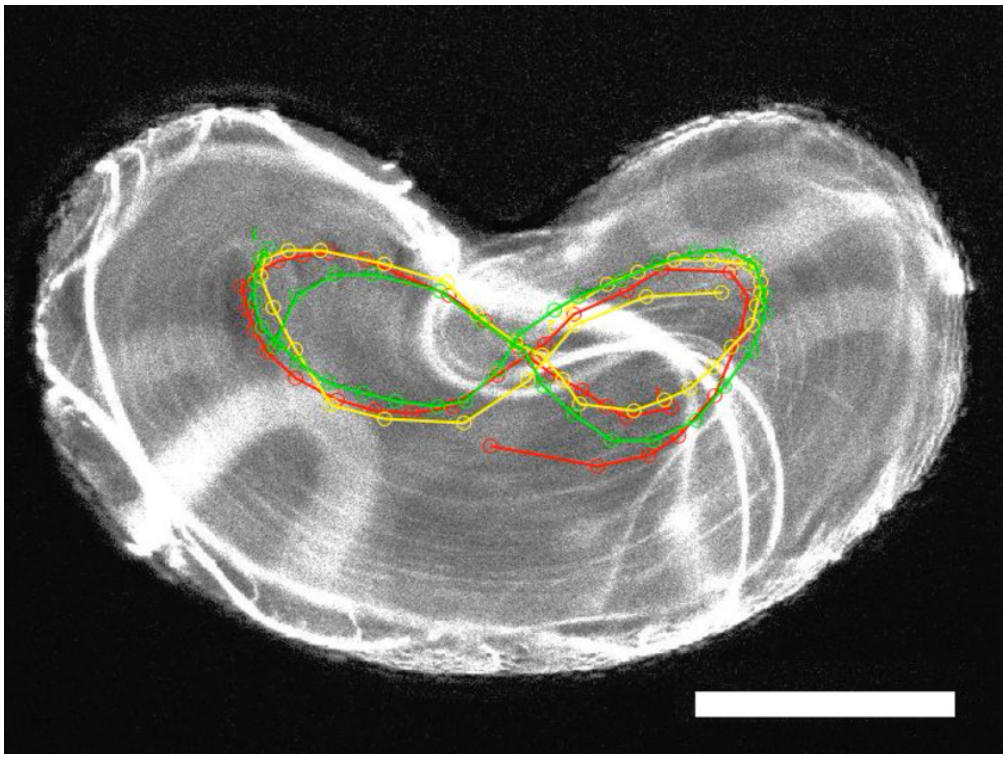

Figure 6.9: Strong confinement of microtubule-based active nematic. Defects are moving in the figure-eight pattern during the experiment. Three defects were tracked manually using the MtrackJ plugin on ImageJ. The time window of the tracked defects is 2 h 13 m 20s. Scale bar 200μm

For the first time, we observed the golden braid pattern in this regime. Microtubule-based active nematic is chaotic, and the self-mixing characteristic is unique. With the golden braid pattern, the mixing is efficient, and the system is not chaotic anymore. As a result, defects should stay longer, and there is no defect annihilation and creation event throughout the mixing. The lifetime of defects is significantly longer than two other regimes, and it is stable until the network runs out of ATP. Three defects were tracked manually over two hours and consistently kept the figure-eight pattern. The figure below presents another example of golden braid snapshots and defects swapping.

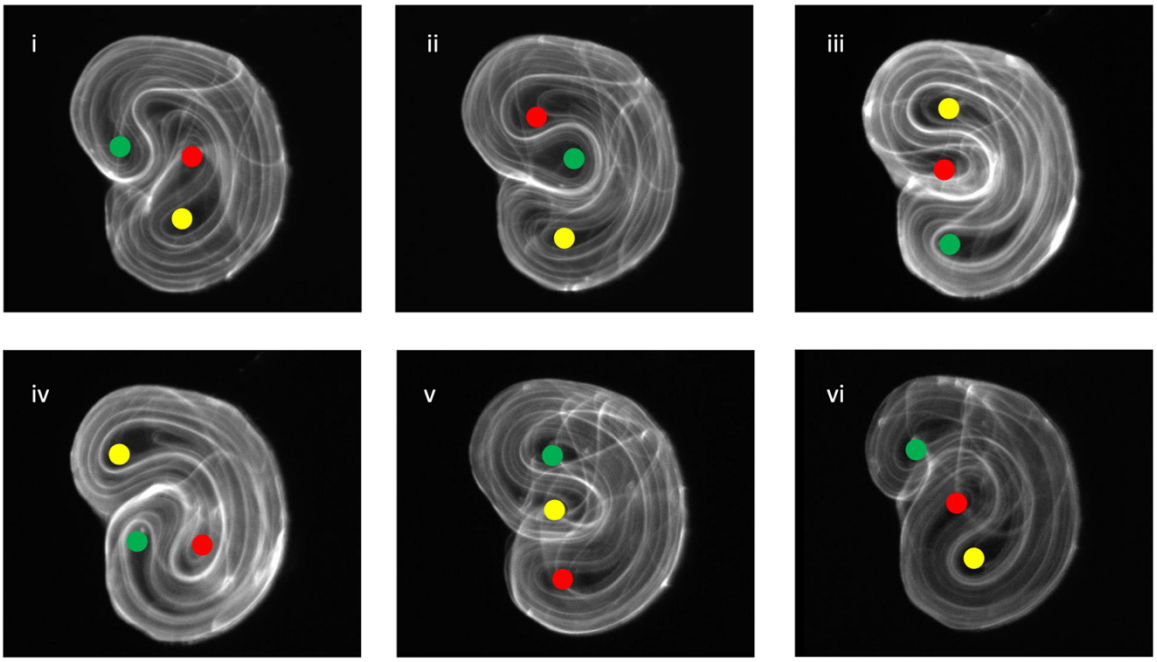

Figure 6.10: Golden braid in microtubule-based active nematic with strong confinement. Semi-integer defects have been demonstrated with green, yellow, and red colors.

Activity and the confinement

I started with the ATP at its saturation level (1000mM) in all the experiments for this chapter. As I discussed in chapter 4, the activity of the microtubules changes during the experiment because even with ATP regenerators that we used in this system still, the network's lifetime is about 5-6 hours. To compare different cardioids' velocities, their imaging should be simultaneously in the same field of view; otherwise, the results would not be precise, and there are more errors in comparison. To address this comparison, I started capturing more than one cardioid in the same field of view. All the parameters are identical for cardioids in the same field of view, such as the active network, the oil, the surface treatment, and imaging. This experimental setup enables us to compare the activity of cardioids solely based on the size of the confining geometry.
After comparing several examples, cardioids with different sizes demonstrated different velocities; however, other parameters were the same. In weak confinement, the confinement didn't suppress the activity significantly. In intermediate confinement, the activity is suppressed but not significant. However, in comparison of strong versus intermediate confinement, we noticed a considerable difference in the activity level.
In figure 6.10, initially, with observation during imaging, we noticed that the activity level is different, and as the confinement is smaller, the activity is more suppressed.

For velocity measurements, I used the Particle Image Velocimetry (PIVLab) tool on MATLAB[77]–[79], extracted the velocity in the x and y directions, and calculated the v_{rms} using those parameters.

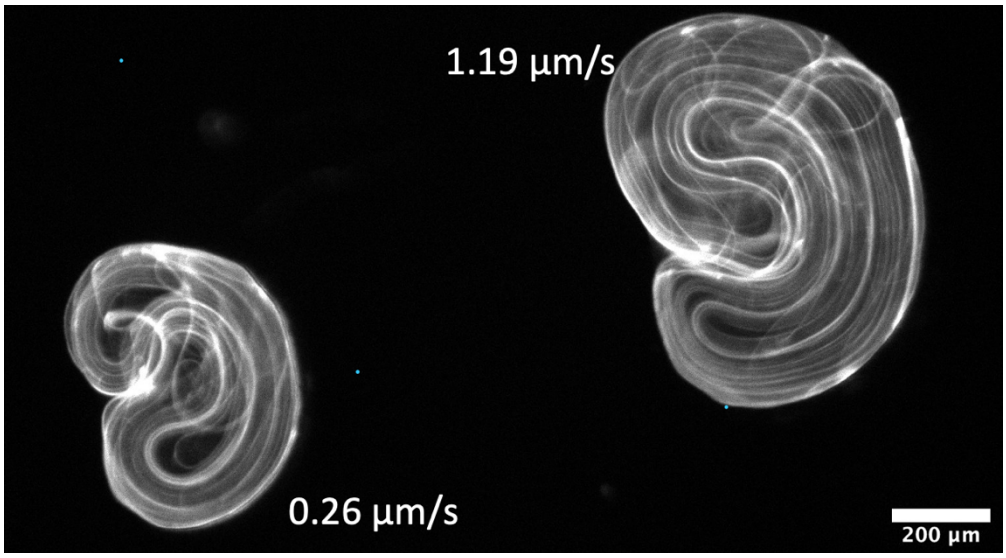

Figure 6.11: On the left, we have strong confinement and a golden braid of defects, and the measured velocity is 0.26µm/s inside the cardioid. On the right, we have intermediate confinement, and the v_{rms} is 1.19µm/s which is about 4.5 times higher than the strong confinement.

Conclusion

In summary, mixing is an important phenomenon we encounter daily. It could be crucial in industry and environmental science to make mixing efficient. Microtubule-based active nematic is a self-mixing system in that the +1/2 defects act as stirring rods in mixing binary fluids. Silver braid mixing happens when we have stirring rods in a lattice, and they swap clockwise and counterclockwise with each other. Silver braid mixing has been observed in narrow channels theoretically and experimentally. Golden braid mixing is an efficient mixing and braid pattern that needs three stirring rods, or the braiding needs three strands. A cardioid shape mold was prepared to study golden braid mixing in microtubule-based active nematic. The total topological charge in a cardioid shape is +3/2, and the minimum number of defects that fit in a cardioid is three comet shapes or +1/2 defects. The curvature of the cardioid minimizes the bending energy of microtubules, and the cusp induces the golden braid pattern and acts similarly to a -1/2 defect.
In this project, we observed three regimes based on the number of defects inside the cardioid. First, weak confinement demonstrated bulk-like behavior; we constantly see defect creation and annihilation, which is chaotic. On the other hand, intermediate confinement showed defect creation only at the boundary, and it maintained the +3/2 total topological charge. The third regime is the strong confinement which, for the first time, we observed the golden braid mixing. In the

strong confinement regime, defects make a figure-eight pattern periodically without any random defect creation and annihilation in bulk or at the wall.
The activity of microtubules is expected to vary as we change the confinement size. Under strong confinement, the movement of microtubules is more restricted, reducing their activity level. As a result, the network would likely move more slowly, and the microtubules would be more limited in their chaotic movement. Conversely, under weaker confinement, microtubules would have more freedom to move and explore their environment, leading to higher activity levels and potentially more chaotic motion. Therefore, the confinement level can significantly impact microtubules' behavior, which should be considered when studying their properties and dynamics in different contexts. In the intermediate and weak confinement, the v_{rms} is higher, but still, the weak confinement suppresses the least between all three regimes.
In conclusion, understanding the mechanisms of mixing in active nematics is important for designing and optimizing these systems for applications such as microfluidics, drug delivery, and sensing.

Acknowledgment

I want to thank all the collaborators of this project, including Prof. Kevin Mitchell, Prof. Linda Hirst, and Md Mainul Hasan Sabbir. Also, Dr. Dustin Kleckner for his advice regarding the post-treatment of cardioid mold and Dr. Bin Liu and Salvador Diaz for assistance in 3D printing the mold. We acknowledge generous funding from the NSF DMR-1808926. NSF-CREST also supported the project: Center for Cellular and Biomolecular Machines at the University of California, Merced (HRD-1547848). Finally, we acknowledge the Brandeis Biomaterials Facility Materials Research Science and Engineering Center DMR-2011846 for some of the materials used in this work.

Conclusion and Future Work

In conclusion, this thesis has contributed to our understanding of active matter systems, which are prevalent in many natural and artificial environments and exhibit intriguing behavior as a non-equilibrium system. This thesis has shed light on their unique properties and dynamics by investigating microtubule-based active nematics in two different setups. Specifically, the first setup involved confining microtubule active matter on the lipid bilayer in 2D, where increasing the microtubule concentration led to the formation of a nematic phase. In the second setup, microtubule bundles were confined in 2D between the water-oil interface and exhibited a nematic phase.

In Chapter 3, we investigated microtubule gliding on a lipid bilayer, inspired by cargo transportation in cells. Our experiments demonstrated the formation of self-organized microtubule lanes that were highly sensitive to microtubule concentration, even without the use of crowding agents. We also observed the redistribution of diffusive motor proteins by microtubule lanes. This chapter provided insights into membrane-bound transportation and the existence of bidirectional microtubule lanes in concentrated systems. Our findings have been published in PNAS as "Active nematic order and dynamic lane formation of microtubules driven by membrane-bound diffusing motors" in 2021.[83]

In chapter 4, I investigated the behavior of microtubules bundled together with kinesin clusters and polyethylene glycol, which create a depletion force. The confined microtubule network forms an active nematic phase between the water-oil interface. I quantitatively analyzed the morphology of the active nematic at different levels of activity and oil viscosity to better understand the characteristics of the microtubule-kinesin-based system. This chapter investigates the effect of internal energy depletion on active nematic texture and dynamics, and the results have been submitted to the international liquid crystal society (ILLC) in a paper titled “Effect of internal energy depletion on active nematic texture and dynamics.”

In chapter 5, I proposed a novel and reliable experimental method to confine the microtubule-based active nematic in various geometries. This fast and easily replicable method allowed for creation of complex geometries and was compared to alternative approaches, including their advantages and limitations. The details of this method have been published in a peer-reviewed scientific video journal titled "Forming, Confining and Observing Microtubule-Based Active Nematics" in 2023. This chapter presents a significant contribution to the field of active matter by enabling the study of active nematics in confined geometries.[93]

Chapter 6 focused on investigating the effect of geometrical confinement on the dynamics of microtubule-based active nematic. The self-mixing nature of the active nematic network was explored, and the mixing efficiency was quantified and improved by confining the material within cardioid-shaped geometries, replicating efficient golden braid mixing patterns. The paper reporting the results of this chapter is currently in progress for submission to a peer-reviewed journal.

The next step is to explore different braiding patterns using various geometries, such as figure-eight geometry. Additionally, the findings from this study of out-of-equilibrium systems could have applications in other fields, such as soft robotics and drug delivery. For example, developing these self-mixing materials holds promise for improving drug delivery and enabling soft robotics to navigate complex environments.

Appendix

A.1 GTP Microtubule Polymerization

1. Combine labeled and unlabeled tubulin with the desired ratio (30% labeled tubulin for microtubule gliding assay)
2. Incubate tubulin (rhodamine and unlabeled) on ice for 10 min
3. Centrifuge in MICRO ULTRA for 10 min at 90,000 rpm to remove dead tubulin
    a. Use a small rotor that's cooled to 4°C
    b. Get 100mM GTP from a -20°C Freezer
4. Save supernatant in a new Eppendorf tube and discard the pellet
5. Add GTP to make 1mM (final) GTP
6. Put Eppendorf tube in incubator for 20 min at 37°C.
7. Add 1mM Taxol (final concentration should be 50uM)
8. Incubate for 20 min at 37°C
9. Centrifuge Eppendorf tube for 10 min at 25C -14,000xg
10. Pipette supernatant out and discard. Resuspend pellet in final concentration -50uM taxol and original volume of PEM100.
11. Incubate microtubules for 1 day to yield the best result

A.2 Microtubule gliding on lipid bilayer

1- Wash glass slides and coverslips in 4 steps (acetone, methanol, ethanol, nano-pure water) in a beaker 1hr in the sonicator
2- Plasma clean for 7 min both coverslip and glass slide (2 min vacuum + 5min plasma clean)
3- Apply spacer to slide ASAP, then drop cast enough nano-pure water to cover the entire flowcell~50ul.
4- Prepare the lipid mixture SUVs (each lipid mixture could be used about 2 weeks)
5- Clean the tip sonicator (wipe it with acetone, methanol and put it in a beaker with 50% ethanol + 50% nano-pure water)
6- Keep the lipid mixture under the tip sonicator at least 5 minute and use an ice bucket to keep the lipid cool. It should look clear and not cloudy.
7- Add 25ul lipid mixture + 2.5 NaCL 2mM + 22.5 ddH2O in an Eppendorf tube and drop it uniformly on the water lock (no contact)
8- Wet a chem wipe and keep it next to the glass slide, put the glass slide with the kimwipe in the oven at 50c for 1h in a petri dish with the lid on.
9- After one hour gently flush slide with 800ul nanopure water, dropcast on one side of flowcell and slowly pull on other side with kimwipe.
10- Exchange the water on the water lock every 15 four times (don't let the water lock dehydrate even for a second)
11- Wipe the glass slide and the excess water (Keep the water lock hydrated and put the cover slip on top and seal the edges – now you have a flow cell)
12- Flow dilute motor proteins (5ul Kinesin + 1 ul DDT 100mM + 46ul PEM80)
13- Wait 5 minutes
14- Flow microtubules (depends on the dilution, e.g. 1ul labeled + 10ul unlabeled + 88ul PEM80 + 1ul Taxol 2mM)
15- Flow motility mix (total volume 50ul)
    a. 39.5 ul PEM80
    b. 3.5 ul CPK
    c. 2.5 ul ATP 10mM
    d. 1 ul Phospho
    e. 1 ul DDT 100mM
    f. 0.5 ul Taxol 2mM
    g. *1 ul Glucose
    h. *1 ul Scav
16- Seal the flow cell with UV glue and do the imaging.

A.3 GMPCPP Microtubule Polymerization

1. Mix unlabeled tubulin with labeled tubulin in a 500µl ultracentrifuge tube. Incubate on ice for 10 min. (For the active nematic experiment, final concentration: (6.8mg/ml and ~4% labeling)
2. Centrifuge the tubulin mixture for 10min at 90,000 rpm at 4°C.
3. Pipette the supernatant, keep it in a new Eppendorf tube, and discard the pellet.
4. Add GMPCPP with the final concentration of 0.6mM
5. Add 100mM DTT with the final concentration of 1mM
6. Incubate the Eppendorf tube at 37C water bath for 30min
7. Centrifuge it at room temperature at 14000 rpm for 10min
8. Remove the supernatant and resuspend the pellet in M2B buffer with the final concentration of 6mg/ml
9. Store at room temperature for 2 hours
10. Flash freeze aliquots with liquid nitrogen and store them at -80

A.4 Preparation of PDMS Mold for Confined Microtubule-based Active Nematic

1. Design the desired structure on AutoDesk Fusion 360 software
2. 3D print the design (Phrozen Sonic mini 8k)
3. After printing, clean in 3 steps with isopropanol alcohol (IPA):
    a. Dip the molds in the IPA
    b. Spray IPA on the mold to clean the resin residues between small features of the mold
    c. Use a cleaning station filled with IPA for approximately 20 min to clean all the resin residues from the mold
4. UV cure under the UV lamp for 45 min
5. Thermal cure the mold in the oven at 120 C for 2 h
6. Use the PDMS kit and mix the PDMS elastomer base with the curing agent in a ratio of 10:1
7. Degas the mix under desiccator for 1 h
8. Pour mixed PDMS on the master mold in a disposable container (e.g., weight boat)
9. Let PDMS cure in the oven for 4 h at 60 C
10. Remove the mold from the PDMS
11. Clean the PDMS mold with ethanol and IPA, respectively
12. Use plasma cleaner to make the PDMS surface clean and hydrophilic (at low for 1 min)
13. Prepare the silane agent (100 mL ethanol, 1 mL acetic acid, 500 μL 3-(trimethoxysilyl)propyl methacrylate
14. Add fresh silane agent on the surface and keep it for 15 min, then rinse it 3 times with DI water
15. Add acrylamide solution to coat the surface with a hydrophilic polymer brush
    a. 95 ml DI water
    b. 5 ml Acrylamide solution 40%
    c. Degas for 30 min
    d. Add 35 μL TEMED
    e. Add 0.07 g Ammonium Persulfate (APS)
16. Add acrylamide solution to the mold and incubate it at room temperature for at least 1 h before use. The acrylamide-coated PDMS can be stored at room temperature with acrylamide for up to three weeks.
17. Rinse the mold three times with DI water before the experiment

A.5 Component of active MIX

MIX		**Stock solution**	**v/V**
Microtubule	GMPCPP polymerized microtubule	6 mg/mL	0.167
Kinesin	K401-bio	0.07 mg/mL	0.018
Streptavidin		0.325 mg/mL	0.021
Pluronic-F127		12%	0.112
PEG (20kDa)	Polyethylene Glycol	6% w/v	0.149
DTT	1-4 Dithiothhreitol	0.5 mM	0.011
ATP	Adenosine Triphosphate	10 mM	0.1
PKLDH	Pyruvate Kinase/Lactic Dehydrogenase enzymes	600-1,000 units/mL pyruvate kinase	0.031
		900-1400 units/mL lactic dehydrogenase	
Trolox		20 mg/mL	0.112
Glucose		300 mg/mL	0.011
Glucose Oxidase		20 mg/mL	0.011
Catalase		3.5 mg/mL	0.011
PEP	Phosphoenol Pyruvate	200 mM	0.149
M2B Buffer	80mM PIPES (PH 6.8), 2mM $MgCl_2$, 1mM EGTA		0.043
High-salt M2B	M2B Buffer and 1M $MgCl_2$	1M $MgCl_2$	0.054

Bibliography

[1] L. S. Hirst, *Fundamentals of Soft Matter Science*, 2nd ed. CRC Press, 2019. doi: 10.1201/9781315192383.

[2] D. Needleman and Z. Dogic, 'Active matter at the interface between materials science and cell biology', *Nat Rev Mater*, vol. 2, no. 9, p. 17048, Jul. 2017, doi: 10.1038/natrevmats.2017.48.

[3] R. Zhang, A. Mozaffari, and J. J. de Pablo, 'Autonomous materials systems from active liquid crystals', *Nature Reviews Materials*, vol. 6, no. 5. Nature Research, pp. 437–453, May 01, 2021. doi: 10.1038/s41578-020-00272-x.

[4] A. Tan, 'Microtubule-kinesin based active matter', Merced, 2020. [Online]. Available: https://escholarship.org/uc/item/9n91d036

[5] Nédélec FJ, Surrey T, Maggs AC, and Leibler S, 'Self-organization of microtubules and motors', *Nature*, vol. 389, no. 6648, pp. 305–308, Sep. 1997.

[6] R. Phillips, J. Kondev, J. Theriot, H. G. Garcia, and N. Orme, *Physical Biology of the Cell*. Garland Science, 2012. doi: 10.1201/9781134111589.

[7] S. Eldeen *et al.*, 'Quantifying the non-equilibrium activity of an active colloid', *Soft Matter*, vol. 16, no. 31, pp. 7202–7209, 2020, doi: 10.1039/D0SM00398K.

[8] B. Lemma, L. Lemma, S. C. Ems-McClung, C. E. Walczak, Z. Dogic, and D. J. Needleman, 'Structure and dynamics of motor-driven microtubule bundles', Sep. 2022, [Online]. Available: http://arxiv.org/abs/2209.06637

[9] F. J. Schwarzendahl and D. A. Beller, 'Do active nematic self-mixing dynamics help growing bacterial colonies to maintain local genetic diversity?', May 2022, [Online]. Available: http://arxiv.org/abs/2205.05185

[10] T. Sanchez, D. T. N. Chen, S. J. Decamp, M. Heymann, and Z. Dogic, 'Spontaneous motion in hierarchically assembled active matter', *Nature*, vol. 491, no. 7424, pp. 431–434, Nov. 2012, doi: 10.1038/nature11591.

[11] A. J. Tan *et al.*, 'Topological chaos in active nematics', *Nat Phys*, vol. 15, no. 10, pp. 1033–1039, Oct. 2019, doi: 10.1038/s41567-019-0600-y.

[12] A. J. Tan, D. E. Chapman, L. S. Hirst, and J. Xu, 'Understanding the role of transport velocity in biomotor-powered microtubule spool assembly', *RSC Adv*, vol. 6, no. 82, pp. 79143–79146, 2016, doi: 10.1039/c6ra19094d.

[13] J. Toner and Y. Tu, 'Long-Range Order in a Two-Dimensional Dynamical Model: How Birds Fly Together', *Phys Rev Lett*, vol. 75, no. 23, pp. 4326–4329, Dec. 1995, doi: 10.1103/PhysRevLett.75.4326.

[14] F. Ginelli, 'The Physics of the Vicsek model', *Eur Phys J Spec Top*, vol. 225, no. 11–12, pp. 2099–2117, Nov. 2016, doi: 10.1140/epjst/e2016-60066-8.
[15] S. Bernardi and M. Scianna, 'An agent-based approach for modelling collective dynamics in animal groups distinguishing individual speed and orientation', *Philosophical Transactions of the Royal Society B: Biological Sciences*, vol. 375, no. 1807, p. 20190383, Sep. 2020, doi: 10.1098/rstb.2019.0383.
[16] M. E. Cates and J. Tailleur, 'Motility-Induced Phase Separation', *Annu Rev Condens Matter Phys*, vol. 6, no. 1, pp. 219–244, Mar. 2015, doi: 10.1146/annurev-conmatphys-031214-014710.
[17] Y. Yi, L. Sanchez, Y. Gao, and Y. Yu, 'Janus particles for biological imaging and sensing', *Analyst*, vol. 141, no. 12, pp. 3526–3539, 2016, doi: 10.1039/C6AN00325G.
[18] Y. Wang *et al.*, 'Application of Janus Particles in Point-of-Care Testing', *Biosensors (Basel)*, vol. 12, no. 9, p. 689, Aug. 2022, doi: 10.3390/bios12090689.
[19] Y. Ye *et al.*, 'Fabrication of Self-Propelled Micro- and Nanomotors Based on Janus Structures', *Chemistry – A European Journal*, p. chem.201900840, May 2019, doi: 10.1002/chem.201900840.
[20] C. Huang and X. Shen, 'Janus molecularly imprinted polymer particles', *Chem. Commun.*, vol. 50, no. 20, pp. 2646–2649, 2014, doi: 10.1039/C3CC49586H.
[21] J. Hu, S. Zhou, Y. Sun, X. Fang, and L. Wu, 'Fabrication, properties and applications of Janus particles', *Chem Soc Rev*, vol. 41, no. 11, p. 4356, 2012, doi: 10.1039/c2cs35032g.
[22] Y. Li *et al.*, 'Self-stratification of amphiphilic Janus particles at coating surfaces', *Mater Horiz*, vol. 7, no. 8, pp. 2047–2055, 2020, doi: 10.1039/D0MH00589D.
[23] T. Bellini, R. Cerbino, and G. Zanchetta, 'DNA-Based Soft Phases', 2011, pp. 225–279. doi: 10.1007/128_2011_230.
[24] B. E. Collins, L. F. Ye, D. Duzdevich, and E. C. Greene, 'DNA curtains', 2014, pp. 217–234. doi: 10.1016/B978-0-12-420138-5.00012-4.
[25] I. Kaverina, O. Krylyshkina, and J. V. Small, 'Microtubule Targeting of Substrate Contacts Promotes Their Relaxation and Dissociation', *Journal of Cell Biology*, vol. 146, no. 5, pp. 1033–1044, Sep. 1999, doi: 10.1083/jcb.146.5.1033.
[26] H. Rischer, G. R. Szilvay, and K.-M. Oksman-Caldentey, 'Cellular agriculture — industrial biotechnology for food and materials', *Curr Opin Biotechnol*, vol. 61, pp. 128–134, Feb. 2020, doi: 10.1016/j.copbio.2019.12.003.

[27] T. B. Saw *et al.*, 'Topological defects in epithelia govern cell death and extrusion', *Nature*, vol. 544, no. 7649, pp. 212–216, Apr. 2017, doi: 10.1038/nature21718.
[28] A. Doostmohammadi, J. Ignés-Mullol, J. M. Yeomans, and F. Sagués, 'Active nematics', *Nat Commun*, vol. 9, no. 1, p. 3246, Aug. 2018, doi: 10.1038/s41467-018-05666-8.
[29] A. A. Hyman, D. Chr6tien, I. Arnal, and R. H. Wade, 'Structural Changes Accompanying GTP Hydrolysis in Microtubules: Information from a Slowly Hydrolyzable Analogue Guanylyl-(c ,/3)-Methylene-Diphosphonate', 1995. [Online]. Available: http://rupress.org/jcb/article-pdf/128/1/117/1256849/117.pdf
[30] C. L. Hueschen, V. Galstyan, M. Amouzgar, R. Phillips, and S. Dumont, 'Microtubule End-Clustering Maintains a Steady-State Spindle Shape', *Current Biology*, vol. 29, no. 4, pp. 700-708.e5, Feb. 2019, doi: 10.1016/j.cub.2019.01.016.
[31] E. Nogales, V. H. Ramey, and H. W. Wang, *Cryo-EM studies of microtubule structural intermediates and kinetochore-microtubule interactions*, vol. 95, no. C. Academic Press Inc., 2010. doi: 10.1016/S0091-679X(10)95008-5.
[32] S. W. Manka and C. A. Moores, 'Microtubule structure by cryo-EM: Snapshots of dynamic instability', *Essays in Biochemistry*, vol. 62, no. 6. Portland Press Ltd, pp. 737–751, Dec. 07, 2018. doi: 10.1042/EBC20180031.
[33] A. M. Tayar, L. M. Lemma, and Z. Dogic, 'Assembling Microtubule-Based Active Matter', in *Methods in Molecular Biology*, Humana Press Inc., 2022, pp. 151–183. doi: 10.1007/978-1-0716-1983-4_10.
[34] B. J. Lafrance *et al.*, 'Structural transitions in the GTP cap visualized by cryo-electron microscopy of catalytically inactive microtubules', *BIOPHYSICS AND COMPUTATIONAL BIOLOGY*, vol. 119, no. 2, p. e2114994119, 2022, doi: 10.1073/pnas.2114994119/-/DCSupplemental.
[35] R. D. Vale, 'Review The Molecular Motor Toolbox for Intracellular Transport transport involves molecular motor proteins that carry cargo directionally along a cytoskeletal track (myosins along actin and kinesins and dyneins along microtu', 2003. [Online]. Available: www.proteome.com/YPDhome.html
[36] M. J. Schnitzer and S. M. Block, 'Kinesin hydrolyses one ATP per 8-nm step', *Nature*, vol. 388, no. 6640, pp. 386–390, Jul. 1997, doi: 10.1038/41111.
[37] G. Lee *et al.*, 'Myosin-driven actin-microtubule networks exhibit self-organized contractile dynamics', *Sci Adv*, vol. 7, no. 6, Feb. 2021, doi: 10.1126/sciadv.abe4334.

[38] S. P. Gilbert, M. R. Webb, M. Brune, and K. A. Johnson, ‘Pathway of processive ATP hydrolysis by kinesin’, *Nature*, vol. 373, no. 6516, pp. 671–676, Feb. 1995, doi: 10.1038/373671a0.
[39] J. J. Silberg and L. E. Vickery, ‘Kinetic characterization of the ATPase cycle of the molecular chaperone Hsc66 from Escherichia coli’, *Journal of Biological Chemistry*, vol. 275, no. 11, pp. 7779–7786, Mar. 2000, doi: 10.1074/jbc.275.11.7779.
[40] D. L. Coy, W. O. Hancock, M. Wagenbach, and J. Howard, ‘Kinesin’s tail domain is an inhibitory regulator of the motor domain’, *Nat Cell Biol*, vol. 1, no. 5, pp. 288–292, Sep. 1999, doi: 10.1038/13001.
[41] S. R. Nelson, K. M. Trybus, and D. M. Warshaw, ‘Motor coupling through lipid membranes enhances transport velocities for ensembles of myosin Va’, *Proceedings of the National Academy of Sciences*, vol. 111, no. 38, Sep. 2014, doi: 10.1073/pnas.1406535111.
[42] N. Sarpangala and A. Gopinathan, ‘Cargo surface fluidity can reduce inter-motor mechanical interference, promote load-sharing and enhance processivity in teams of molecular motors’, *PLoS Comput Biol*, vol. 18, no. 6, Jun. 2022, doi: 10.1371/journal.pcbi.1010217.
[43] D. Inoue *et al.*, ‘Depletion force induced collective motion of microtubules driven by kinesin’, *Nanoscale*, vol. 7, no. 43, pp. 18054–18061, Nov. 2015, doi: 10.1039/c5nr02213d.
[44] J. Lopes, ‘Membrane-Bound Kinesin Transport and its Applications in Active Matter’, Merced, 2019. [Online]. Available: https://escholarship.org/uc/item/0wt2t6z0
[45] J. Lopes, D. A. Quint, D. E. Chapman, M. Xu, A. Gopinathan, and L. S. Hirst, ‘Membrane mediated motor kinetics in microtubule gliding assays’, *Sci Rep*, vol. 9, no. 1, Dec. 2019, doi: 10.1038/s41598-019-45847-z.
[46] D. Stelter and T. Keyes, ‘Simulation of fluid/gel phase equilibrium in lipid vesicles’, *Soft Matter*, vol. 15, no. 40, pp. 8102–8112, 2019, doi: 10.1039/C9SM00854C.
[47] G. M’Baye, Y. Mély, G. Duportail, and A. S. Klymchenko, ‘Liquid Ordered and Gel Phases of Lipid Bilayers: Fluorescent Probes Reveal Close Fluidity but Different Hydration’, *Biophys J*, vol. 95, no. 3, pp. 1217–1225, Aug. 2008, doi: 10.1529/biophysj.107.127480.
[48] J. M. Boggs, ‘Lipid intermolecular hydrogen bonding: influence on structural organization and membrane function’, *Biochimica et Biophysica Acta (BBA) - Reviews on Biomembranes*, vol. 906, no. 3, pp. 353–404, Oct. 1987, doi: 10.1016/0304-4157(87)90017-7.
[49] S. Shankar, S. Ramaswamy, M. C. Marchetti, and M. J. Bowick, ‘Defect Unbinding in Active Nematics’, *Phys Rev Lett*, vol. 121, no. 10, Sep. 2018, doi: 10.1103/PhysRevLett.121.108002.

[50] D. Dell'Arciprete *et al.*, 'A growing bacterial colony in two dimensions as an active nematic', *Nat Commun*, vol. 9, no. 1, Dec. 2018, doi: 10.1038/s41467-018-06370-3.
[51] 'UC Merced UC Merced Electronic Theses and Dissertations Title Microtubule-kinesin based active matter', 2016. [Online]. Available: https://escholarship.org/uc/item/9n91d036
[52] S. Henkes, M. C. Marchetti, and R. Sknepnek, 'Dynamical patterns in nematic active matter on a sphere', *Phys Rev E*, vol. 97, no. 4, Apr. 2018, doi: 10.1103/PhysRevE.97.042605.
[53] R. Zhang, Y. Zhou, M. Rahimi, and J. J. de Pablo, 'Dynamic structure of active nematic shells', *Nat Commun*, vol. 7, Nov. 2016, doi: 10.1038/ncomms13483.
[54] A. Opathalage *et al.*, 'Self-organized dynamics and the transition to turbulence of confined active nematics', *Proc Natl Acad Sci U S A*, vol. 116, no. 11, pp. 4788–4797, 2019, doi: 10.1073/pnas.1816733116.
[55] V. VanDelinder, Z. I. Imam, and G. Bachand, 'Kinesin motor density and dynamics in gliding microtubule motility', *Sci Rep*, vol. 9, no. 1, Dec. 2019, doi: 10.1038/s41598-019-43749-8.
[56] S. Tanida *et al.*, 'Gliding filament system giving both global orientational order and clusters in collective motion', *Phys Rev E*, vol. 101, no. 3, Mar. 2020, doi: 10.1103/PhysRevE.101.032607.
[57] J.-L. Thiffeault, M. D. Finn, E. Gouillart, and T. Hall, 'Topology of Chaotic Mixing Patterns', Apr. 2008, doi: 10.1063/1.2973815.
[58] M. D. Finn and J.-L. Thiffeault, 'Topological optimisation of rod-stirring devices', Apr. 2010, doi: 10.1137/100791828.
[59] R. L. Adler, A. G. Konheim, and M. H. McAndrew, 'Topological Entropy', *Trans Am Math Soc*, vol. 114, no. 2, p. 309, Feb. 1965, doi: 10.2307/1994177.
[60] J.-L. Thii, 'Braids and Dynamics', 2022. Accessed: May 04, 2023. [Online]. Available: https://link.springer.com/book/10.1007/978-3-031-04790-9
[61] L. M. Lemma, S. J. Decamp, Z. You, L. Giomi, and Z. Dogic, 'Statistical Properties of Autonomous Flows in 2D Active Nematics', 2019.
[62] A. Doostmohammadi, M. F. Adamer, S. P. Thampi, and J. M. Yeomans, 'Stabilization of active matter by flow-vortex lattices and defect ordering', *Nat Commun*, vol. 7, Feb. 2016, doi: 10.1038/ncomms10557.
[63] T. N. Shendruk, A. Doostmohammadi, K. Thijssen, and J. M. Yeomans, 'Dancing disclinations in confined active nematics', *Soft Matter*, vol. 13, no. 21, pp. 3853–3862, 2017, doi: 10.1039/b000000x.
[64] M. M. Norton, P. Grover, M. F. Hagan, and S. Fraden, 'Optimal Control of Active Nematics', *Phys Rev Lett*, vol. 125, no. 17, p. 178005, Oct. 2020, doi: 10.1103/PhysRevLett.125.178005.

[65] F. C. Keber *et al.*, 'Topology and dynamics of active nematic vesicles', *Science (1979)*, vol. 345, no. 6201, pp. 1135–1139, Sep. 2014, doi: 10.1126/science.1254784.
[66] P. W. Ellis, D. J. G. Pearce, Y. W. Chang, G. Goldsztein, L. Giomi, and A. Fernandez-Nieves, 'Curvature-induced defect unbinding and dynamics in active nematic toroids', *Nat Phys*, vol. 14, no. 1, pp. 85–90, 2018, doi: 10.1038/NPHYS4276.
[67] J.-L. Thiffeault and M. D. Finn, 'Topology, braids and mixing in fluids', *Philosophical Transactions of the Royal Society A: Mathematical, Physical and Engineering Sciences*, vol. 364, no. 1849, pp. 3251–3266, Dec. 2006, doi: 10.1098/rsta.2006.1899.
[68] H. Gruler, 'The Elastic Constants of a Nematic Liquid Crystal', 1975.
[69] E. J. Hemingway, P. Mishra, M. C. Marchetti, and S. M. Fielding, 'Correlation lengths in hydrodynamic models of active nematics', *Soft Matter*, vol. 12, pp. 7943–7952, 2016, doi: 10.1039/b000000x.
[70] R. Grover, J. Fischer, F. W. Schwarz, W. J. Walter, P. Schwille, and S. Diez, 'Transport efficiency of membrane-anchored kinesin-1 motors depends on motor density and diffusivity', *Proc Natl Acad Sci U S A*, vol. 113, no. 46, pp. E7185–E7193, Nov. 2016, doi: 10.1073/pnas.1611398113.
[71] M. Tjioe *et al.*, 'Multiple kinesins induce tension for smooth cargo transport', *Elife*, vol. 8, Oct. 2019, doi: 10.7554/eLife.50974.
[72] A. Sciortino and A. R. Bausch, 'Pattern formation and polarity sorting of driven actin filaments on lipid membranes', *PHYSICS BIOPHYSICS AND COMPUTATIONAL BIOLOGY*, vol. 118, no. 6, 2021, doi: 10.1073/pnas.2017047118/-/DCSupplemental.
[73] F. Pincet *et al.*, 'FRAP to characterize molecular diffusion and interaction in various membrane environments', *PLoS One*, vol. 11, no. 7, Jul. 2016, doi: 10.1371/journal.pone.0158457.
[74] M. Kang, C. A. Day, A. K. Kenworthy, and E. DiBenedetto, 'Simplified equation to extract diffusion coefficients from confocal FRAP data', *Traffic*, vol. 13, no. 12, pp. 1589–1600, Dec. 2012, doi: 10.1111/tra.12008.
[75] M. Fritzsche *et al.*, 'Cytoskeletal actin dynamics shape a ramifying actin network underpinning immunological synapse formation', *Sci Adv*, vol. 3, no. 6, Jun. 2017, doi: 10.1126/sciadv.1603032.
[76] A. Ciudad and J. M. Sancho, 'External mechanical force as an inhibition process in kinesin's motion', *Biochemical Journal*, vol. 390, no. 1, pp. 345–349, Aug. 2005, doi: 10.1042/BJ20042092.
[77] W. Thielicke and R. Sonntag, 'Particle Image Velocimetry for MATLAB: Accuracy and enhanced algorithms in PIVlab', *J Open Res Softw*, vol. 9, no. 1, p. 12, May 2021, doi: 10.5334/jors.334.
[78] W. Thielicke and E. J. Stamhuis, 'PIVlab – Towards User-friendly, Affordable and Accurate Digital Particle Image Velocimetry in MATLAB', *J Open Res Softw*, vol. 2, Oct. 2014, doi: 10.5334/jors.bl.

[79] W. Thielicke and A. (Anita G. J. Buma, *The flapping flight of birds : analysis and application*. 2014.
[80] K. Kim, N. Yoshinaga, S. Bhattacharyya, H. Nakazawa, M. Umetsu, and W. Teizer, 'Large-scale chirality in an active layer of microtubules and kinesin motor proteins', *Soft Matter*, vol. 14, no. 17, pp. 3221–3231, 2018, doi: 10.1039/c7sm02298k.
[81] C. A. Scarff, M. J. G. Fuller, R. F. Thompson, and M. G. Iadaza, 'Variations on negative stain electron microscopy methods: Tools for tackling challenging systems', *Journal of Visualized Experiments*, vol. 2018, no. 132, Feb. 2018, doi: 10.3791/57199.
[82] R. J. T. Nambayan, S. I. Sandin, D. A. Quint, D. M. Satyadi, and E. de Alba, 'The inflammasome adapter ASC assembles into filaments with integral participation of its two Death Domains, PYD and CARD', *Journal of Biological Chemistry*, vol. 294, no. 2, pp. 439–452, Jan. 2019, doi: 10.1074/jbc.RA118.004407.
[83] L. S. H. L. M. Designed Research; F and N. S. L. M. Performed Research; F, 'Active nematic order and dynamic lane formation of microtubules driven by membrane-bound diffusing motors', vol. 118, 2021, doi: 10.1073/pnas.2117107118/-/DCSupplemental.
[84] K. Thijssen *et al.*, 'Submersed micropatterned structures control active nematic flow, topology, and concentration', *PNAS*, vol. 118, no. 38, p. e2106038118, 2021, doi: 10.1073/pnas.2106038118/-/DCSupplemental.y.
[85] P. Guillamat, J. Ignés-Mullol, S. Shankar, M. C. Marchetti, and F. Sagués, 'Probing the shear viscosity of an active nematic film', *Phys Rev E*, vol. 94, no. 6, Dec. 2016, doi: 10.1103/PhysRevE.94.060602.
[86] E. Berliner, E. C. Young, K. Anderson, H. K. Mahtani, and J. Jeff, 'Failure of a single-headed kinesin to track parallel to microtubule protofilaments', *Nature*, vol. 373, no. 6516, pp. 718–721, Feb. 1995, doi: 10.1038/373718a0.
[87] W. O. Hancock and J. Howard, 'Processivity of the Motor Protein Kinesin Requires Two Heads', 1998. [Online]. Available: http://www.jcb.org
[88] A. Gennerich and R. D. Vale, 'Walking the walk: how kinesin and dynein coordinate their steps', *Current Opinion in Cell Biology*, vol. 21, no. 1. pp. 59–67, Feb. 2009. doi: 10.1016/j.ceb.2008.12.002.
[89] N. Kumar, R. Zhang, J. J. de Pablo, and M. L. Gardel, 'Tunable structure and dynamics of active liquid crystals', 2018. [Online]. Available: https://www.science.org
[90] J. Hardoüin *et al.*, 'Reconfigurable flows and defect landscape of confined active nematics', *Commun Phys*, vol. 2, no. 1, Dec. 2019, doi: 10.1038/s42005-019-0221-x.
[91] J. Hardoüin, C. Doré, J. Laurent, T. Lopez-Leon, J. Ignés-Mullol, and F. Sagués, 'Active boundary layers in confined active nematics', *Nat Commun*, vol. 13, no. 1, Dec. 2022, doi: 10.1038/s41467-022-34336-z.

[92] B. Venzac *et al.*, 'PDMS Curing Inhibition on 3D-Printed Molds: Why? Also, How to Avoid It?', *Anal Chem*, vol. 93, no. 19, pp. 7180–7187, May 2021, doi: 10.1021/acs.analchem.0c04944.
[93] F. L. Memarian, D. A. Khaladj, D. Hammar, and L. S. Hirst, 'Forming, Confining, and Observing Microtubule-Based Active Nematics', *Journal of Visualized Experiments*, no. 191, Jan. 2023, doi: 10.3791/64287.
[94] A. Satoshi, J. Kougo, F. Araoka, O. Haba, and K. Yonetake, 'Nontrivial topological defects of micro-rods immersed in nematics and their phototuning', *Phys. Chem. Chem. Phys.*, vol. 24, pp. 3338–3347, 2022, Accessed: Mar. 08, 2023. [Online]. Available: https://doi.org/10.1039/D1CP03363H
[95] P. B. Rhines, 'Mixing and Large-Scale Ocean Dynamics', 1988.
[96] W. Baeyens *et al.*, 'In situ measurements of micronutrient dynamics in open seawater show that complex dissociation rates may limit diatom growth', *Sci Rep*, vol. 8, no. 1, Dec. 2018, doi: 10.1038/s41598-018-34465-w.
[97] K. A. Mitchell, A. J. Tan, J. Arteaga, and L. S. Hirst, 'Fractal generation in a two-dimensional active-nematic fluid', *Chaos: An Interdisciplinary Journal of Nonlinear Science*, vol. 31, no. 7, p. 073125, Jul. 2021, doi: 10.1063/5.0050795.